Phase transformations and stress evolution during laser beam welding and post heat treatment of TiAl-alloys

(Vom Promotionsausschuss der Technischen Universität Hamburg-Harburg als Dissertation angenommene Arbeit)

J. Liu

wissen
schafft
nutzen

Helmholtz-Zentrum
Geesthacht
Zentrum für Material- und Küstenforschung

Phase transformations and stress evolution during laser beam welding and post heat treatment of TiAl-alloys

(Vom Promotionsausschuss der Technischen Universität Hamburg-Harburg als Dissertation angenommene Arbeit)

J. Liu

Phase transformations and stress evolution during laser beam welding and post heat treatment of TiAl-alloys

(Vom Promotionsausschuss der Technischen Universität Hamburg-Harburg als Dissertation angenommene Arbeit)

Jie Liu

104 pages with 57 figures and 6 tables

Abstract

γ-TiAl material is an attractive alternative candidate for aerospace and automotive applications because of its low density, high specific yield strength and high creep and oxidation resistance. It has been used successfully in the manufacture of low-pressure turbine blades in the GEnx^{TM} engine, which represents a major advance in propulsion efficiency, with a 20% reduction in fuel consumption, a 50% reduction in noise, and an 80% reduction in NO_x emissions compared with prior engines of the same class. In future, γ-TiAl will most likely be applied as a structural material in the combustion turbine of aircraft; for this purpose, the challenge of determining a method for the proper joining of this material must be met.

Laser beam welding is considered to be a promising joining method. However, because of the low ductility and fracture toughness of γ-TiAl alloys at ambient temperature, cracks are frequently observed in welding seams. The high cooling rate further reduces the weldability of the alloy, as a large amount of brittle phase and high residual stresses are formed. Thus, there are four problems that must be solved: (1) How can a crack-free TiAl butt joint be produced? (2) How can the microstructural and mechanical properties of the weld be improved? (3) How do the phases transform during welding? (4) How to perform a fast and reliable welding?

The objective of this thesis is to methodically address these challenges. First, because of the intrinsic brittleness of the alloy, several heat treatments using a furnace and a defocused laser are applied to heat the alloys above the brittle-to-ductile transition temperature and reduce the cooling rate. The butt joint welds are investigated via radiography and found to be free of cracks.

Second, the task is the modification of the microstructural and mechanical properties of the welds. The grain refinement induced by borides, which is widely exploited during casting, is suppressed by the high cooling rate. Additionally, a large amount of α_2 phase and residual stress are detrimental to the weld. Thus, post-weld heat treatments are applied to the as-welded specimens to refine the grain size, modify the microstructure and relieve the residual stress. Tensile tests are also conducted to evaluate the mechanical properties of the as-welded and heat-treated specimens.

Third, an *in situ* investigation of the phase transformation as a function of the heating rate is performed at the HZG beamline HEMS at DESY. The phase transformation is plotted over time, and the transformation mechanism is explained. A new concept of grain refinement with the assistance of superheated particles is proposed and applied to the optimisation of the laser beam welding parameters and the mechanical properties of the welds.

Fourth, besides solving the scientific questions, attention is paid to produce fast and reliable welds. Several heating methods are developed and applied, such as resistance furnace heating, induction furnace heating, dual-laser-beam heating and FLEXILAS experiment. Both the advantages and disadvantages of these methods are discussed. It is found out that the FLEXILAS set-up is able to heat the specimen homogeneously and fast. It is proved to be potential for industrial application.

In conclusion, it is demonstrated, on the laboratory scale, that laser beam welding has the potential to be employed for the joining of γ-TiAl alloys used as structural materials. The welding approach developed here is capable of producing a sound joint with an optimised microstructure, low residual stress and good mechanical properties. Moreover, the newly gained understanding of the phase transformation during laser beam welding has revealed a novel grain-refinement mechanism that can be further employed to improve the mechanical performance of the final welds.

Phasenumwandlungen und Spannungsentwicklung beim Laserstrahlschweißen und Nachwärmebehandelung von TiAl-Legierungen

Zusammenfassung

Aufgrund ihrer geringen Dichte, hohen spezifischen Festigkeit, hohen Kriechfestigkeit und Oxidationsbeständigkeit ist γ-TiAl ein attraktiver Strukturwerkstoff und damit ein Kandidat für Luftfahrt- und Automobilanwendungen. In Zukunft wird γ-TiAl höchstwahrscheinlich auch als Strukturmaterial im Verbrennungsbereich der Turbine eingesetzt. Die Herausforderung besteht in der Verfügbarkeit geeigneter Fügemethoden.

Das Laserstrahlschweißen gilt als vielversprechendes Fügeverfahren. Wegen niedriger Duktilität und Bruchzähigkeit der γ-TiAl-Legierungen bei Raumtemperatur werden häufig Risse in Schweißnähten beobachtet. Die hohe Abkühlgeschwindigkeit beim Schmelzschweißen vermindert die Schweißbarkeit der Legierung, weil eine Vielzahl von spröden Phasen und zu hohe Eigenspannungen entstehen. So gibt es vier Probleme, die zuerst gelöst werden müssen: (1) eine rissfreie Stumpfstoßschweißen der γ-TiAl realisieren, (2) die mikrostrukturellen und die mechanischen Eigenschaften der Schweißverbindungen verbessern, (3) Phasenumwandlung während des Schweißens verstehen, (4) ein schnelles und zuverlässiges Stumpstoßschweißen realisieren.

Das Ziel dieser Arbeit ist es, diesen Herausforderungen methodisch zu begegnen. Erstens, wegen der intrinsischen Sprödigkeit der γ-TiAl-Legierung, werden mehrere Wärmebehandlungen unter Verwendung eines Ofens sowie eines defokussierten Laserstrahls durchgeführt, um die γ-TiAl-Legierungen oberhalb der spröd-duktilen Übergangstemperatur zu erwärmen und die Abkühlgeschwindigkeit zu verringern. Die radiographischen Untersuchungen haben gezeigt, dass die Stumpstoßverbindungen rissfrei sind.

Zweitens, die Aufgabenstellung ist die Modifikation des Gefüges und die mechanischen Eigenschaften der Schweißnähte. Nach dem Schweißen werden deshalb gezielt Wärmebehandlungen angewendet, um die Korngröße zu verfeinern, die Mikrostruktur zu verändern und Eigenspannungen abzubauen. Es werden auch Zugversuche durchgeführt, um die mechanischen Eigenschaften der geschweißten und wärmebehandelten Proben zu bewerten.

Drittens wird eine In-situ-Untersuchung der Phasenumwandlung in Abhängigkeit von der Aufheizrate an der HZG-Beamline HEMS bei DESY durchgeführt. Es werden die Phasenumwandlung über die Zeit aufgetragen, und die Umwandlungsmechanismen erläutert. Es wird ein neues Konzept der Kornfeinung durch überhitzte γ-Phase vorgeschlagen, das für die Optimierung der Laserstrahlschweißparameter und die mechanischen Eigenschaften der Schweißnähte angewendet werden kann.

Viertens, neben der Lösung der wissenschaftlichen Fragestellungen wird hier ein Augenmerk auf die Realisierung der schnellen und zuverlässigen Schweißprozesse gerichtet. Mehrere Erwärmungsmethoden werden entwickelt und eingesetzt, wie zum Beispiel die Widerstandsofen-, die Induktionsofen-Heizung und die Dual-Laser-Beam-Erwärmung sowie das für das FLEXILAS-Experiment entwickelte Heiz-Modul. Es werden sowohl die Vor- als auch Nachteile dieser Verfahren diskutiert.

Schließlich der hier entwickelte Ansatz zum Laserstrahlschweißen dieser Legierungsklasse ist geeignet, einen Stumpfstoß mit optimierter Mikrostruktur, geringeren Eigenspannungen und guten mechanischen Eigenschaften zu realisieren.

Contents

List of symbols and abbreviations

α	coefficient of thermal expansion
γ_m	massive γ
ε	strain
θ	Bragg angle, angle between the incident ray and the scattering planes
λ	wavelength
ν	Poisson's ratio
ρ	density
σ	stress
d	lattice parameter
d_0	stress-free lattice parameter
t	time
v	weld speed
x, y, z	spatial coordinates
AC	air cooling
Al	aluminium
Ar	argon
B	boron
BM	base material
BOR	Burgers orientation relationship
BSE	backscattered electron
C	carbon
CCT	continuous cooling transformation
Cu	copper
DESY	Deutsches Elektronen-Synchrotron
DRx	dynamic recrystallisation
E	Young's modulus
EBSD	electron backscatter diffraction technique

EDM	electro-discharge machining
EDS	energy-dispersive spectroscopy
ESRF	European Synchrotron Radiation Facility
FC	furnace cooling
FLEXILAS	flexible *in situ* synchrotron observation of the laser beam welding process
GfE	Gesellschaft für Elektrometallurgie GmbH
GBS	grain boundary sliding
HAZ	heat-affected zone
He	helium
HE	high energy
HEMS	High Energy Materials Science
HEXRD	High Energy X-ray Diffraction
HV	Vickers hardness
HZG	Helmholtz-Zentrum Geesthacht
L	liquid
LD	longitudinal direction to weld
Mo	molybdenum
Nb	niobium
ND	normal direction to weld
Nd:YAG	neodymium-doped yttrium aluminium garnet
OC	oil cooling
OR	orientation relationship
PIGA	plasma melting induction guiding gas atomisation
RT	room temperature
SEM	scanning electron microscope
Si	silicon
SiC	silicon carbide
Si_3N_4	silicon nitride

T	temperature
T_α	α-transus temperature
T_e	eutectoid temperature
Ti	titanium
TiAl	titanium aluminide
TD	transversal direction to weld
UTS	ultimate tensile stress
W	watt
WC	water cooling
WZ	welding zone
XRD	X-ray diffraction

1 Introduction

1.1 Motivation and objectives

γ-TiAl material is an attractive alternative candidate for aerospace and automotive applications because of its low density and good high-temperature properties. As indicated by Figure 1 (a), the density of TiAl alloys is only approximately half that of steel or nickel-based superalloys; however, TiAl alloys exhibit competitively high values of the Young's modulus. As shown in the relationship map of the Young's modulus relative to the density (Figure 1 (a)), Si_3N_4 and SiC are structural ceramics and Ni-based superalloys are structural alloys. TiAl alloys lie between the common structural alloys and the structural ceramics, tending to exhibit a combination of the properties of alloys and ceramics because of the atomic bonding of the transition metal titanium with aluminium [1].

Although the Young's modulus and yield strength of TiAl alloys are not as high as those of steel, titanium and nickel alloys, they are interesting compared to other structural metals when the material density and high application temperatures are important. The density-normalised mechanical properties of various materials, represented by the specific modulus and specific yield strength, are presented in Figure 1 (b) and (c). TiAl alloys demonstrate a specific modulus of 46 GPa/(Mg/m^3) at RT, which slowly decreases to 42 GPa/(Mg/m^3) at 500°C. Meanwhile, Ti-6Al-4V and the nickel-based alloy Inconel-718 exhibit values of approximately 25 GPa/(Mg/m^3) at RT and 20 GPa/(Mg/m^3) at 500°C. The specific modulus of TiAl is over 80% greater than those of titanium and the superalloys, especially at high temperatures. The specific strength of advanced TiAl alloys is much higher than those of the superalloys and titanium alloys at all temperatures and lower than those of single-crystal superalloys and refractory metals only when the temperature is above 1000°C. With the aid of a new generation of TiAl alloys, for example, the TNB-V5 alloy patented at HZG [2] and the TNM alloy developed at the University of Leoben, the upper limit on the strength of cast γ-TiAl 47XD alloys has been extended [3].

Because of their good high-temperature performance, low density and precise manufacturing process, TiAl alloys have now been implemented in turbine blades, turbocharger wheels and motor valves, and they demonstrate attractive prospects for industrial applications by virtue of their good engineering properties at working temperatures near 750°C. In 1999, the first announcement of the commercial application of γ-TiAl-based alloys was released by the Mitsubishi company, which used TiAl turbocharger wheels in the Lancer Evolution 6 sports car [4, 5]. These wheels are produced via a precise casting method by the Daido Steel company using the Levicast process, which is a modification of the lost-wax precision casting method in combination with centrifugal casting [6]. The joining of the TiAl turbine
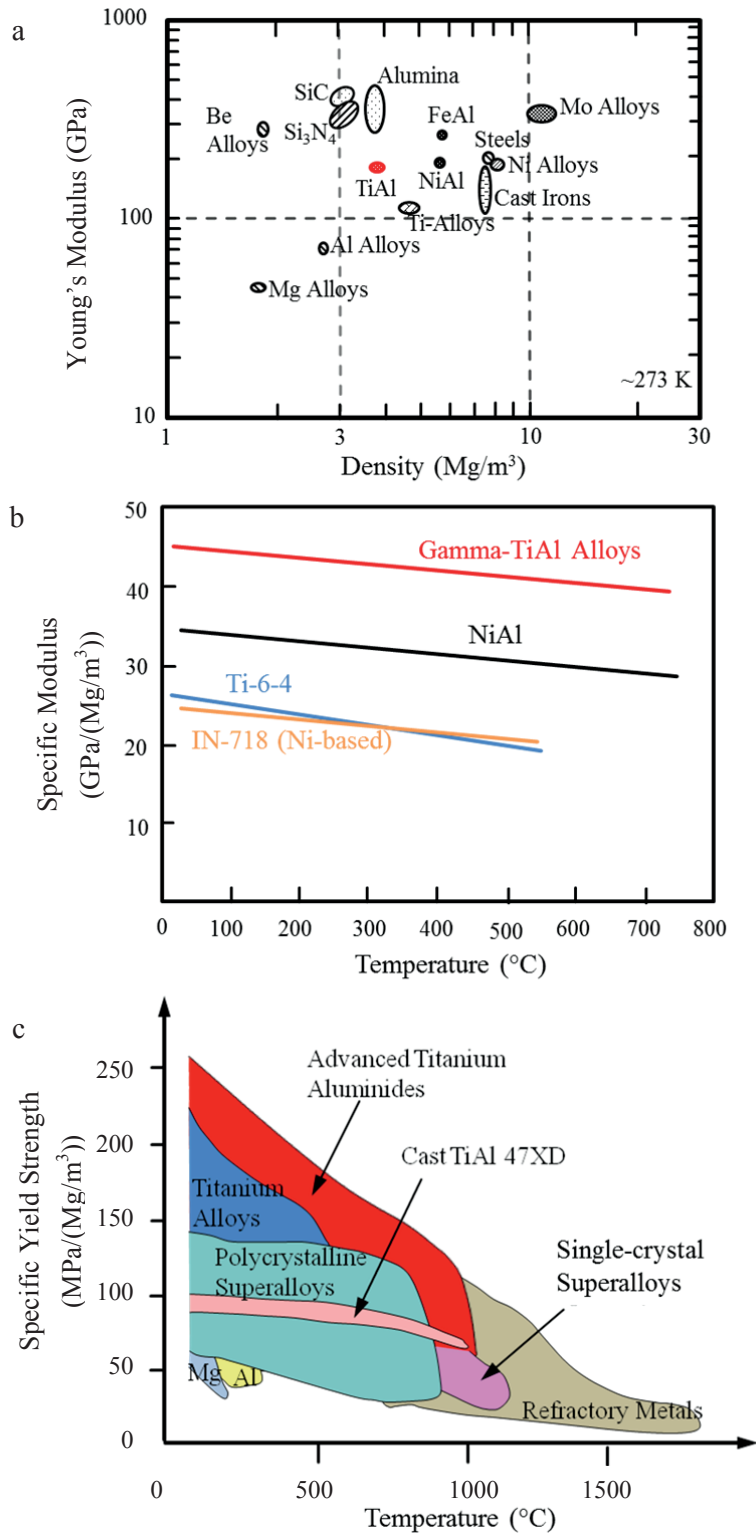
Figure 1: (a) Densities and Young's moduli of various structural materials. Certain density-normalised specific properties of structural alloys and selected intermetallics are also presented: (b) specific modulus versus temperature and (c) specific strength versus temperature [1, 3].

wheel to the steel shaft is accomplished by brazing the TiAl to an insert material and then electron beam welding the insert material to the shaft [4]. In 2002, the serial production of wrought-processed high-performance γ-TiAl engine valves for race cars was launched. These valves are produced through multi-step extrusion and precision machining and coating [6]. In 2008, Kelly of the General Electron Aviation company first announced the beginning of the implementation of cast γ-TiAl blades in low-pressure turbines [7]. Later, in 2012, they presented the GEnx™ engine as the first commercial aircraft engine composed of TiAl alloy (composition Ti-48Al-2Cr-2Nb, at%; atom percent is used throughout this thesis) blades fabricated via near-net-shape casting. Engines fabricated from TiAl alloy represent a major advance in propulsion efficiency, with a 20% reduction in fuel consumption, a 50% reduction in noise, and an 80% reduction in NO_x emissions compared with prior engines of the same class. To date, the company has announced that more than 40,000 TiAl low-pressure turbine blades have been manufactured for use in the Boeing 787 and the Boeing 747-8 [8]. Moreover, the GfE company in Germany has successfully hot rolled TiAl into sheets, which are used in laser-welding experiments in the current study. In summary, TiAl can be feasibly produced and deformed, and it is now gaining interest as a commercial structural material.

In future, it is expected that TiAl will be implemented as a structural material in the aerospace industry. Thus, a good capability for joining TiAl alloy to itself or to other materials is urgently required. Considerable effort has been made to produce sound butt joints via laser beam welding [9, 10], electron beam welding [11, 12], diffusion bonding [13] and friction welding [14-16]. However, because of the intrinsic brittleness of the material, longitudinal and transverse cracks are often observed in the welds, as shown in Figure 2. In addition to such cracking defects, a large amount of residual stress is observed after welding. The longitudinal stress can be as high as 1000 MPa, which is close to the UTS of the material [9], leading to distortion [17, 18] or failure [19]. Thus, the production of crack-free butt joints with optimised welding parameters is the first objective of this work.

Second, it must be possible to ensure the quality of the weld, especially when the welded-material is used as turbine blades. The weld should be as strong as the base material and, at the same time, exhibit acceptable ductility. From the microscopic point of view, an ideal microstructure consists of fine, nearly lamellar γ grains without any distinct texture [3]. However, because of the high cooling gradient, the welding zone consists of a large amount of α_2 phase [11, 20], which appears as textured colonies [21], leading to premature fracture of the welding seam under load. The welding zone is characterised by low toughness and little ability to dissipate local stress concentrations through plastic flow, hindering the application of these materials in the engineering field. Fortunately, with the aid of heat treatment, the microstructural and mechanical properties of the welding zone can be
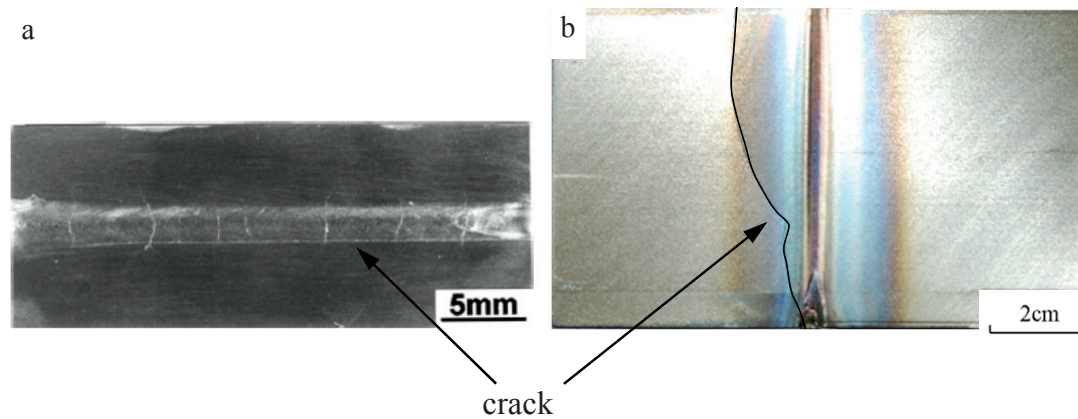
Figure 2: (a) Transverse cracking in a weld at a cooling rate of 1670°C/s [11]. (b) A longitudinal crack.

improved. Phase transformation occurs, leading to the formation of a microstructure with balanced mechanical properties [3, 22, 23]. The grains are refined [24-28], and the residual stresses in the weld are reduced [29-31]. These heat treatments, such as pre-heating and *in situ* heating during welding, reduce the cooling rate, which helps to reduce the crack frequency [11]. Thus, to obtain a sound weld with good microstructural and mechanical properties, it is critical to apply the proper heat treatment to the weld.

Third, the phase transformation is a critical issue for the alloy, as the microstructure is generated by the transformation and influences the mechanical properties. The phase diagram is plotted under equilibrium state [32, 33], which is used for phase transformation. However, it does not likely apply to the laser beam welding, which heats the material ultrafast. It is important to understand the phase transformation behaviour during welding and shed light on the melting and solidifying mechanism of TiAl alloy.

The present study is focused on the following objectives:

1. The application of pre-weld and *in situ* heat treatments to produce a crack-free TiAl butt joint.

2. The improvement of the properties of the weld by means of *in situ* heating using a laser and post-weld heat treatment using a furnace to refine the grain size, optimise the microstructure and obtain balanced mechanical properties in the welding zone.

3. The development of an improved understanding of the equilibrium and non-equilibrium phase transformation during welding to shed light on the properties of TiAl materials. Moreover, this knowledge is applied to further optimise the laser beam welding parameters, in combination with the heat treatment to improve the welding quality.

Beside the scientific objectives to achieve, attention is also paid to improve the welding process, which should be reliable and efficient. Several heating methods are used. The first

welding starts with heating via a conventional resistance heated furnace, which is quite time consuming. It takes around 2 hours to heat a specimen from RT to 750°C, and the cooling takes another 3 hours. With the purpose of increasing the welding efficiency, an induction furnace is applied to take an advantage of fast heating. The welding time is around 15 minutes, which is further reduced to 10 minutes by a dual-laser beam welding. Finally, a specific designed FLEXILAS chamber is able to heat the specimen fast and homogeneously, as it is equipped with a programmed electric system for temperature control. With an assistance of a fiber laser, a reliable weld is made in 15 minutes.

1.2   Structure of the thesis

This thesis is structured based on the schematic view of the scientific approach presented in Figure 3. First, there is an introductory section that presents the fundamentals of the relevant materials knowledge. The next chapter discusses the experimental facilities used in the study. In the following, each experiment is presented in its own individual chapter, which concludes with a discussion of the achieved objectives. Finally, there is a conclusion section that summarises the results obtained from all the experimental studies and the scientific highlights of the work.

Chapter 2 is a literature review. It presents basic knowledge concerning the phase transformation of TiAl alloys. The transformations from liquid to solid and the solid–solid transformations are influenced by factors such as the alloy composition, the temperature gradient and the addition of boride. Particular attention is paid to the discussion of heat treatments because these procedures are important for the prevention of cracking and the improvement of the mechanical properties of the weld. The method for the calculation of the residual stress is introduced.

Chapter 3 discusses the experimental work. It includes methods of specimen preparation, laser beam welding processes, and strategies for the investigation of the welds using radiography, SEM and EBSD. The FLEXILAS experiment, which applied HEXRD at DESY for the *in situ* study of the phase transformation and the calculation of residual stress after laser beam welding, is presented. Finally, the tensile tests to assess the mechanical properties of the welded specimens are described.

Chapters 4 through 7 introduce four experiments performed in pursuit of the three objectives set forth in chapter 1.1. Because of differences in the experimental procedures and evaluation methods, each chapter is presented independently. In each chapter, the experimental conditions and parameters are introduced and advantages and disadvantages of the experimental set-ups are discussed. The experimental set-ups are improved to be faster and more reliable than the previous one. Also, the experimental results are analysed and illustrated. Finally, each chapter ends in a conclusion that summarises the improvement in the material properties that was achieved and the understanding gained from the work.

Chapter 4 focuses on the application of a resistance furnace to preheat the material above the brittle–ductile transition temperature to avoid cracking. The mechanical properties are improved by post-weld heat treatment.

Because resistance furnace heating is quite time consuming, for improved efficiency, in chapter 5, both *in situ* and conventional post weld heat treatment using an induction furnace are conducted. The *in situ* post-weld heating treatment is found to prevent cracking during laser beam welding, and the conventional post-weld heat treatment is found to refine the textured colonies.

Moreover, heat treatments are performed using a defocused laser; the procedure is explained in chapter 6. Because the local heating area can be effectively adjusted by modifying the diameter of the laser beam, the specimen can be heated by means of several different scans. In particular, after welding, the area of interest can be reheated and the temperature cooling gradient in the welding zone is reduced.

To precisely control the temperature field and gain an understanding of the phase transformation during welding, *in situ* HEXRD observations are presented in chapter 7. The laser facilities and welding chamber are transported to DESY. Using a fast detector, the diffraction patterns are recorded and analysed. The phase-transformation behaviours observed at various laser powers are illustrated. This knowledge of the phase transformations is applied for welding-parameter optimisation and weld-quality improvement.

Chapter 8 serves as the conclusion for the thesis and summarises the important results of this research. It also proposes three challenges to be addressed in future work.
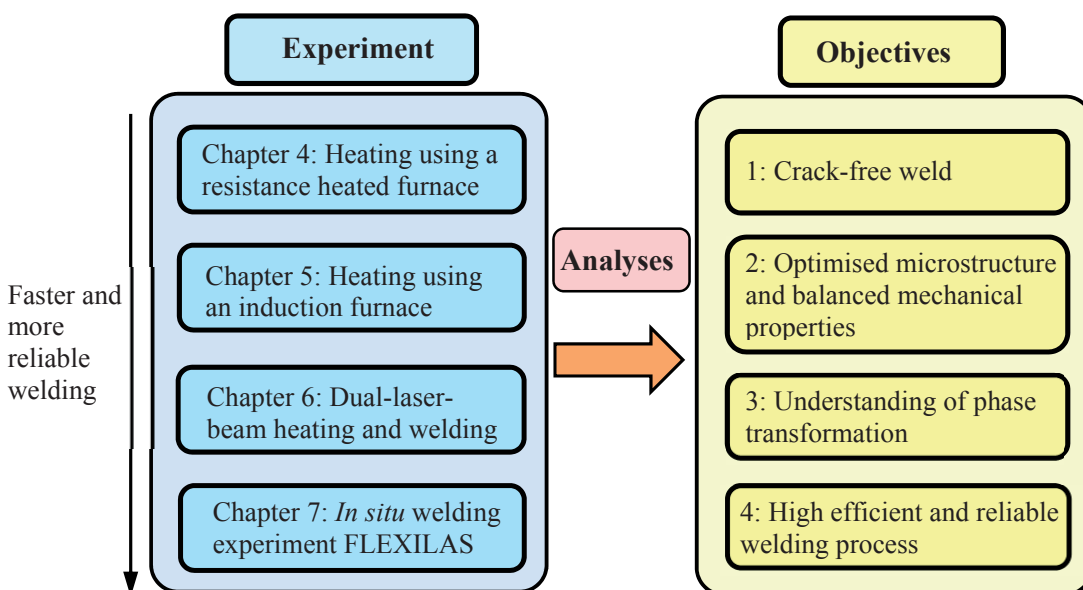

Figure 3: Schematic view of the scientific approach taken in this thesis.

2 State of the art

The first part of this chapter includes a brief introduction of the fundamentals of phase transformations for both equilibrium and non-equilibrium states, including general remarks on liquid–solid and solid–solid phase transformations. Precipitation of α from β with the assistance of borides is also discussed. Additionally, the influence of various heat-treatment methods, i.e., pre-weld, *in situ* and post-weld heat treatments, on the microstructural and mechanical properties of the weld is considered.

The second part of the chapter presents some *in situ* observations acquired during the heating and welding of materials with the assistance of high-energy synchrotron X-ray diffraction. Moreover, the fundamentals of the residual stress and the calculation of the residual stress are clarified.

2.1 Phase transformations

Figure 4 presents the Ti-Al binary phase diagram. As indicated in the figure, there are several intermetallic phases that form depending on the chemical composition. The region of interest, TiAl alloys, typically lies near the chemical compositions of Ti-(42-49)Al, as indicated by the blue background. Throughout the temperature range, the predominant phases in this region are the hexagonal close packed α_2 (Ti_3Al) phase (Strukturbereich designation $D0_{19}$), the hexagonal α (Ti) phase (Strukturbereich designation A_3), the tetragonal γ (TiAl) phase (Strukturbereich designation $L1_0$), the cubic high-temperature B2 phase (Strukturbereich designation B2), and the cubic high-temperature β phase (Strukturbereich designation A2). The liquid–solid and solid–solid phase transformations are discussed below.

2.1.1 Liquid–solid phase transformation

The liquid–solid transformations were calculated by Witusiewicz et al. [34] and are presented in Figure 5, which represents an enlarged view of the peritectic reaction in the binary phase diagram. As is evident from the figure, when the Al concentration is below 44.6 at%, the β phase is the only solid phase when the melt solidifies; this is identified as a β-solidifying alloy. When the Al concentration is between 44.6 and 49.4 at%, the peritectic formation of the α phase follows the primary β formation, with the path of L + β → α. When the Al concentration is above 49.4 at%, the α phase is the first phase to form. The peritectic reaction L + α → γ takes place when the Al content is above 51.5 at%.

The solidification path exerts considerable influence on the texture of the cast alloys. Figure 6 shows examples of the texture-free Ti-45Al alloy and the strongly textured Ti-48Al alloy. In the β-solidifying alloy, which solidifies solely through the β phase, it is observed that during the solid transformation β → β + α → α, the α phase precipitates at the grain

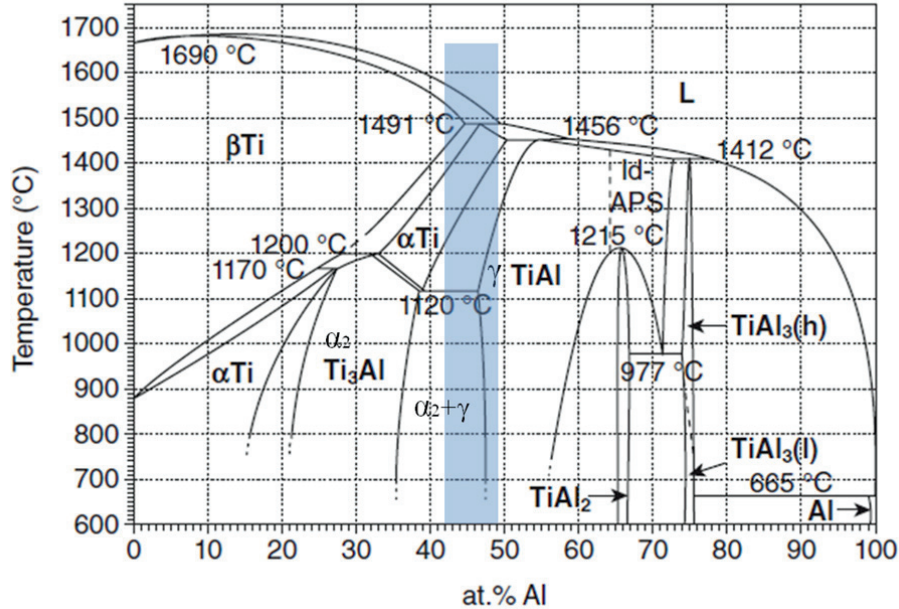boundaries of the primary β phase following the Burgers orientation relationship (BOR) below:

Figure 4: Binary Ti-Al phase diagram, according to the assessment of Schuster and Palm [35].

$$\{110\}_{\beta} // (0001)_{\alpha} \text{ and } <111>_{\beta} // <11\bar{2}0>_{\alpha} \tag{1}$$

Because of the crystallography relationship, there are 12 orientation variants of the basal plane of the α phase with $(110)_{\beta}$. In addition, α grains stemmed from the same primary β phase exhibit 12 orientations. However, if the alloy solidifies through peritectic α, which nucleates in the melt, the primary α phase adopts its preferential growth direction, namely, $(0001)_{\alpha}$ // heat-flow direction. It then grows into the primary β phase and suppresses the solid transformation from β to α. Thus, in this case, the final orientations of the material are determined only by the orientation of the primary α [36, 37]. Therefore, alloys that solidify through peritectic α are found to exhibit stronger texture than β-solidifying alloys [33].

In addition to the Al composition, the binary phase diagram can also be influenced by many alloying elements. Several elements, including W, Re, Fe, Mo, Cr, Nb and Ta, have been identified as effective in promoting β solidification [26, 38], as they shift the α/β primary-solidification phase boundary towards a higher aluminium content.

Elements such as Cr, Nb and Mo have proven to be important in the design of TiAl alloys. The application of such alloying elements began with the General Electric alloy Ti-48Al-2Cr-2Nb and continued with the 2nd generation γ-MET Ti-46.5Al-4(Cr, Nb, Ta, B) alloy; the current 3rd generation of alloys can be described as follows:

$$\text{Ti-(42-48)Al-(0-10)X-(0-3)Y-(0-1)Z-(0-0.5RE)} \tag{2}$$

where X = Cr, Mn, Nb, or Ta; Y = Mo, W, Hf, or Zr; and Z = C, B, or Si. RE denotes a rare earth element. Typical 3rd generation alloys include, for example, the TNB-V5 alloy Ti-45Al-5Nb-0.2C-0.2B developed at HZG [2] and the TNM alloy Ti-(42-45)Al-(3-5)Nb-(0.1-2)Mo-(0.1-1)B designed by the Montanuniversität Leoben. They are both β-solidifying alloys.
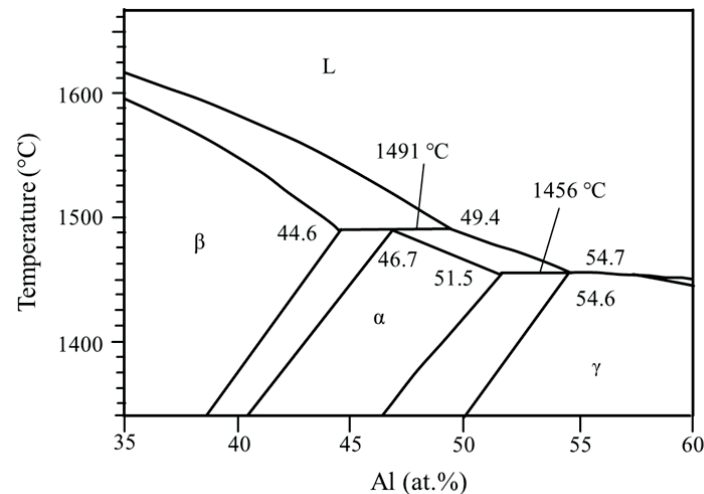
Figure 5: Section of the phase diagram calculated by Witusiewicz et al. for the peritectic reaction [34].
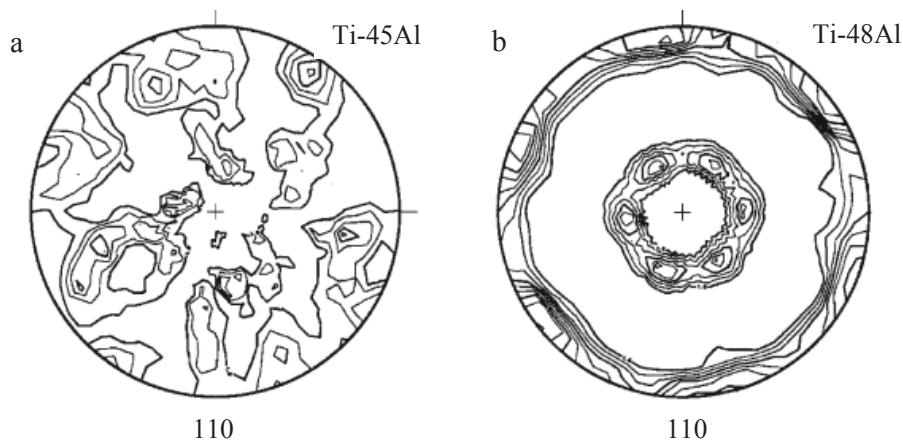
Figure 6: Pole figures of the γ (TiAl) phase determined from binary arc-melted buttons using neutron diffraction [39]: (a) Ti-45Al, {110) pole figure, maximum pole density 1.66 random; (b) Ti-48Al, {110) pole figure, maximum pole density 2.67 random.

2.1.2 Solid–solid phase transformation

The solid-state phase transformations of γ-TiAl-based alloys depend strongly on the cooling rate and chemical composition. On the one hand, when the alloy cools from the α-phase field at a very high cooling rate, the α phase cannot decompose but becomes ordered into α$_2$. As

the cooling rate decreases, the transformation of the α phase yields massive γ, feathery structures, Widmannstätten colonies and lamellae [40-43]. At very low cooling rates, the formation of γ grains is observed. It is possible to plot the CCT diagram as a function of the cooling rate [32, 44]. Figure 7 illustrates the cooling of the alloy Ti-46Al-9Nb from $T_α$ using various cooling methods and the corresponding microstructures. Experiments have demonstrated the $α_2$ phase forms upon water quenching. Oil quenching leads to massive γ. Lamellae are observed following cooling methods at low cooling rates, such as air cooling and furnace cooling. On the other hand, the chemical composition also affects the transformation path. As reported by Jones et al. [32], γ precipitation is observed in an alloy that contains more than 45 at% Al when the alloy is quenched from the α-phase field. However, this precipitation is entirely suppressed at lower Al contents.

Heat treatments that are applied after quenching lead to phase transformation and grain refinement. As shown in Figure 8, a Ti–46Al–8Nb specimen can be oil quenched from 1360°C to form massive γ. Afterward, if the specimen is aged at 1320°C, which is within the (α + γ)-phase field, for 2 h, then the α phase precipitates on the four (111) planes of the massive γ following the Blackburn OR:

$$(0001)_{α2} // \{111\}_γ \text{ and } <11\bar{2}0>_{α2} // <1\bar{1}0]_γ \tag{3}$$

The fine microstructure with $α_2$ plates rotationally precipitating in the γ matrix with an angular separation of 60° between them is called a "convoluted microstructure" [28, 45].

2.1.3 β → α transformation with the assistance of boride

Boron is an important alloying element in TiAl alloys. The addition of B leads to the formation of borides. There are four types of borides: TiB (B27 structure), TiB (B_f structure), Ti_3B_4 ($D7_b$ structure) and TiB_2 (C32 structure) [46].
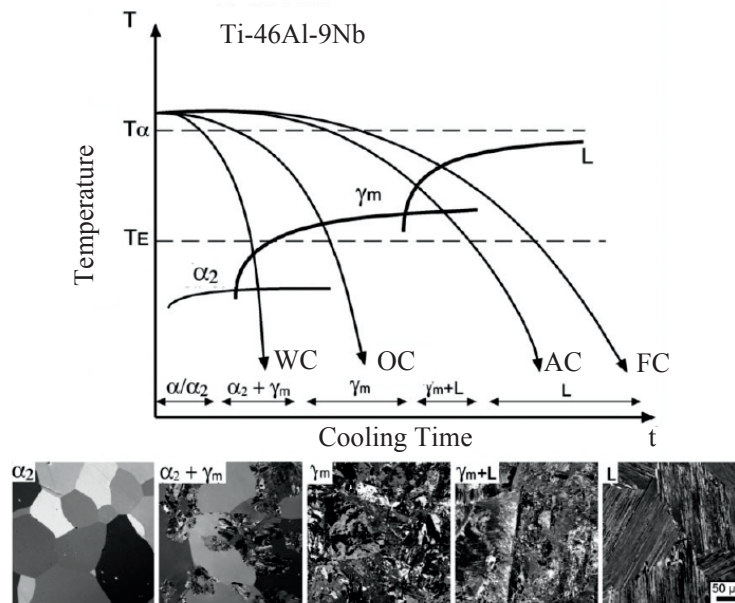
Figure 7: Schematic CCT diagram of a high-Nb-bearing γ-TiAl-based alloy, showing the microstructures that form as a result of different cooling rates [44]. γ_m: massive γ. L: lamellae. WC: water cooling. OC: oil cooling. AC: air cooling. FC: furnace cooling.
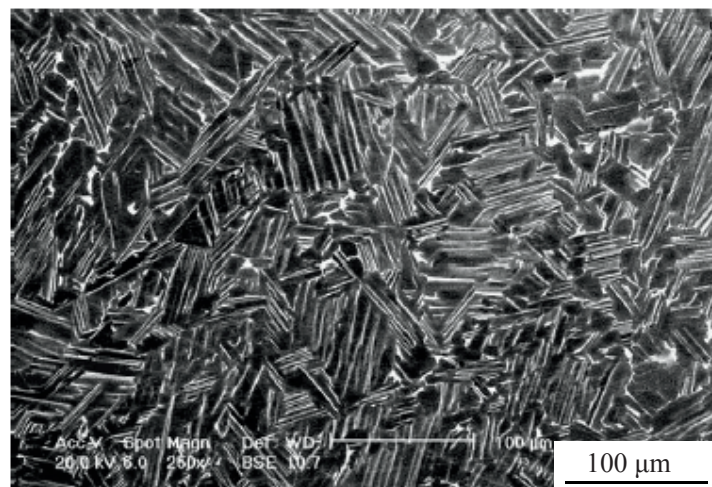
Figure 8: BSE micrograph of a sample of Ti–46Al–8Nb taken from a 20 mm diameter sample cut from an ingot, oil quenched to room temperature from 1360°C and aged at 1320°C for 2 h, exhibiting a typical convoluted microstructure [28].

Borides are found to present various orientations in the interdendritic regions of β grains and lead to microstructure refinement. In β-solidifying alloys, more than 0.1 at% of borides is sufficient to provide heterogeneous nucleation sites for α during β → α transformation [47, 48]. Hu [25] and Hecht [48] have demonstrated the refinement achieved by boride-assisted α-phase nucleation during β/α transformation at a slow cooling rate. The mechanism for this refinement has been explained as strong constitutional undercooling in the segregation zone, which is attributed to the pronounced partitioning of boron and leads to the formation of

many nucleation sites in the interdendritic spaces during solidification [49]. The grain refinement induced by boride depends strongly on the cooling rate from the β-phase region. Recent studies conducted by Liu [21] and Oehring [27] indicate that the heterogeneous nucleation of α on borides may be suppressed by high cooling rates. For peritectic alloys, grain refinement occurs only when the addition of borides is above some critical threshold, approximately 0.5-0.7 at%, and interestingly, the addition of a larger amount of boride does not further increase the refinement [50]. The refinement can be described as a switch on/off effect caused by the addition of borides. It has been found that borides are likely to provide heterogeneous nucleation sites for peritectic α, leading to randomly oriented α and grain refinement [51].

The ORs between borides and the solid α and β phases are also a subject of intensive research. It has been reported that the OR between boride and β can be described as follows: $\{011\}_{\beta}//(001)_{B27}$ and $<111>_{\beta}//[010]_{B27}$. Additionally, there are many ORs between α and borides, such as $(0001)_{\alpha}//(001)_{B27}$ and $<11\bar{2}0>_{\alpha}//[010]_{B27}$, as reported by Hu [25, 51] and Hill [52]; $[0\bar{1}11]_{\alpha}//[\bar{1}04]_{B27}$ and $[2\bar{1}\bar{1}0]_{\alpha}//[010]_{B27}$, as reported by Genç [53]; and $(1\bar{1}01)_{\alpha}//(001)_{B27}$, $(11\bar{2}0)_{\alpha}//(010)_{B27}$ and $(1\bar{1}0\bar{2})_{\alpha}//(100)_{B27}$, as reported by Banerjee [54]. The differences among the ORs between borides and the β and α phases lead to further grain refinement.

2.1.4 *In situ* observation of phase transformations via HEXRD

HEXRD is considered to be a good choice for investigating the bulk properties of engineering materials because of its high intensity and large penetration depth. It can achieve not only high spatial resolution with a very small beam size but also high time resolution when combined with a fast detector, and these capabilities provide many opportunities for *in situ* experiments [55].

The *in situ* observation of phase transformations in γ-TiAl-based alloys by means of synchrotron radiation is an effective approach to understand how these transitions proceed during heating and solidification. As reported by Shuleshova [56], 15 alloys in the Ti-Al-Nb system have been designed and remelted in an electromagnetic levitator apparatus at the ESRF to observe their liquid–solid phase equilibria. The phase transformations can be analysed by synchronising the diffraction spectra and temperature. By calculating the scattering vector q, which is independent from the instrumental parameters and is defined as follows,

$$q = 4\pi \sin(\theta)/\lambda \qquad (4)$$

it is possible to identify different phases. Figure 9 provides an example of the solidification from the liquid state to β + α and the remelting to the liquid state. The β solidification and

the $\beta \rightarrow \alpha$ transformation temperatures can thus be determined. Another *in situ* observation of phase transformation has also been performed by Babu [57], who investigated the solidification during the welding of Fe-C-Al-Mn steel. Typical diffraction peaks of $(111)_{fcc}$ and $(110)_{bcc}$ are represented in the image to illustrate the variation in the primary solidification phase depending on the chemical composition and cooling speed.
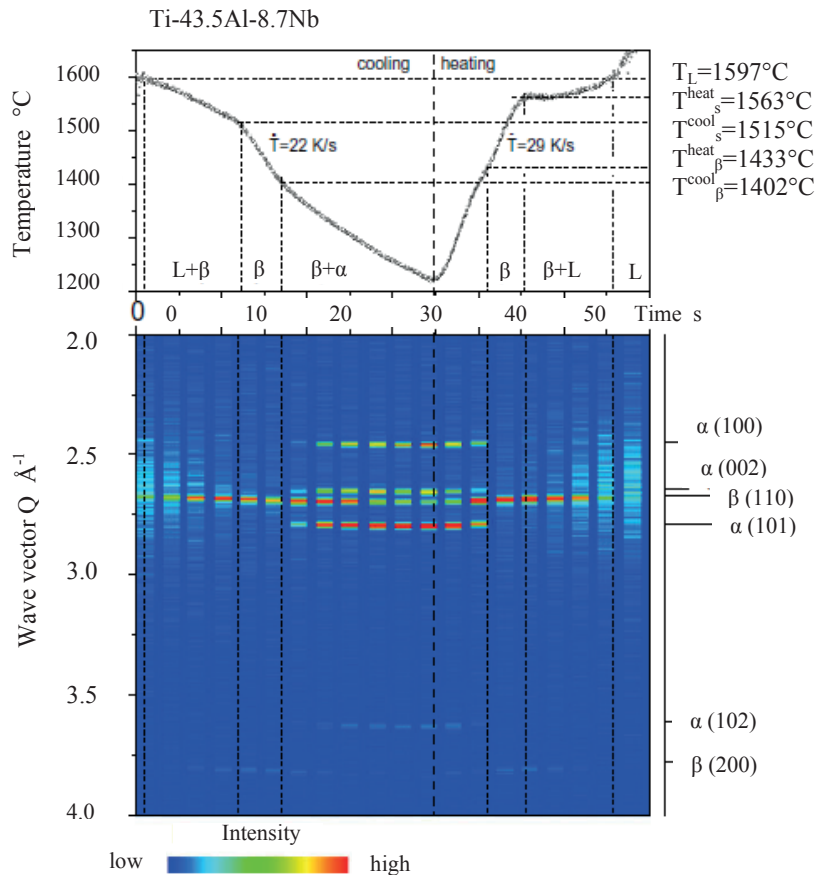
Figure 9: Time evolution of the temperature and the X-ray diffraction spectra during a solidification cycle of the Ti-43.5Al-8.7Nb alloy. The temperature–time profiles (top) are synchronised with the spectra (bottom) for the typical cooling and heating stages of the solidification cycle. The brightness in the intensity maps corresponds to the diffracted radiation intensity. The Bragg peaks of the crystalline phases are assigned at the right-hand side [56].

2.2 Heat treatments

Heat treatments are typically applied during the welding process to ensure the quality of the weld and improve its mechanical properties. Several types of heat treatments, such as pre-heating, *in situ* heating and post-weld heat treatments, can be performed using either a defocused laser or a furnace. The effects of such heat treatments are discussed in the following.

2.2.1 **Pre-weld and *in situ* heating**

Several studies concerning the fusion welding of γ-TiAl-based alloys have been conducted by Chaturvedi [11], Chen [12], Xu [58], Arenas [20, 59, 60] and Resgen [61]. All these publications report either solidification cracking or solid-state cracking in the weld. It has been found that pre-heating is an effective method of reducing the crack frequency [22, 61]. The relation between the cooling rate and the cracking frequency has been investigated, as shown in Figure 10, where the cracking frequency and the volume fraction of the retained α phase in the weld are plotted as functions of the cooling rate. It has been demonstrated that the sudden drop observed in the cracking frequency is almost entirely attributable to the decrease of the cooling rate below 660°C/s. As mentioned in chapter 2.1.2, the decomposition of the α phase also depends on the cooling rate. A high cooling rate produces a high volume fraction of the retained α phase, which is very brittle. It is observed that the crack frequency is lower when the weld contains a smaller amount of the brittle α phase. The cooling-rate threshold for crack-frequency reduction has been determined to be between 660 K/s [58] and 560 K/s [60].
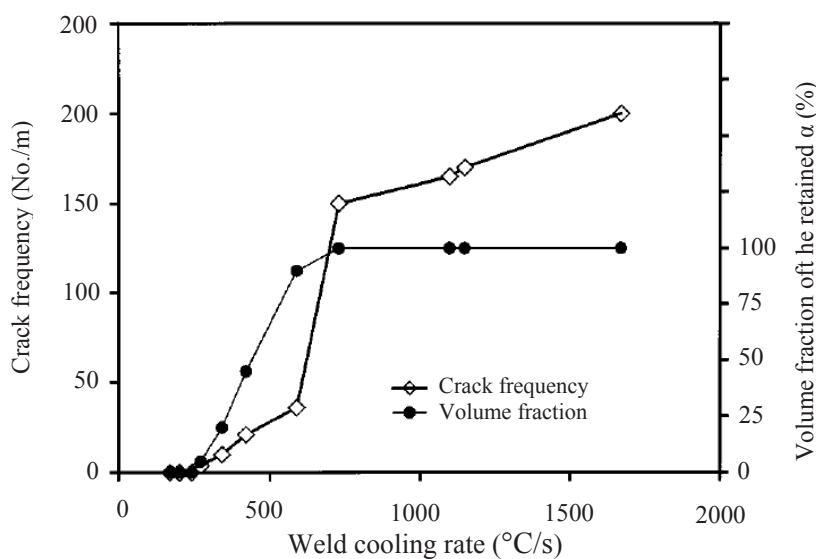
Figure 10: The weld crack frequency and the volume fraction of the retained α phase in the weld *vs.* the calculated cooling rate [58].

There are several methods of reducing the cooling rate. First, it is common to preheat the specimen using either a furnace or a defocused laser to above the brittle-to-ductile transition temperature [9, 11, 19, 29, 61]. Second, a ceramic material can be laid under the weld to serve as heat insulation and a heat reservoir to prolong the high-temperature stage and promote phase transformation [12]. Third, an *in situ* post-weld heat treatment can be applied by traversing the weld with a defocused laser [9] or electron beam to reheat the weld immediately after welding. Fourth, the specimen can be allowed to remain in the furnace and undergo furnace cooling. Using these methods, the cooling rate can be effectively reduced.

2.2.2 Post weld heat treatment

There are large amounts of the α_2 phase and residual stress in the welding zone. Heat treatments are applied to obtain a chemically homogeneous microstructure with balanced tensile properties with respect to creep resistance at both RT and high temperatures.

Figure 11 illustrates the relation between the temperature and the microstructure when the alloy is heat treated within the α- and ($\alpha + \gamma$)-phase fields and cooled down in an equilibrium state. Depending on the heating temperature, such heat treatments can lead to fully lamellar, nearly lamellar γ, duplex and near-γ microstructures [62]. If the heat treatment is performed at a temperature above T_α, a fully lamellar microstructure is produced (Figure 11 (a)). This occurs when α grains decompose into α_2 and γ lamellae as follows: $\alpha \rightarrow \alpha_2 + \gamma$. If the material is heat treated below T_α, γ grains are precipitated at the grain boundaries of α. The γ-phase content can be calculated by applying the lever rule. When the temperature is slightly below T_α, heat treatment gives rise to a nearly lamellar microstructure (Figure 11 (b)). When the temperature is between T_{eu} and T_α, heat treatment leads to a duplex microstructure, meaning that the volume fractions of γ grains and lamellar colonies are nearly identical (Figure 11 (c)). If the alloy is heated to slightly above T_{eu} and then slowly cooled, this treatment results in a near-γ microstructure (Figure 11 (d)).

Investigations of tensile properties and fracture modes can shed light on the relations between microstructures and mechanical properties. As shown in Table 1, a fully lamellar microstructure exhibits relatively high fracture toughness and creep resistance but poor RT tensile ductility [63]. Comparably equiaxed near-γ and duplex microstructures with only a small amount of lamellar colonies exhibit low fracture toughness and creep resistance but moderate tensile ductility at RT. A nearly lamellar microstructure exhibits balanced properties [3].

In the research of Schwaighhofer [23], systematic heat treatments have been applied to the TNM alloy to investigate the relations between microstructural constituents and mechanical properties. The results are summarised in Table 2. The presence of β and γ is found to retard α-grain growth and lead to refined lamellar colonies when the alloy is heated to near the γ_{solvus} temperature (Figure 12). The yield and tensile strength of the specimens of lamellar microstructures are closely related to the interlamellar spacing and colony size. A coarsening of the interlamellar spacing substantially reduces the strength of TiAl alloys and their creep resistance at high temperature [63-65]. The presence of the B2 phase at colony boundaries is also found to be effective in improving the RT yield strength because of the refined lamellar size. The RT ductility is increased by the formation of globular γ grains, and high creep resistance can be achieved in the presence of a large volume fraction of lamellae of fine α_2/γ lamellar spacing.
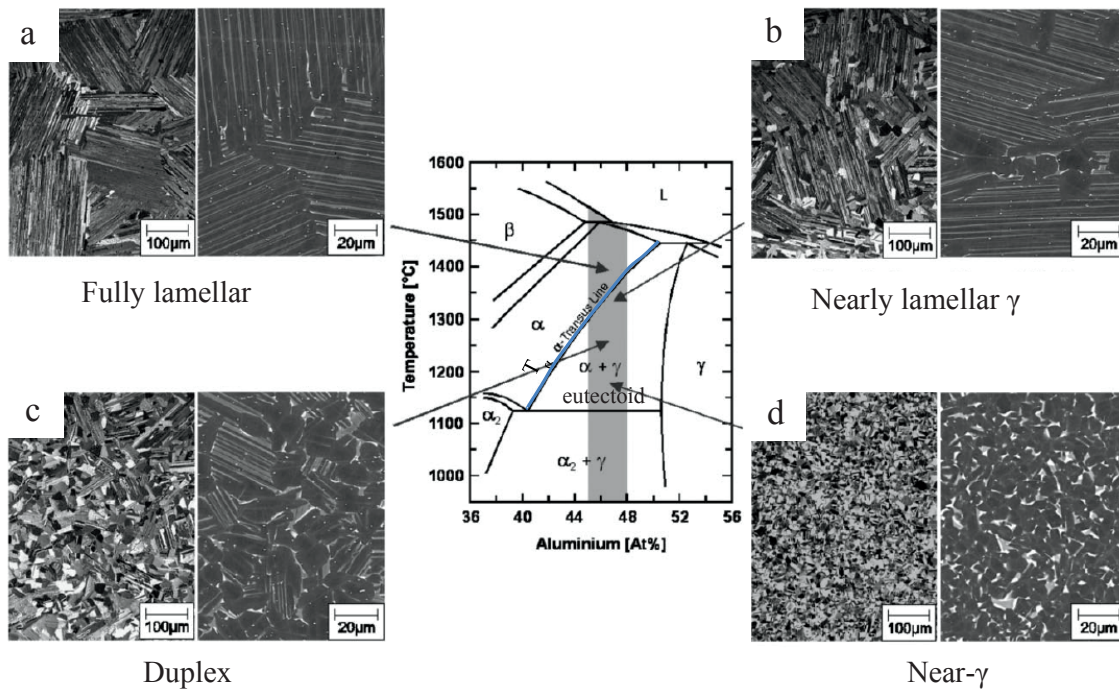
Figure 11: Mid-section of the binary Ti-Al phase diagram and representative microstructures obtained via heat treatments within the α- and (α + γ)-phase fields [62]. The blue curve in the phase diagram is the α-transus line, and the α-transus temperature is T_α. The left half of each microstructural image presents a light optical microscope image, whereas the right half is an SEM image acquired in BSE mode, i.e., γ-TiAl appears dark, whereas α_2-Ti$_3$Al appears as a light contrast.

For the attainment of a better understanding of the relation between the fracture mechanism and the microstructure, considerable attention has been directed towards the near-γ microstructure [29]. It has been reported by Nieh [66] that for a highly strained γ-TiAl-based alloy deformed at a low strain rate and a temperature near 800°C, the most commonly considered mechanisms for superplastic flow involve GBS, accommodation via dislocation slip, grain-boundary migration, recrystallisation and diffusional flow. Dislocation slip is the predominant mechanism of accommodation processes. The presence of a soft phase in the alloy can be beneficial in absorbing the dislocations induced by GBS to reduce the stress concentration and delay cavity formation [67]. It has also been found out that during creeping, these cavities nucleate at grain boundaries, triple points and ledges where there are stress concentrations and interfacial decohesion [68]. These cavities grow via stress-driven vacancy diffusion to the cavity–grain-boundary junction. The heterogeneous deformation between the hard α_2 grains and the comparatively soft γ phase induced by strain misfit is another source of cavity initiation [69].

In addition to investigations of the near-γ and duplex microstructures, it has been found that cracking is accompanied by ligaments and delaminations in the fine-grained fully lamellar microstructure. Investigations of compact tension specimens have revealed intact ligaments

in the wake of the crack tip when cracking propagates perpendicular to the lamellar normal direction [70]. For polysynthetically twinned (PST) alloys, cleavage fracture and delamination occur throughout the α_2 phase [71] and at the α_2/γ lamellar boundaries. Delamination separations occur parallel to the lamellar boundaries at the crack tip because of local stress concentrations in PST alloys [72, 73]. There is negligible resistance during the propagation of interlamellar cracking, whereas noticeable stress is needed when a crack grows across grain boundaries [73]. The resistance across the grain boundaries also depends on the misorientation between lamellar grains. Crack propagation across similarly oriented grains proceeds without difficulty. However, the propagation is arrested when the lamellae are unfavourably oriented [74]. Fine precipitations of β and γ particles along lamellar colony boundaries have also been reported to improve the translamellar toughness because the generated α_2/β and α_2/γ interfaces can effectively restrict dislocation motion [75]. Moreover,

Table 1: Assessment of microstructures with respect to creep resistance and RT ductility.

Property / Microstructure	Creep resistance	RT ductility
Fully lamellar	↑	↓
Nearly lamellar	Balanced properties	
Duplex	↓	↑
Near-γ	↓	↑

Table 2: Assessment of microstructural constituents that influence the mechanical properties of TNM alloys. The comparison is valid for random orientations of the α_2/γ colonies [23]. The symbol $+ +$ $(- -)$ represents a strong positive (negative) effect, and $+$ $(-)$ represents a positive (negative) effect on the property. The symbol $\times$ indicates no influence or correlation.

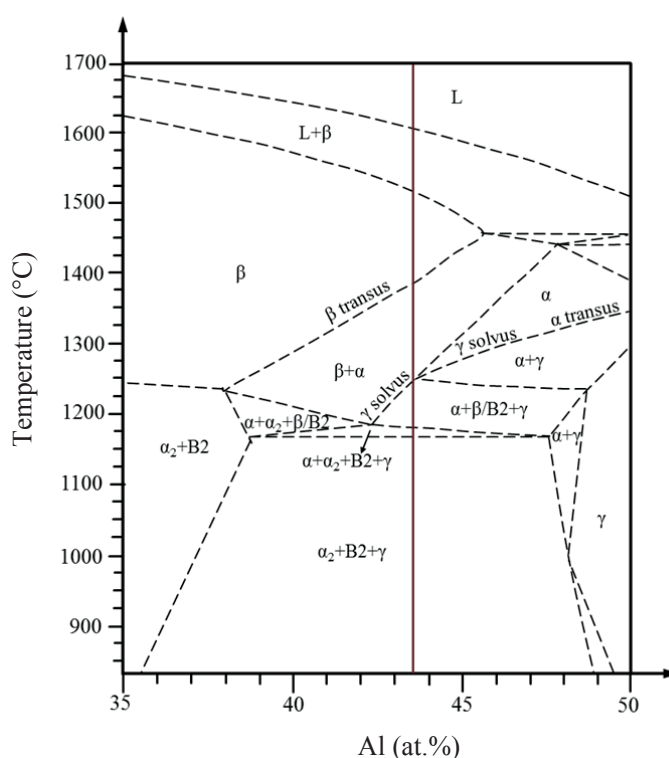| Microstructural parameter	Mechanical property			
	Suppression of grain growth	RT yield strength	RT ductility	Creep resistance
Small lamellar colony size	–	+ +	×	–
Fine lamellar spacing	×	+	×	+
Large α_2/γ lamellar colony fraction	–	+ +	–	+ +
B2 phase at colony boundaries	+ +	+	×	–
Globular γ grains	+ +	– –	+ +	– –

Figure 12: Experimental phase diagram of the alloy Ti–×Al–4Nb–1Mo–0.1B [23].

the size of the boride precipitates has a significant effect on the tensile ductility. Alloys with fine titanium boride precipitations exhibit good ductility because of the refinement in grain size. Large titanium boride precipitates induce debonding along the boride-ribbon/matrix interface, which causes premature tensile fracturing [76]. The simultaneous debonding of parallel lamellar interfaces caused by texture formation in cast alloys can also lead to cleavage fracture [77].

To summarise the above discussion, post weld heat treatment is important for the formation of optimised microstructures and to balance the mechanical properties of welds. The proper temperature and duration of heat treatment depend on the design criteria and the field of application.

2.3 Residual stresses

Residual stresses are always produced when a material is inhomogeneously elastically or plastically deformed in such a fashion that deformation incompatibilities arise [78]. Virtually no material, component or structure exists that is free of residual stress. Residual stresses are generated during material processing, such as cutting, deforming, casting, welding and laser surface hardening [79]. Some residual stresses are beneficial to the mechanical properties of materials, such as the retardation of fatigue crack growth caused by the laser surface heating of the aluminium aerospace alloy AA2198 [80, 81]. However, many residual stresses are detrimental to the structural reliability of materials. Thus, it is important to evaluate the

residual stresses and understand their origins to fabricate technical components with sufficient reliability.

2.3.1 Generation of residual stress

In welding, residual stress is observed both the longitudinal and transverse directions to the weld [9, 55]. The formation of residual stresses can be explained using the three-bar model [18], as illustrated in Figure 13. Three bars of the same length are rigidly connected by two blocks at either end. The bar in the middle represents the welding zone. During heating, the middle bar tries to expand, but its free expansion is constrained by the side bars. The compression stress vanishes when the middle bar is fully melted. As the middle bar begins to cool, the welding zone solidifies and shrinks, which causes compression on the side bars [18]. If the tensile stress on the middle bar exceeds its yield strength, the weld can be torn away, leading to cracking of the weld.

2.3.2 Residual-stress calculation via stress-free reference

X-ray diffraction is outstanding in its ability to non-destructively probe residual stresses within the subsurface and interior regions of components [82]. The underlying principal of X-ray analysis is the Debye-Scherrer technique. When the wavelength of a source of monochromatic radiation is of the same order as the interplanar lattice distance of a polycrystalline material, the interference lines of the specimen appear at discrete *2θ (h k l)* values [78]. In the past, several types of stationary diffractometers have been produced, with the X-ray tube and detector rotating on a focusing circle. In this method, the X-rays are diffracted by the surface layer of the specimen, and only the surface grains are measured. Because the penetration depth of the X-ray beam is low (only 2-14 μm, depending on the
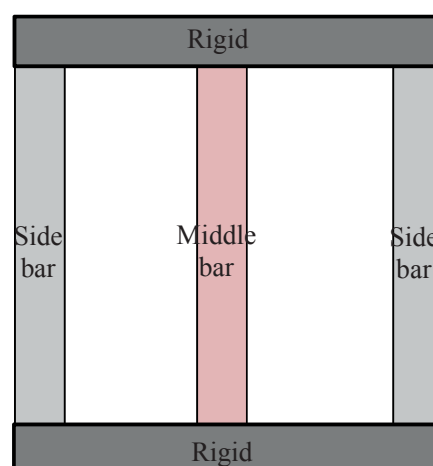
Figure 13: Schematic illustration of the three-bar model.

material and the diffraction plane [78]), it is assumed that the residual stress is in a plane-stress state.

At present, more powerful X-ray sources are available, such as synchrotron beams. Typically, a synchrotron beam passes through the material, and the measured stress is averaged over the entire sample thickness. The attenuation length of the X-ray beam can be calculated using the equation [83]

$$\tau_0 = 1/(\rho \cdot \Sigma) \tag{5}$$

where ρ is the density of the material and Σ is the mass-absorption coefficient. The photon energies in HEMS are typically 53.7, 87.1 and 100 keV. The penetration depth of the incident beam into TiAl is 6.5 mm when the photon energy is 53.7 keV. The thickness of the measured TiAl sheet is less than 2.5 mm, and therefore, the synchrotron beam passes through the material and the diffraction is averaged over the entire sample thickness.

The diffractions at the detector are integrated and fit with a Gaussian function, and the scattering angle 2θ is related to the lattice distance d and the wavelength λ by Bragg's equation:

$$d^{hkil} = \frac{\lambda}{2\sin\theta} \tag{6}$$

The superscripts (*h k i l*) correspond to different lattice planes. Variations in the stress-free interplanar lattice distance d_0 associated with changes in chemical composition are accounted for using a reference sample. The strain ε is related to the difference in lattice distance between the welded piece d and the stress-free reference d_0 by the following function:

$$\varepsilon^{hkil} = \frac{d^{hkil} - d_0^{hkil}}{d_0^{hkil}} \tag{7}$$

For a hexagonal structure, the "average" strains can be calculated using the lattice parameters for the a axis and the c axis:

$$\varepsilon_{ii}^{avg} = (2\varepsilon_{ii}^a + \varepsilon_{ii}^c)/3 \tag{8}$$

where i=xx, yy, and zz correspond to the LD, TD and ND, respectively. Finally, the macroscopic residual stress σ can be calculated using the three components of the residual strains and Hook's law:

$$\sigma_{ii}^{hkil} = \frac{E_{hkil}}{1+v_{hkil}}\left[\varepsilon_{ii}^{hkil} + \frac{v_{hkil}}{1-2v_{hkil}}\left(\varepsilon_{xx}^{hkil} + \varepsilon_{yy}^{hkil} + \varepsilon_{zz}^{hkil}\right)\right] \tag{9}$$

To ensure that the lattice-free parameter d_0 is not influenced by chemical variations, it is important to cut the stress-free reference sample from exactly the location at which the stress measurement is performed [82]. Figure 14 shows two reference samples, (a) a cube and (b) a

comb, produced via EDM. It is worth noting that the comb was cut transverse to the weld to obtain the d_0 values in the base material, heat affected zone and welding zone.
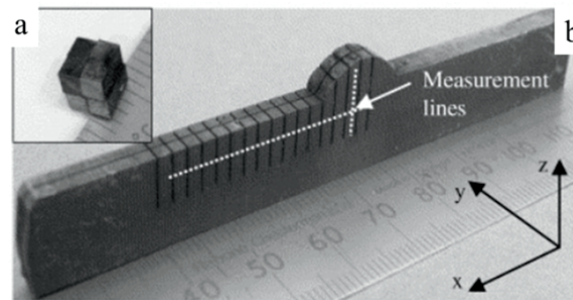

Figure 14: Specimens — (a) a set of cuboids and (b) a comb — used to determine the "stress-free" parameter d_0 [82].

3 Experimental

3.1 Material

Because there are many types of γ-TiAl alloys, three representative types of material were chosen for the welding studies presented in this thesis: γ-TAB, Alloy 2 and TNB-V5. The chemical compositions of these materials are listed in Table 3.

Table 3: Chemical compositions of the investigated alloys, in units of at%.

Material	Ti	Al	Cr	Nb	Mn	Mo	B	Si	C
γ-TAB	47.8	48	1	1.5	1	–	0.5	0.2	–
Alloy 2	53.3	42	2.5	1	–	–	0.5	0.7	–
TNB-V5	49.6	45	–	5	–	–	0.2	–	0.2

The production methods for these three alloys are presented in detail in the following.

1. The γ-TAB material was produced using a powder metallurgical approach by means of gas atomisation (PIGA) at HZG. The powder particles were degassed and hot isostatically pressed. The pressed material was rolled into sheets of 2 mm in thickness and cut via EDM into plates of $25 \times 25 \times 2$ mm^3. The plates were subsequently cleaned to remove oxides.

2. Alloy 2 was acquired from company GfE in a cast state. It was an internal designed alloy in this company, so that there is no trade name for it. It was cut via EDM into discs and finally laser cut into plates of $13 \times 20 \times 2.7$ mm^3.

3. The TNB-V5 material was casted at HZG and it was extruded into a cylindrical rod. Plates of $25 \times 50 \times 2.5$ mm^3 were cut by EDM.

As TiAl alloys are very expensive, the first experiments were performed using easily available alloy, γ-TAB, as it was produced in HZG. Meanwhile, the composition of γ-TAB alloys is similar to the alloy used for GEnx^{TM} engine (composition Ti-48Al-2Cr-2Nb). A welding study is carried out to investigate the weldability of this alloy to obtain a first insight. Subsequent welding experiments were conducted using the alloy 2 and TNB-V5 alloys, which were manufactured at a later time. It is important to note that the alloy 2 and TNB-V5 are both 3rd generation alloys, they share similar phase-transformation paths. The knowledge gained from the early studies of alloy 2 could therefore be utilised in the subsequent investigations.

By using three alloys, this thesis provides a degree of freedom to compare the microstructures of various alloys under different welding methods. The experiment starts

with the 2nd generation TiAl alloy, γ-TAB, and follows by the 3rd generation alloy 2 and TNB-V5 alloys.

3.2 Laser beam welding and heat treatments

Four different types of laser beam welding processes were performed, namely, (1) heating using resistance furnace, (2) heating using induction furnace, (3) dual-laser-beam heating and welding and (4) FLEXILAS experiment. The experiment for the flexible *in situ* synchrotron observation of the laser beam welding process is titled FLEXILAS. The objective of the welds and their heat treatments was to produce crack-free, high-quality welds with an understanding of the phase transformations. At the same time, a faster and more reliable welding process was sought.

3.2.1 Heating using a resistance furnace

To heat the specimen homogeneously above the brittle-to-ductile transition temperature and reduce the cooling rate, the plates were fixed in place by a clamping jig and preheated in a furnace, which was filled with argon to protect the specimen from oxidation, as shown in Figure 15 (a). A robot operated a Rofin Nd:YAG solid-state laser (maximum power: 3300 W) and welded perpendicular to the specimen surface to perform key-hole welding after the specimen was pre-heated to 750°C (Figure 15 (b)). The heating time is 2 hours and the specimen was hold at 750°C for 10 minutes until the temperature is homogenised. The welding was performed with the laser of 200 mm focus length on the specimen surface. Afterwards, the specimen remained in the furnace for furnace cooling, which takes around 3 hours until it reaches RT.

3.2.2 Heating using an induction furnace

The second welding experiment was conducted using an induction furnace, which could heat the specimen to 800°C. A Trumph carbon dioxide laser (maximum power: 2600 W) was applied during the welding process. As shown in Figure 16, the welding plates were heated using an induction furnace, which was filled with argon to protect the plates from oxidation. The residual oxygen content in the welding atmosphere was detected by an oxygen-measuring instrument placed inside the chamber, and each joining procedure was performed at oxygen content below 100 ppm. Helium was used as the working gas and was injected into the chamber from the top. The clamping jig is made of a Macor machinable glass ceramic, which is flexible to cut and mill. Unlike metals, it is not heated during welding as it is not inductive. The temperature of each specimen was measured using a K-type thermocouple, which was arc welded to the heat-affected zone, and the data were recorded by the associated output instrumentation. The heating rate of the furnace is 80°C/min. The shortcoming of the facility is the restriction in complex clamping design. As it is made of glass ceramic, it is possible to manufacture a single piece but it is difficult to assemble

different the parts together. Moreover, the peak heating temperature of the specimen is limit because the clamping jig is oversized than the specimen.

3.2.3 Heating using a defocused laser

This experiment was performed using a dual-laser-beam experimental set-up. The plates were positioned in a chamber that was filled with argon to protect the specimen from oxidation. Helium was used as the working gas, and it was injected from the welding cone. Two laser beams were simultaneously generated by two Rofin Nd:YAG laser operation stations (power outputs P_1: 0–2200 W and P_2: 0–3300 W). The focal lengths of the welding
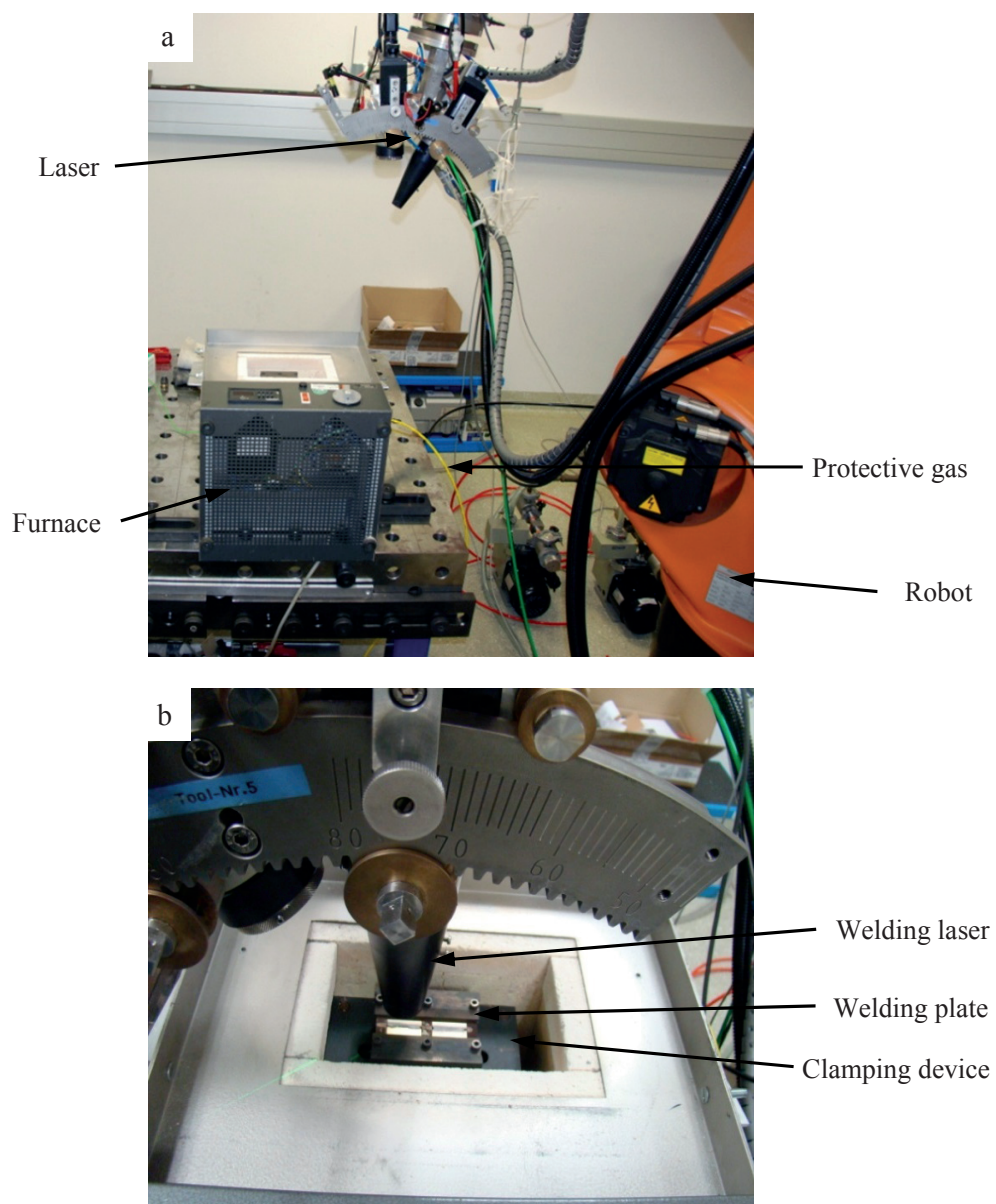
Figure 15: (a) Experimental set-up for furnace heating and welding and (b) a detail view of the welding with a focused laser perpendicular to the specimen surface.
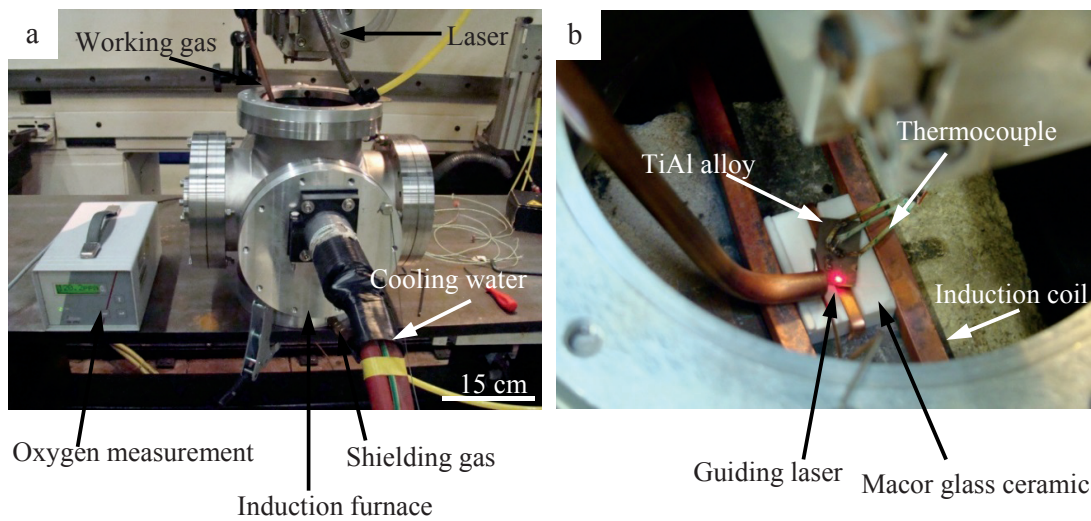
Figure 16: (a) Experimental set-up for induction-furnace heating and (b) welding details for thermocouple temperature measurements. Induction heating experiments were carried out in Fraunhofer Institute for laser technology.
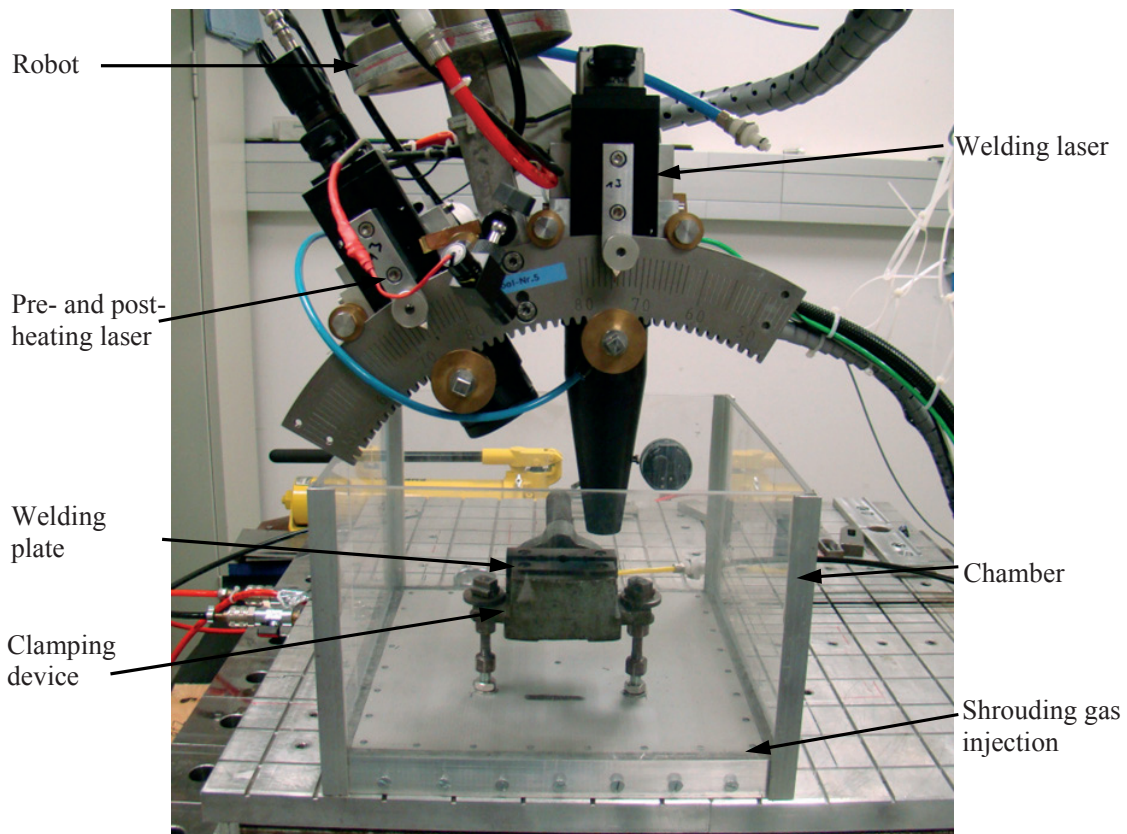
Figure 17: Dual-laser-beam welding set-up.

and heating optics were 200 mm and 120 mm, respectively. The laser was focused on the specimen surface during welding. A KUKA robot was used to control the movement of the laser beam (Figure 17). To heat the welding line above the brittle–ductile transition

temperature prior to welding, the heating laser was defocused to a large spot size and used for whole-plate (d=60 mm) and local (d=20-40 mm) pre-heating. Moreover, the defocused heating laser closely followed the welding laser to apply an *in situ* heat treatment. This heating was applied before the welded area had cooled. Then, post-weld heat treatments were applied using the heating laser with various beam diameters to heat the specimen to reduce the cooling rate along the welding line. The purpose of heating using a defocused laser was to flexibly control the local heating area and to avoid long heating times using a furnace to increase productivity. The total welding time is around 10 minutes.

3.2.4 FLEXILAS welding experiment

To investigate the phase transformation and residual-stress development during welding, a special chamber was designed for *in situ* laser beam welding, as shown in Figure 18. The FLEXILAS experiment was performed at the HZG beamline HEMS at DESY in the main station. The HEXRD measurements were performed in a transmission geometry. The incident beam was calibrated to a photon energy of 100 keV and had a cross section of 0.5×0.5 mm^2 to provide good lateral resolution. A 2-dimensional PerkinElmer detector was oriented strictly perpendicular to the incident beam. The specimen was mounted in a specially designed welding chamber, which was filled with Ar gas. The synchrotron beam entered through the entrance window and diffracted out through the exit window. The sample was mounted on a linear motion stage with a heating element. An IPG fibre laser (maximum power: 8 kW) was mounted in a fixed position in the chamber and aligned perpendicular to the specimen surface to achieve full-penetration local melting. The focal length of the welding optics was 250 mm, with the laser focused on the specimen surface. The angle between the specimen longitudinal direction and the synchrotron beam is denoted by ψ. Running water is pumped inside the water tube to adjust the temperature of the clamping, beam stop and laser optic, so that none of these parts can be superheated. Especially after welding, the water system is helpful to bring out the excessive amount of heat and accelerate the cooling stage.

Figure 19 shows details of the FLEXILAS set-up. For *in situ* phase-transformation observations, the synchrotron beam and laser beam were adjusted to the same position in the middle of the plate, and the synchrotron beam was tilted at an incidence angle of $\psi=45°$ with respect to the specimen surface (Figure 19 (a)). The synchrotron beam was then transmitted through the melt. As the synchrotron-beam cross section was significantly smaller than the observed melted zone, it is reasonable to assume that the X-ray beam penetrated solely the molten zone after the keyhole was established (Figure 19 (b)). Thus, any overlap between the melt zone and the surrounding solid phase within the diffraction region can be neglected. After the experiment, the recorded Debye-Scherrer diffraction rings were azimuthally

integrated to obtain the diffraction patterns as functions of the scattering vector q, in accordance with equation 4.
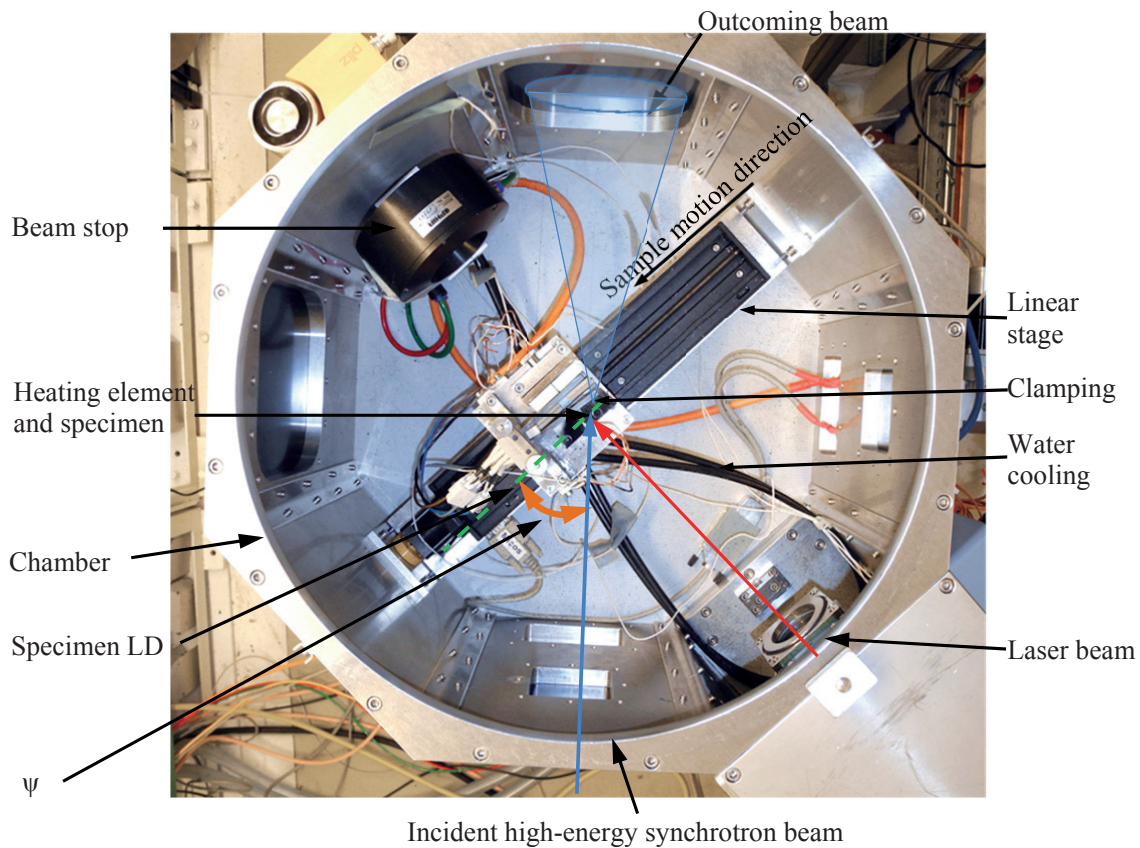
Figure 18: FLEXILAS welding chamber, top view (the symbol ψ represents the angle between the synchrotron beam and the specimen LD).
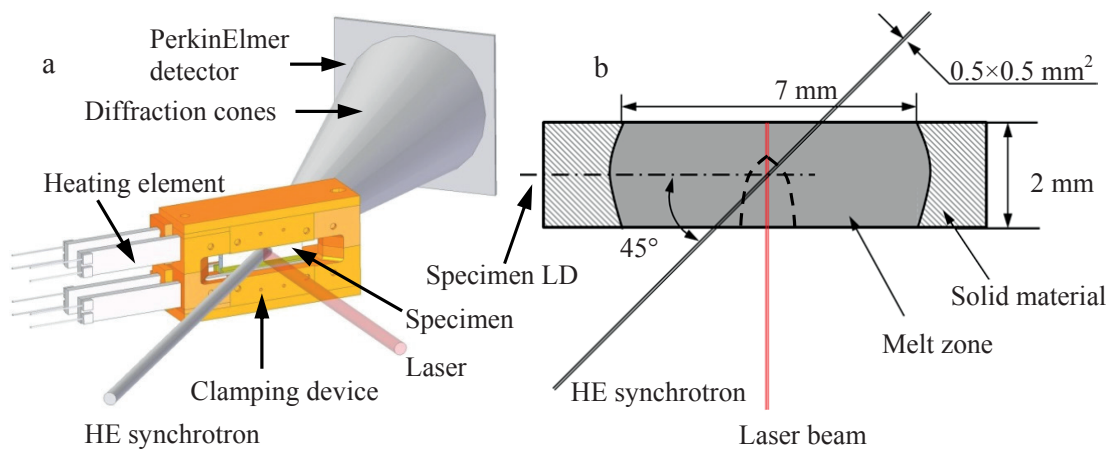
Figure 19: (a) Experimental set-up for the HEXRD *in situ* laser welding experiment. (b) Sketch of the geometry of the welding zone (top view) for phase transformation. Note that the melt zone of 7 mm in diameter developed during the late stage of the melting. The dashed line describes the shape of the melt zone in the initial stage.

3.3 Radiographic, microstructural and textural observations

Radiography experiments were conducted at HZG using a GE Isovolt 320/13 apparatus. Radiography is an imaging technique that uses X-rays to visualise the internal structure of an opaque object of non-uniform composition. An X-ray beam is produced by a generator and projected onto the object. Depending on the particular density and composition of the object, a certain percentage of the X-rays are absorbed by the object, and the rest are captured by a film. The difference in X-ray absorption is reflected by the contrast in the resulting image. Areas that absorb more X-rays appear as brighter regions in the image, and vice versa.

Microstructural and fracture-surface observations were acquired via SEM in the secondary-electron and BSE modes using a Zeiss DSM962 and a LEO Gemini 1530 microscope. The microscope is also equipped with EDS instruments for chemical composition analysis, EBSD instruments for textural examinations and the corresponding data-analysis software.

3.4 Residual-stress measurement

The residual stresses in the butt joint samples were determined using X-ray diffraction at the HZG beamline HEMS at DESY, Hamburg. The incident beam was calibrated to impinge on the plates in transmission mode and be diffracted by 2D Debye-Scherrer cones onto the detector behind it (Figure 20). The detector was oriented strictly perpendicular to the incident beam, and the distance between the sample and the detector distance was adjustable between 800 and 1200 mm. The cross sections of the monochromatic beam were tuned between 0.1×0.1 and 0.5×0.5 mm^2 to achieve either good spatial resolution or good time resolution. The as-welded specimens were covered with a thin layer of copper paste to calibrate the distance between the specimen and the detector and thereby avoid any error caused by specimen distortion.

A scan was performed across the weld seam, which was located in the middle of the weld. A comb-shaped reference sample (Figure 21) was machined out of a cross section of the fusion zone via EDM at the end of each welded specimen to determine the stress-free interplanar lattice distance d_0. It was assumed that the macro-stresses were relaxed in the comb "fingers". The strain was calculated by comparing the lattice parameters of the welded specimen and the stress-free comb, given as in Equation (7). A plane-stress state was assumed in the thin sheets. The entire pattern was fitted to calculate the strain and deduce the residual stress. The mean residual stresses were calculated by weighting the volume fractions of all phases. The diffraction pattern is sectioned into TD and LD. The residual stress in the TD was calculated by integrating the diffraction rings in two regions representing diffraction angles of -10 – 10° and 170 – 190°. Similarly, the residual stress in the LD was calculated by integrating the diffraction rings with diffraction angles of 80 – 100° and 260 – 280°.

One example of a diffraction pattern is presented in Figure 22 (a). In the calculation of the residual stress, the pattern is integrated to obtain the azimuthally averaged scattering intensity as a function of the diffraction angle 2θ to produce the plot shown in Figure 22 (b). The diffraction rings can also be integrated in reciprocal-space units of q, which is defined by the equation (4).
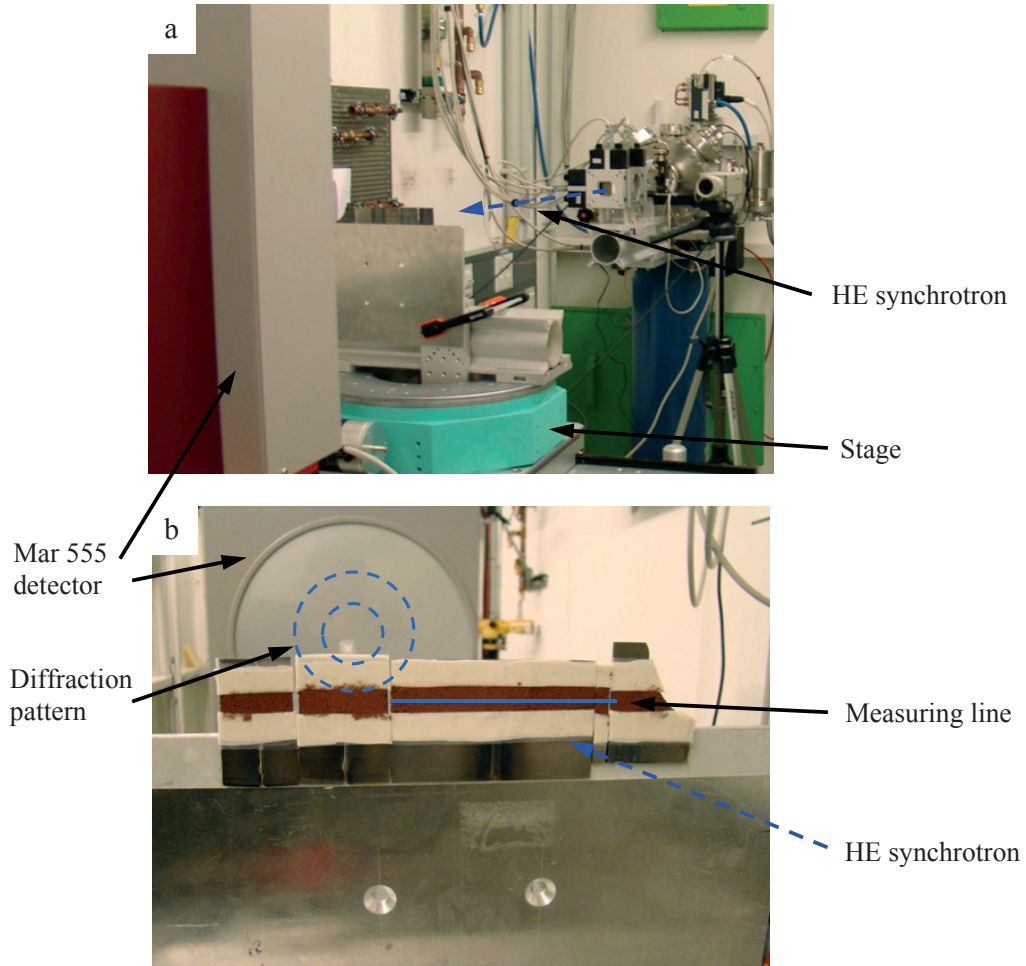

Figure 20: Residual-stress measurement set-up at DESY: (a) synchrotron beam and (b) samples and detector.
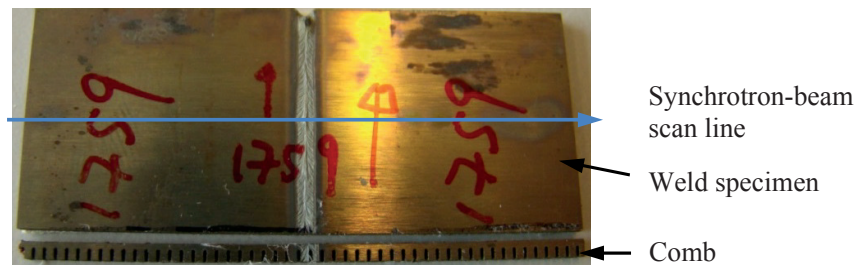

Figure 21: Electro-discharge machined comb used as a stress-free reference.
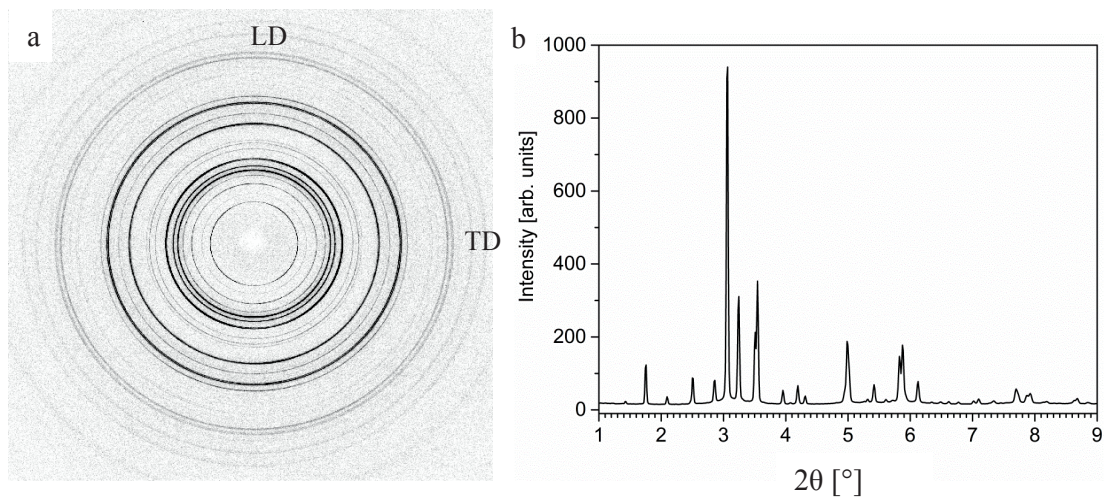
Figure 22: (a) An example showing the diffraction pattern of TNB-V5. (b) The pattern is integrated to obtain the azimuthally averaged scattering intensity as a function of the diffraction angle 2θ.

3.5   Tensile tests and micro-hardness tests

Tensile-test specimens were produced from the as-welded or heat-treated specimens. As shown in Figure 23, the micro-tensile specimens were electro-discharge machined with the welding seam centred with respect to the gauge length. The gauge dimensions of the test specimens were 27 mm × 5 mm × 1 mm. Here, 27 mm is the gauge length, which was used as the tensile direction. The specimens were ground using 2500# SiC paper to minimise microcracks on the surface.

For each configuration, three specimens were tested using a Zwick/Roell Z005 testing machine with a maximum tensile force of 5 kN (Figure 24). Each specimen was heated using an induction furnace manufactured by Linn High Therm, and the temperature is controlled by K-type thermocouple. The elongation was measured using a Fiedler laser extensometer. The tests were conducted using a constant cross-head speed for all tests.

The micro-hardness tests were carried out by HMV 2000 micro-hardness tester produced by Shimadzu company. For each indent a indenter load of 1 kp with a hold time of 20 s was used. The micro-hardness was measured across the base material, heat affected zone and welding zone, at the half of the sheet thickness, as shown in Figure 25.
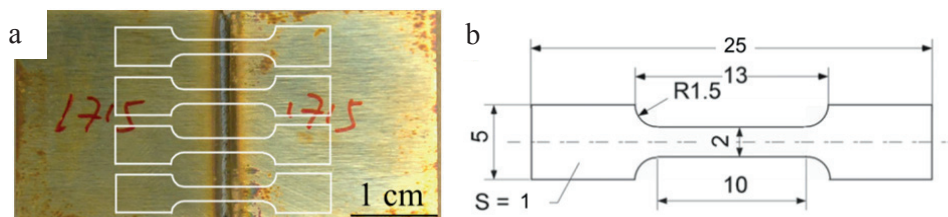

Figure 23: (a) A sketch illustrating the extraction of a tensile specimen from the middle of a weld. (b) Geometry of the micro tensile specimen. The unit is mm.
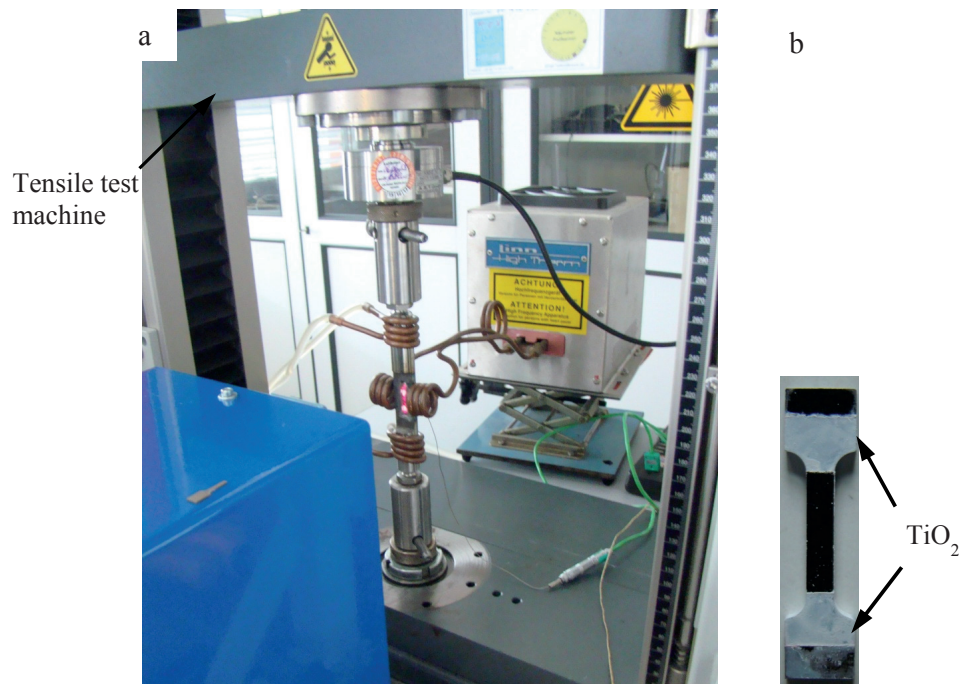
Figure 24: (a) Equipment for tensile tests and (b) a micro-tensile specimen. The length between the TiO₂ segments was measured using a laser extensometer during tensile testing.
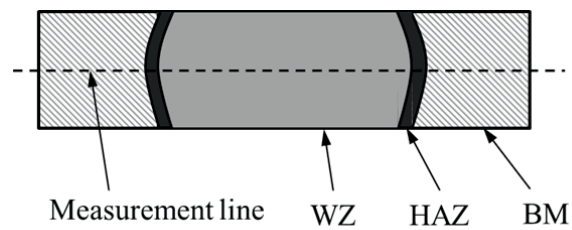

Figure 25: Micro hardness measurement position.

4 Heating using a resistance heated furnace

Chapters 4 through 7 introduce investigations aimed at systematically solving the technical problems encountered during welding. As mentioned in chapter 1, the first objective for TiAl welding is to achieve crack-free welds with the optimised microstructure, which is the primary focus of this chapter. The experiment starts with the γ-TAB alloy and a resistance furnace, which are already in hand. Pre-heating above the brittle-to-ductile transition temperature was applied to reduce the cooling rate. The microstructural transformations during heat treatments and fracture mechanisms are also investigated. The content of this chapter is published in [29].

4.1 Experimental parameters

As shown in Figure 15, γ-TAB alloy plates were clamped in a furnace, which was filled with argon to protect the specimens from oxidation. The first specimen was pre-heated to 750°C and welded using an Nd:YAG laser in the furnace, followed by furnace cooling (specimen #1). Another specimen (#2) was welded in the same manner as #1 and then heat treated in a vacuum furnace for 0.5 hour at 1350°C. The welding takes around 5 hours due to the low heating and cooling rate of the resistance furnace. All specimens were inspected via radiography to identify any defects, including cracks and pores in the welding zone.

The specimens were ground, followed by vibration polishing or electropolishing, to investigate the microstructure of each welded joint using SEM in BSE mode. The mean grain size was determined through observation of the SEM images. The evaluation method was to count the number of grains along a line of a certain length. The mean grain size was averaged from at least ten measurements. To measure the residual stresses in each butt-joint sample, the incident beam was calibrated to a photon energy of 87.1 keV, and it impinged on the weld plate in transmission mode. At DESY, one Mar detector, consisting of 3450×3450 pixels of 100 μm × 100 μm in size, was used. The cross section of the monochromatic beam was 0.2 mm × 0.2 mm to achieve good lateral resolution. A comb-shaped reference sample was machined for stress calculation. Please refer to chapter 2.3.2 and 3.4 for stresses evaluation.

The as-welded and heat-treated specimens were cut via EDM into flat micro-tensile specimens for the tensile tests. The tensile tests were conducted at 750°C in the laboratory air at an initial strain rate of 1.67×10^{-5}/s. At least three tests were performed in each condition, and the average values are reported. For the investigation of the microstructural and textural evolution during the tensile test, X-ray diffraction was applied at various positions on the fractured tensile specimens. The diffraction rings were unrolled into lines and azimuthally integrated. The azimuthal angle was defined to be equal to 0° along the

longitudinal direction (the direction of the weld seam) and to increase anticlockwise to a value of 360°.

4.2 Microstructural characteristics

The as-welded specimen #1 was investigated via radiography (Figure 26), and no cracking or macropores were observed. As shown in Figure 27 (a), the microstructure of the rolled sheet was found to be very homogeneous. The base alloy exhibited a near-γ microstructure with an average grain size of approximately 4 μm. The γ grains exhibited different contrasts at different grain orientations. The α_2 phase was discernible as small bright dots situated predominantly on γ/γ grain boundaries. A small amount of lamellar colonies was also observed between γ grains.

The welding zone was composed of coarse lamellar dendrites with small lamellar spacing, as shown in Figure 27 (b). The coarse dendrite arms could be as long as 60 μm. As a result of the high cooling rate during the welding process, the material was far from thermodynamic equilibrium. There were bright ribbons with curvy features, with the same morphology as borides [84], wrapped by dark layers lying in the interdendritic region. The microstructure in the interdendritic region appeared generally similar to the results of the investigation of Hecht [48], who quenched unidirectional solidified Ti-43Al-5Nb-0.2C-0.2B at the end of solidification. These findings could indicate that welding zone solidification begins with the nucleation of β, which then transforms into peritectic α through the process $L + \beta \rightarrow \alpha$, followed by α dendritic growth. During the final stage of solidification, the interdendritic region is enriched with the Ti-poor α phase, which is responsible for the dark contrast. The boride ribbons solidify during the final stage with the Ti-poor α phase in the interdendritic region.

Figure 27 (c) shows the microstructure of the welding zone after tensile tests at 750°C. The microstructure still consisted of coarse lamellar dendrites with fine lamellar spacing. This is compared with Figure 27 (b), additional microcavities were observed in the interdendritic region. These cavities seem to have resulted from the stress applied during the tensile tests.
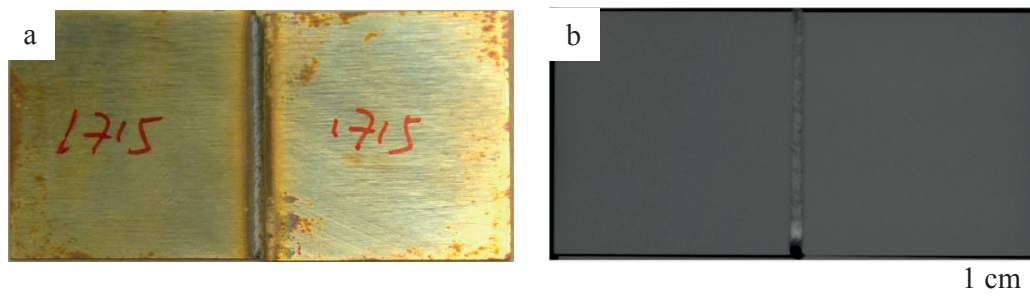

1 cm

Figure 26: (a) Example of a specimen welded in the furnace. (b) Radiography of the specimen.
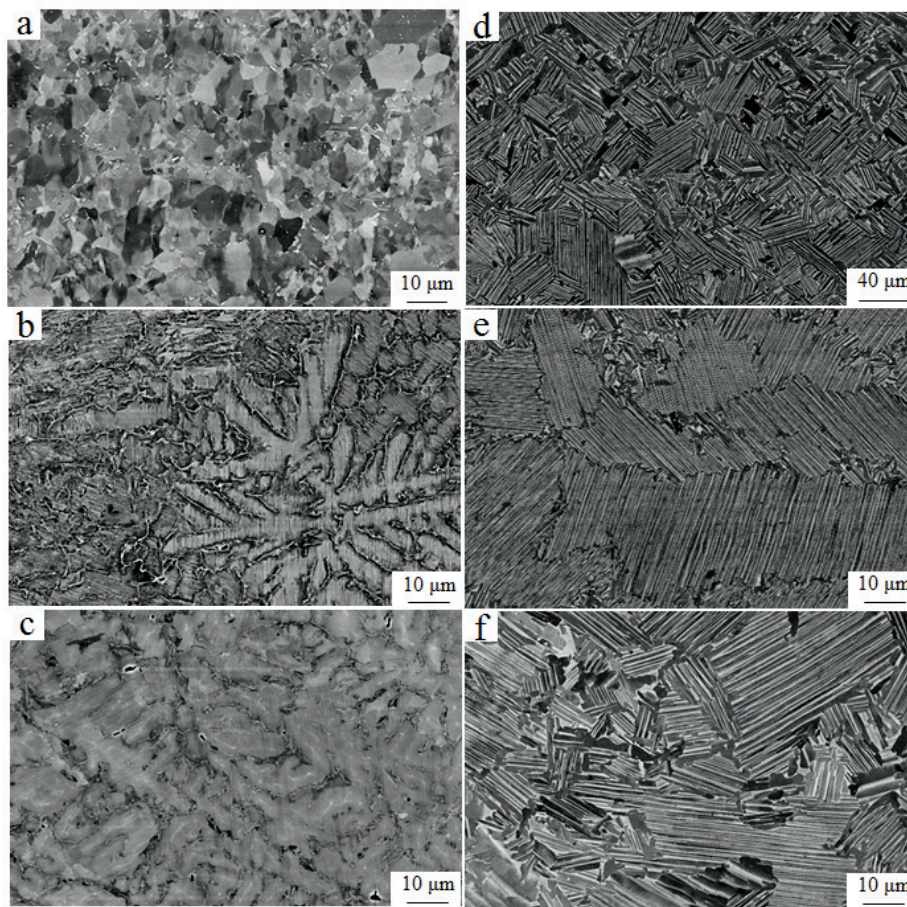
Figure 27: SEM observations of microstructures in BSE mode: (a), (b) and (c) are of the as-welded specimen, and (d), (e) and (f) are of the heat-treated specimen. (a), (d) base material; (b), (e) welding zone; and (c), (f) welding zone of the specimen after tensile testing.

Polishing revealed the presence and shapes of borides and silicides. Following vibration polishing, bright rods in the base material (Figure 28 (a)) and ribbons with curvy features (Figure 28 (c)) in the welding zone were observed, as indicated by arrows in the figures. It is well known that borides are mechanically removed by electropolishing [85], leaving elongated holes of approximately 3 μm in length in the base material and indentations in the welding zone. Moreover, in the base material, some round, bright particles at the γ grain boundaries disappeared following electropolishing, leaving the α_2 phase still in its original position. It can be inferred that round-shaped silicides exist in the base material together with the borides and are removed by the electropolishing process.

To produce an almost fully lamellar microstructure, laser-beam-welded TiAl alloys were heat treated in a vacuum furnace at 1350°C for 0.5 hour. As shown in Figure 27 (d), a metallographic examination of specimen #2, produced by such a heat treatment, indicated that the γ grains in the base material transformed into an almost fully lamellar microstructure. There were only a few γ grains individually situated at lamellar-colony boundaries. The

average colony size was coarsened to 16.7 μm. Coarse dendritic grains still remained in the welding zone (Figure 27 (e)), and the α_2-α_2 lamellar spacing measured via SEM was 0.87 μm, which is much thicker than the spacing prior to heat treatment. Many small equiaxed lamellar colonies were observed between the dendritic arms. These interdendritic colonies tended to grow more extensively during high-temperature tensile testing and lead to a refinement of the grain size in the welding zone, as shown in Figure 27 (f).

4.3 Residual stress measurement

The residual stresses of specimens #1 and #2 are presented in Figure 29 (a). The as-welded specimen presented a three-peak morphology (Figure 29 (d)), with three tensile-stress maxima symmetrically separated in the welding zone and heat affected zone, leading to compressive stress in the base material. The maximum tensile stress in the heat affected zone was approximately 480 MPa, which was 100 MPa higher than that at the welding zone centre. The stress decreased rapidly to negative values with increasing distance from the weld centre. The maximum compressive stress was -180 MPa at approximately 5 mm from the weld centre. Near the edge of the specimen, the residual stress was close to 0. After heat treatment in the furnace at 1350°C for 0.5 hour, the residual stress was almost entirely relieved, and the remaining peak stress was approximately 100 MPa in the heat affected zone.
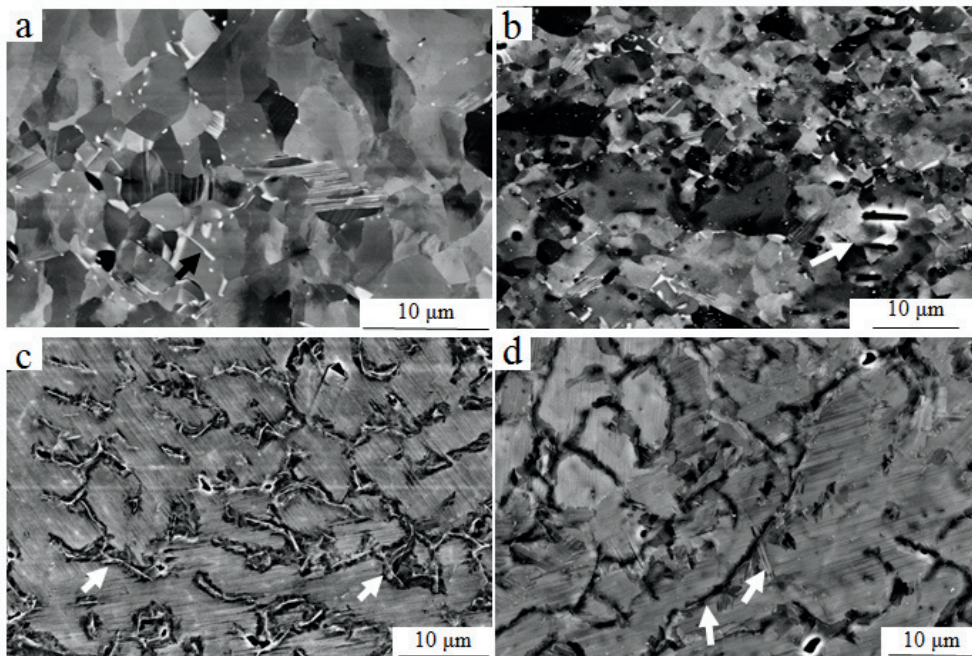

Figure 28: SEM observations of microstructures in BSE mode: the vibration-polished (a) base material and (c) welding zone of an as-welded specimen and the electropolished (b) base material and (d) welding zone of an as-welded specimen. The arrows indicate the presence of borides or boride indentations.

The residual stress in the as-welded specimen exhibited one tensile-stress maximum in the centre of the welding zone, whereas the other two, higher maxima appeared symmetrically in the heat affected zone. There was a sudden drop in the tensile stress of 200 MPa at positions of ±0.5 mm away from the weld centre. Close investigation of the microstructure revealed the reason for this sharp decrease in stress. The heat affected zone could be divided into two regions according to its different microstructural morphologies: the near-heat affected zone and the far-heat affected zone (Figure 30 (a)-(b)). The near-heat affected zone was closer to the fusion region than the far-heat affected zone, and it received more heat during welding than the far-heat affected zone. Figure 30 (c)-(d) presents the details of both regions at high magnification. The near-heat affected zone, of 40 μm in width, was composed of massively transformed and twinned γ (Figure 30 (c)). The borides displayed a morphology of curvy ribbons, which appeared similar to the welding zone. It could be inferred that the near-heat affected zone was partly melted during welding. The nearly random distribution of the borides indicates that the melting time of this region was very short and that the borides were therefore not able to flow into the interdendritic region. The excessive amount of heat input in the near-heat affected zone promoted dislocation movement and relieved the internal stress. On the other hand, the far-heat affected zone was farther from the welding zone and therefore less influenced by the heat source than the near-heat affected zone. It is reasonable to suppose that the peak temperature and the cooling rate in the far-heat affected zone were both lower than those in the near-heat affected zone. However, the temperature may have been sufficiently high that the far-heat affected zone was briefly in the $\alpha_2 + \gamma$ region, as indicated by the lamellar microstructure (Figure 30 (d)). It can be concluded that the differences in microstructure and stress in the two regions resulted from the reduction in heat input with increasing distance from the fusion line. In the far-heat affected zone, high stress remained, and this region consisted of a lamellar microstructure. However, in the massively transformed near-heat affected zone, the residual stress was reduced.

As mentioned above, the welding zone was composed of coarse lamellar dendrites with fine than that in the near-heat affected zone. However, the microstructural observations seem to be conflict with this fact, as massive γ was found to have formed in the near-heat affected zone, and the formation of such structures requires a higher temperature gradient than does the formation of lamellae. One possible hypothesis is that a single α_2 phase was formed in the welding zone directly after welding. Because of the slow furnace cooling from 750°C, atomic diffusion was activated in this region, and the γ lamellae precipitated from the α_2 [86]. This hypothesis could be verified through diffraction morphology analysis.

In the far-heat affected zone and the base material, the numbers of bright dots, which were previously identified as silicide, were far greater than in the near-heat affected zone. Silicide
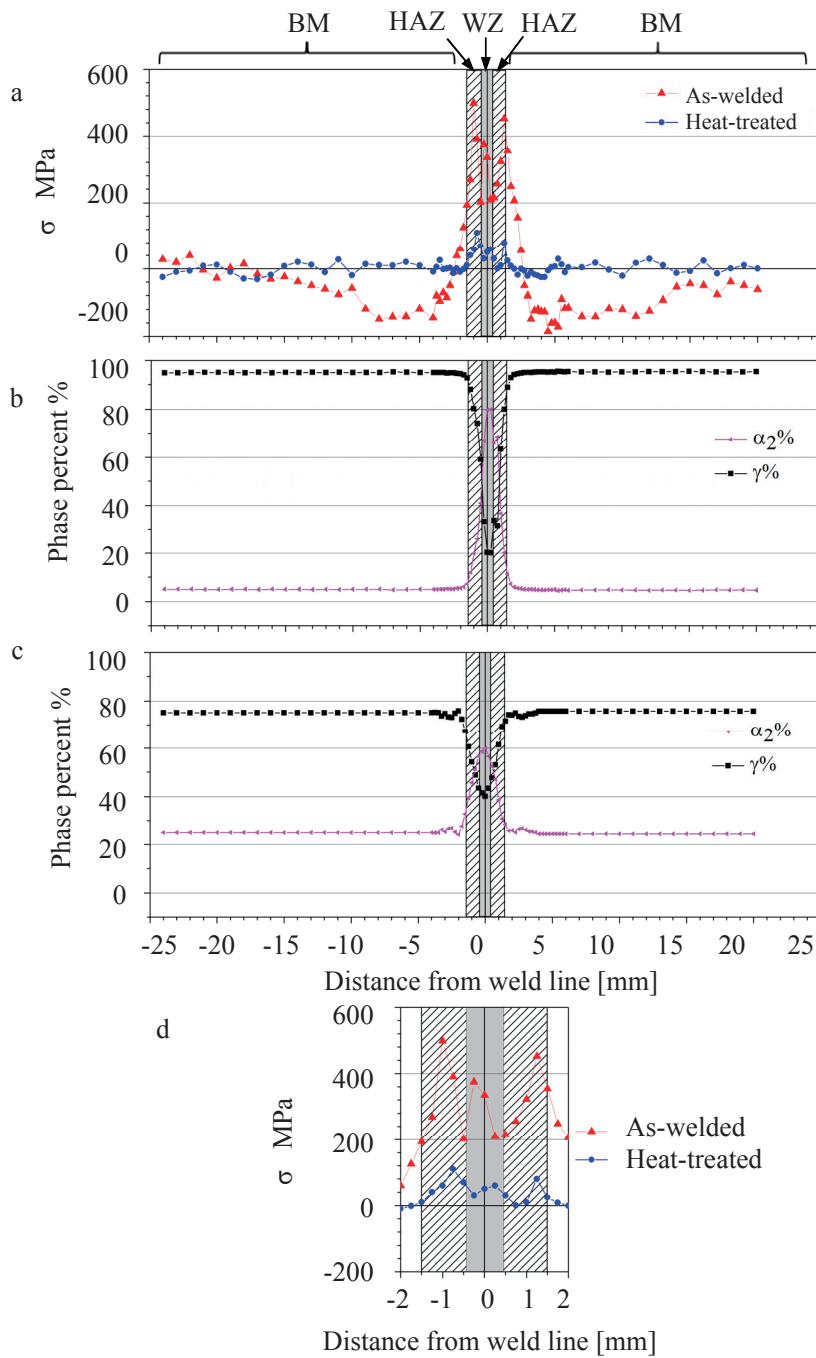
Figure 29: (a) Longitudinal stress maps along the welding lines of as-welded and heat-treated specimens. Phase distributions in the (b) as-welded and (c) heat-treated specimens. (d) The details of the residual-stress distributions in the welding zone and heat affected zone regions. BM: base material, HAZ: heat-affected zone, WZ: welding zone.

precipitates have been reported to be beneficial in improving creep resistance [87, 88]. They form in dissolved α_2 lath that has previously been bounded by γ lath of the same variety [88]. These precipitates act as effective obstacles to dislocation motion, such that the internal
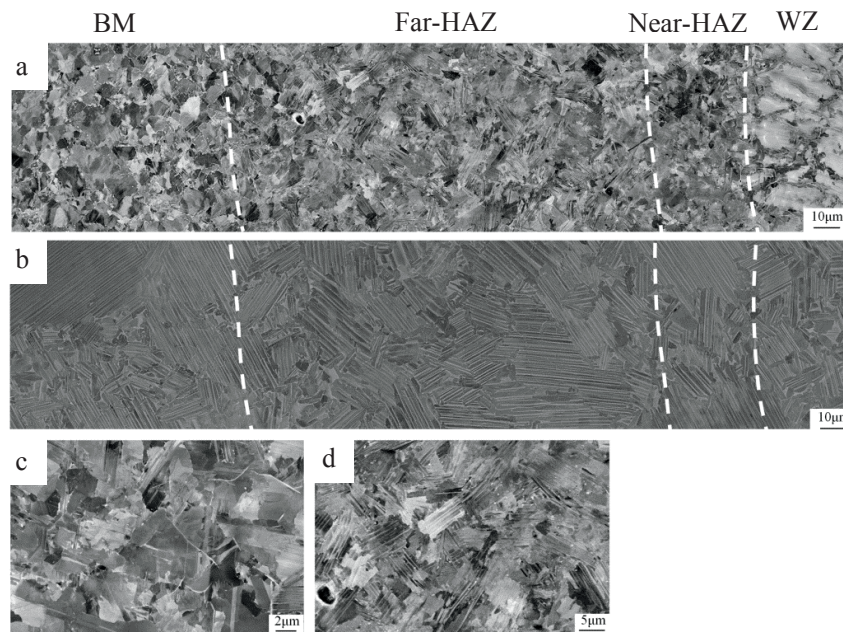
Figure 30: Microstructural observations of specimens in the welding zone, heat affected zone and base material regions of (a) as-welded and (b) heat-treated specimens. (c) near-heat affected zone and (d) far-heat affected zone of the as-welded specimen at high magnification. BM: base material. HAZ: heat-affected zone

stress cannot be easily relieved. Moreover, phase analysis via diffraction demonstrates that the welding zone consisted of 80% α_2 phase and 20% γ phase (Figure 29 (b)). Very little dislocation slip could be activated in the α_2 phase because of the limited number of dislocation systems, and therefore, the weld centre remained highly strained. Thus, it can be concluded that high stresses were formed by the welding process and that these stresses could not be eliminated because of the limited number of dislocation sliding systems in the α_2 phase and because of silicide precipitates pinning the dislocation motion in the far-heat affected zone. The residual stress in the near-heat affected zone, however, was relieved because of the heat-induced softening.

The phase composition and microstructure of the welded specimen were significantly modified after heat treatment for 0.5 hour at 1350°C. The heat treatment at 1350°C gave rise to a microstructure of predominantly lamellar grains, with equiaxed γ grains at the lamellar grain boundaries. This observation indicates an alpha-transus temperature of slightly above 1350°C. The amount of α_2 phase in the welding zone centre decreased to 60% (Figure 29 (c)). Far away from the weld centre, the amount of α_2 phase decreased rapidly and finally reached 25% in the base material. The microstructures of the welding zone, heat affected zone and base material regions of the heat-treated specimen are presented in Figure 30 (b). All three regions consisted of a near-lamellar structure. It can be seen from the figure that the lamellar-colony size in the welding zone was 6 μm, smaller than the size of 10 μm observed in the heat affected zone. However, compared with the as-welded specimen, the

heat-treated sample presented no pronounced microstructural differences among its different regions.

4.4 Tensile properties

The microstructure of a material plays a role in its mechanical properties. It has been reported that the lamellar structure is poor in ductility; however, it is superior to the near-γ structure in fracture toughness, fatigue resistance and high-temperature strength [73]. The stress-elongation-to-fracture curves at 750°C for both specimens #1 and #2 are presented in Figure 31. Each curve represents the average values from at least three tests. The samples from the as-welded specimen began to soften at approximately 3% plastic elongation. Then, the stress gradually decreased up through 25% elongation, after which the damage progressively increased until the material fractured. The ultimate tensile stress of the as-welded specimen was 355 MPa, and the elongation to fracture was 44%. The low ultimate tensile stress and high elongation to fracture are attributable to the γ phase in the base material, where the fracture occurred. The mechanism of the pronounced softening of fine-grained γ at 750 °C will be discussed in detail.

The samples of the specimen #2 subjected to heat treatment exhibited an improved ultimate tensile stress of 524 MPa, 50% higher than that of the as-welded specimen. The elongation still reached 21% with no stress-softening regime before the final fracture. The heat-treated specimen, which exhibited an almost fully lamellar structure, demonstrated a balance between higher tensile strength and acceptable elongation to fracture.

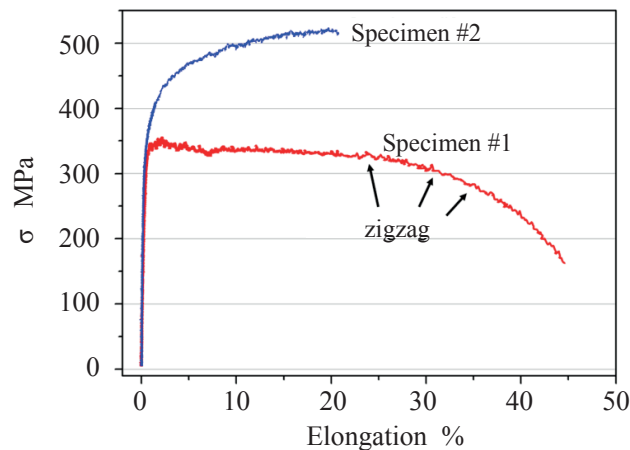Figure 31: Tensile stress vs. elongation for as-welded (#1) and heat-treated (#2) specimens. The weld lines were oriented normal to the loading direction. The tensile tests were conducted at 750°C.

4.5 Fracture analysis

The as-welded specimen #1 was investigated via radiography to detect welding defects such as macro-/micro-cracks and pores in the welding zone. Figure 32 (e) presents representative

radiograph of the as-welded specimen. It is apparent from Figure 32 (e) that the welding zone of this specimen was free of macrocracks and visible pores. Moreover, the weld seam was slightly thicker than the base material. The start and end of the weld seam were partially melted because of the energy concentration in the laser run-in and run-out regions. The tensile specimens were cut via EDM as indicated by the white line, with the weld seam oriented normal to the loading direction. The specimen geometry is shown in Figure 23.

The fracture surfaces are shown in Figure 32. To understand the microstructure at the fracture tip, the fractured tensile specimens were polished for SEM investigations of the microstructural regions of interest. These microstructural images are presented in Figure 33 and Figure 34, where the loading was oriented in the horizontal direction.

For the as-welded specimen, the fracturing occurred in the base material. It exhibited a ductile fracture mode, and dimples could be seen throughout the specimen (Figure 32 (a)). The striation provided further evidence of the ductile fracture behaviour. It is interesting to note that a few "microcracks" were observed with lengths of 10-20 μm, as indicated by arrows in Figure 32 (b). Such "microcracks" were frequently observed on the fracture surface of the specimen. The microstructure at a position 1 mm away from the fracture tip (Figure 33 (a)) exhibited many cavity stringers propagating parallel to the tensile direction. These stringers were of 5-10 μm in length. As demonstrated by Niu [89], such cavity stringers elongate and coalesce when the deformation strain is increased at the fracture tip. It can be inferred that the stringer length at the fracture tip should be longer than that observed in Figure 33 (a) because of the severe deformation. Under tensile deformation, these elongated and coalesced cavity stringers led to "microcracks", as observed in Figure 32 (b), and finally led to the fracture of the tensile specimen.

A detailed investigation revealed the formation of cavity stringers (Figure 33 (b)). The γ grains were refined in the deformed region to be less than 1 μm in size. The α_2 grains were elongated, separated and wrapped by γ colonies. Most of the α_2-phase grains were observed to lie along the γ-colony boundaries, and some of the small ones were located at triple boundaries of γ. When such cavities extend into one another, a coalescence zone forms between them. On the one hand, as reported by Nieh [66], GBS is the most commonly considered mechanism of deformation in fine-grained γ-TiAl intermetallics at high temperatures. During deformation, high local stresses develop at triple grain boundaries and lead to the debonding of γ colonies. The stress is reduced by GBS through stress-driven vacancy diffusion. On the other hand, bright α_2 particles were observed near the cavities. Compared to the hard and brittle α_2 phase, the soft nature of γ helps to activate deformation and relieve local stress, thereby delaying the formation of cavities. However, when γ grains encounter a coarse α_2 grain, the γ grains may reach their deformation limit and fail to sustain their relative positions. Strain misfit between the two phases will inevitably arise, leading to the development of a stress concentration and cavity formation [69].

It has been reported that DRx can occur in the high-temperature and low-strain-rate regime, as evidenced by grain refinement [67]. DRx leads to stress softening and local stress relief, which can also be identified from the zigzag behaviour observed in the tensile tests (Figure 31). Because this zigzag behaviour indicates an interaction between strain hardening and DRx softening, DRx in the γ grains also occurred during the tensile testing, and the stress concentration was partially reduced.

After heat treatment, the base material was transformed into a nearly lamellar microstructure. The fracture occurred in the welding zone, with cracking perpendicular to the tensile direction. As shown in Figure 32 (c)-(d), the fracture surfaces presented translamellar and interlamellar fracture modes, combined with cleavage fracture, as further confirmed by Figure 34 (a)-(b). In Figure 34 (c) and (d), three regions of interest are labelled. The first region reveals interlamellar microcracks with a number of intact ligaments located in the wake of the secondary crack and connecting the microcracks. This morphology was caused by decohesion of interlamellar slip, as has also been reported by Chan and Kim [74]. In the second region of interest, a microcrack occurred in the γ region, which was surrounded by two lamellar colonies. γ grains are considered to be softer than lamellae. The interfacial debonding of γ and lamellar grains is caused by stress concentration and strain misfit. The third interesting region displays a microcrack initiated and propagating within a single α_2 lamella. The α_2 phase is intrinsically brittle, and this delamination separation is also

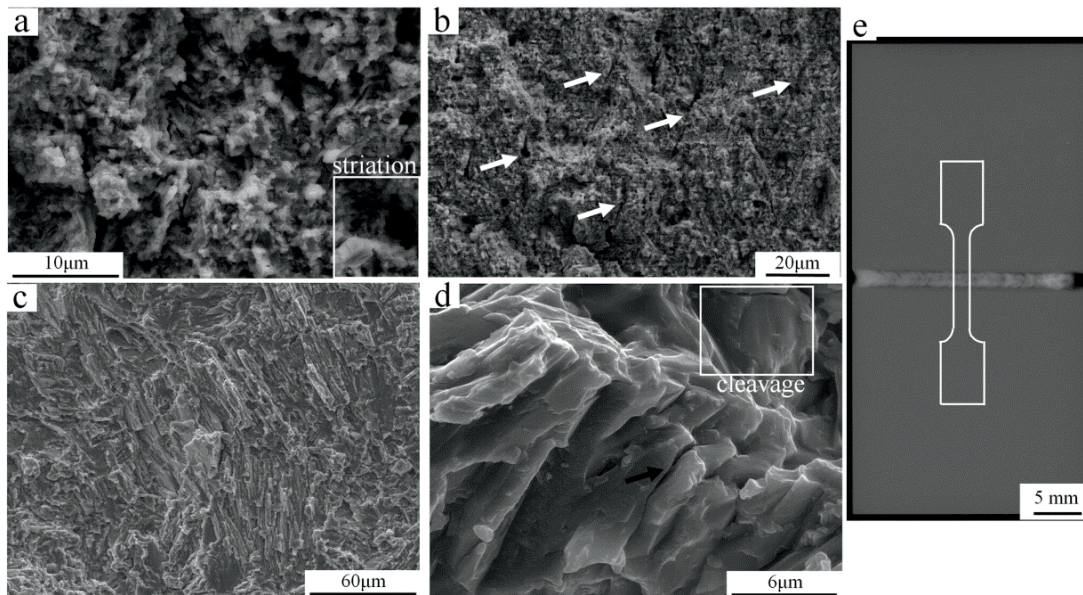Figure 32: Fracture surfaces of the specimens after tensile tests: (a), (b) as-welded specimen #1; (c), (d) heat-treated specimen #2; (a), (c) macroscopic views; (b), (d) microscopic views. (e) Radiograph of an as-welded specimen #1. The samples for the tensile tests were cut via EDM across the weld in the shape indicated by the white line, with the weld seam oriented normal to the loading direction.
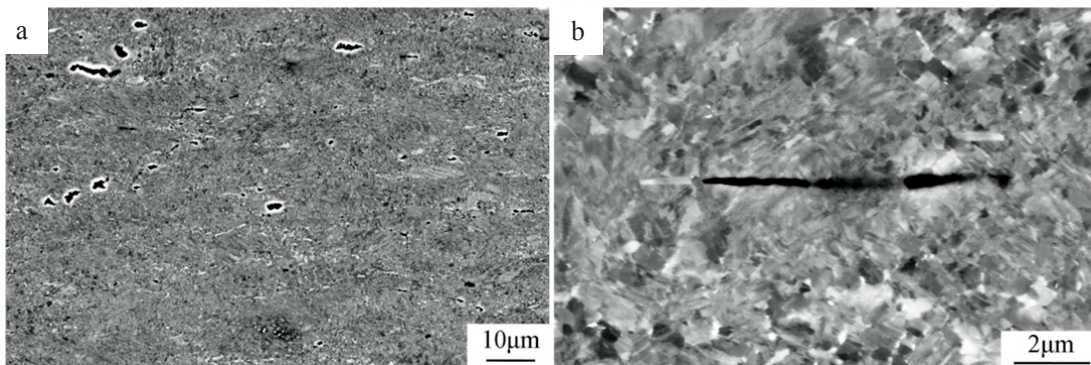
Figure 33: SEM observations in BSE mode of microstructures 1 mm away from the fracture tip in the as-welded specimen after tensile testing: (a) macroscopic view and (b) microscopic view. The tensile loading was applied in the horizontal direction.
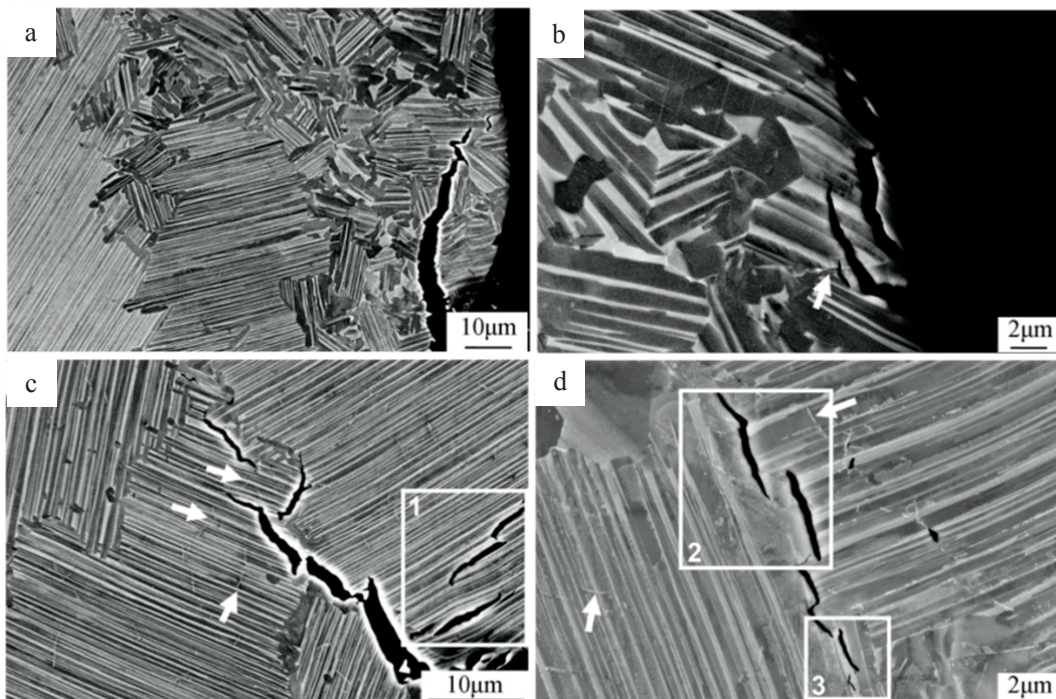
Figure 34: SEM observations in BSE mode of the microstructure of a heat-treated specimen after tensile testing at the fracture tip: (a) macroscopic view, (b) translammellar microcracking, (c) interlamellar microcracking, and (d) delamination separation through the α_2 phase and interlamellar debonding. The tensile loading was in the horizontal direction.

attributable to the local stress concentration. It can be concluded that local stress concentrations and strain misfit were responsible for the microcracking and ultimately led to crack coalescence and fracture.

Boride ribbons were observed in the vicinity of the microcracks, as indicated by arrows in Figure 34 (b)-(c). These borides of 5 μm in length remained at some distance from the crack. It seems that they neither were involved in crack initiation nor played a role in crack

propagation. Additionally, as indicated by the arrow in Figure 34 (b), a microcrack was observed to propagate across a boride. It can be inferred that boride may have a positive effect on the prevention of crack propagation. Investigations conducted by Hu [76, 77] have indicated that long, coarse titanium borides are responsible for debonding along boride-ribbon/matrix interfaces and lead to the premature failure of materials. Borides of over 100 μm in length are detrimental to tensile properties. However, when the boride dimension is carefully controlled to approximately 5 μm, as demonstrated in this study, borides do not appear to be detrimental but may instead be beneficial to tensile properties.

4.6 Diffraction morphology analysis

The morphology of the Debye-Scherrer rings is related to grain size and texture with respect to the beam size and the dimensions of the illuminated volume [90]. When a ring has been unrolled into a line and azimuthally integrated, a continuous and smooth line indicates a large number of small, non-textured grains. A spiky morphology reveals that the material consists of a few large grains, whereas a line with only a few coarse but regular spots indicates that the material is strongly textured.

The base material (Figure 35(a)) consisted of both α_2 and γ phases. A thin layer of fine-grained and texture-free copper paste was coated onto the plate. In the first view, the diffraction morphology of the α_2-002 line is seen to coincide with that of the γ-111 line along the azimuthal angle, indicating that the crystallographic planes of α_2-(002) and γ-(111) satisfied the Blackburn relationship. The rhombic diffractions of γ-002 and γ-200 align commutatively along a line. The azimuthal difference between neighbouring diffraction spots of γ-002/γ-200 is 180°. This finding indicates a strong cube texture of γ, with the c axis parallel to the longitudinal direction and the a axis parallel to the transversal direction. Such a cube texture is typical after a rolling process. The diffractions of both γ-002 and γ-200 indicate gradual rotations of correlated groups of grains and a large longitudinal lattice strain [90]. The appearance of commutative γ-002/γ-200 diffraction maxima also reflects the crystal symmetry of the γ grains. There is a 90° difference in orientation between the (002) and (200) γ planes in a tetragonal lattice. Although there was a limited amount of the α_2 phase in the base material, as indicated by the weak peak in the integrated diffraction signal, it was sufficient to determine the orientation relationship between α_2 and γ, i.e., most of the α_2-(201) plane was parallel to the γ-(200) plane, whereas a small amount of the α_2-(201) plane was parallel to the γ-(002) plane. This correlation between the α_2 and γ planes may have resulted from the rolling process.

The amount of the α_2 phase in the weld seam was clearly greater than that in the base material, as evidenced by the stronger α_2 peaks. A streak diffraction morphology is observed, and these streaks extend from the original line and link the neighbouring patterns. This streak, with the shape of a truncated rod, is the result of the formation of very fine lamellae,

consistent with the microstructure shown in Figure 27 (b). These fine lamellae gave rise to a peak-broadening effect in the diffraction signal. The γ-002 and γ-200 diffraction spots changed from commutative to synchronous. The appearance of synchronous diffraction originated from the lamellar transformation from the α field. Because the γ phase precipitated from α_2 following the Blackburn orientation relationship $(0001)_{\alpha 2}//\{111\}_\gamma$ during furnace cooling, two $\{111\}_\gamma$ planes could be parallel to each other with a misorientation of 120° between them. This misorientation would lead to parallel directions of $<\bar{1}01]//<1\bar{1}0]//<0\bar{1}1]$ in neighbouring planes. Thus, the synchronous nature of the γ-002 and γ-200 diffractions serves as proof of lamellar formation in the welding zone, which is consistent with the microstructural observations.

The copper paste was stress-free and fine-grained. The integrated diffraction of this copper layer appears as a continuous, straight diffraction line, which can be used as a reference. It is important to note that the diffractions of both the α_2 and γ phases are shifted along the azimuthal angle, as shown in Figure 35 (b) and (c). The diffraction lines of α_2-200, α_2-201, γ-002 and γ-200 exhibit smaller scattering vectors in the longitudinal direction and shift to higher scattering vectors in the transversal direction. This finding indicates large internal strains in both phases. According to Bragg's equation, an increased lattice distance d in the longitudinal direction leads to a decreased diffraction angle θ and a smaller scattering vector. The observed diffractions also correspond well with the high longitudinal residual stress in the welding zone region (Figure 29 (a)).

The diffraction morphology of the near-heat affected zone presented in Figure 35 (c) also exhibits streaks in all diffraction lines. However, the streak intensity is weaker than in Figure 35 (b). This reduced streak intensity is consistent with the observed massive-γ transformation in the microstructure. It is important to note that the size of the incident beam was 0.2 mm × 0.2 mm, much larger than the width of the near-heat affected zone. The illuminated region contained not only the near-heat affected zone but also a few lamellar grains in the welding zone or the far-heat affected zone. Therefore, streaks can be still observed in the diffraction lines.

The diffraction morphology of the base material after tensile testing indicates that the texture changed to a maxima/minima pattern (Figure 36 (a)). The α_2-002 and γ-111 diffractions exhibit spots of strong intensity in the transversal direction. Correspondingly, they tend to be weak in the longitudinal direction. This change in intensity with direction is stronger at the fracture tip (Figure 36 (c)), where the specimen was subjected to the highest deformation. This orientational change can be attributed to the rotation of grains under a vertical tensile load, as is further confirmed by the γ-002 and γ-200 diffraction lines. The a axis of the γ grains, which originally lay in the transversal direction, rotated towards the longitudinal

direction, which was perpendicular to the tensile load. The originally rhombic γ-002 also split into two components, indicating the rotation of the c axis of the γ phase.

Two significant differences can be observed by comparing the diffraction morphologies before and after tensile testing. On the one hand, the streak intensity for the specimen after tensile testing (Figure 36 (b)) is significantly stronger than that for the as-welded welding zone (Figure 35 (b)) because of the phase transformation from α_2 to γ. This phase transformation is confirmed by the diffraction intensities. The integrated areas under the γ-002 and γ-200 peaks are clearly higher than that under the α_2-201 peak after tensile testing (Figure 36 (b)); however, the reverse was true before (Figure 35 (b)). The precipitation of γ in the α_2 phase occurred because of the activation of atomic diffusion at a temperature of 700-850°C, when the welding zone was in a non-thermodynamic equilibrium state [86, 90]. Furthermore, the tensile testing increases the dislocation density, which also served to increase the diffusion coefficient. The γ precipitation refined the lamellar spacing, giving rise to a high streak intensity after tensile testing. Another difference between Figure 35 (b) and Figure 36 (b) lies in the azimuthally homogeneous spreads of the γ-002 and γ-200 diffraction signals. The change from a spiky morphology to a homogeneous one demonstrates that the grains were nucleated and the grain size was refined in the welding zone. Thus, it is reasonable to conclude that both the grain size and the lamellar spacing were refined in the welding zone as a result of the tensile testing.
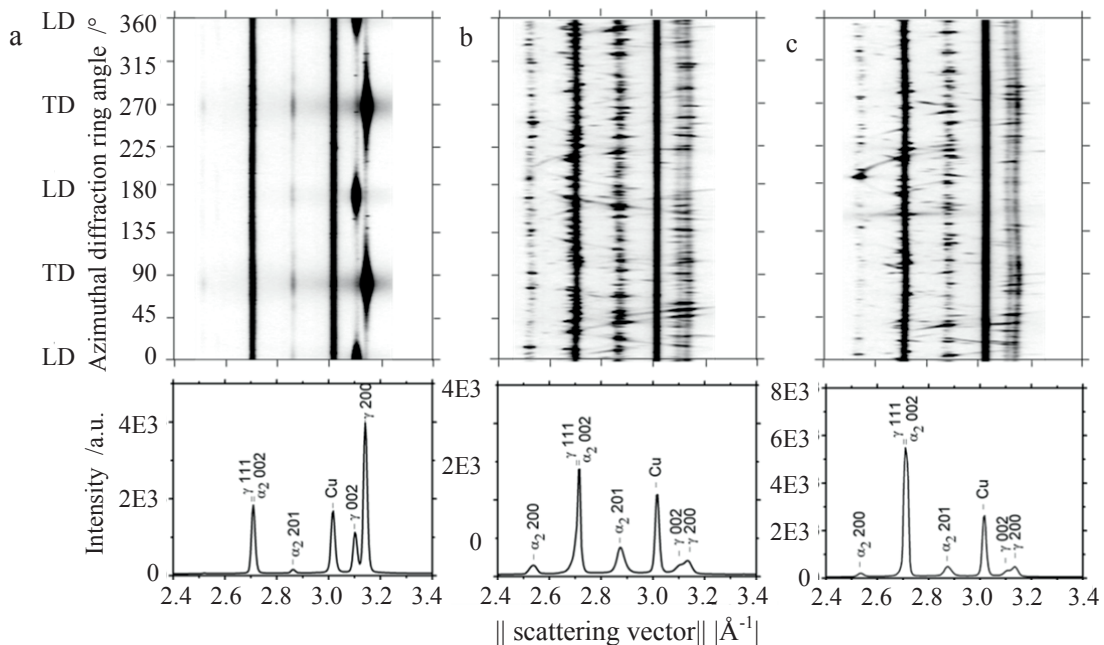
Figure 35: X-ray diffraction morphologies of the as-welded specimen: (a) base material, (b) welding zone, and (c) near-heat affected zone. The Debye-Scherrer diffraction rings have been unrolled into lines and azimuthally integrated. LD/TD denotes the longitudinal/transversal direction of the weld.
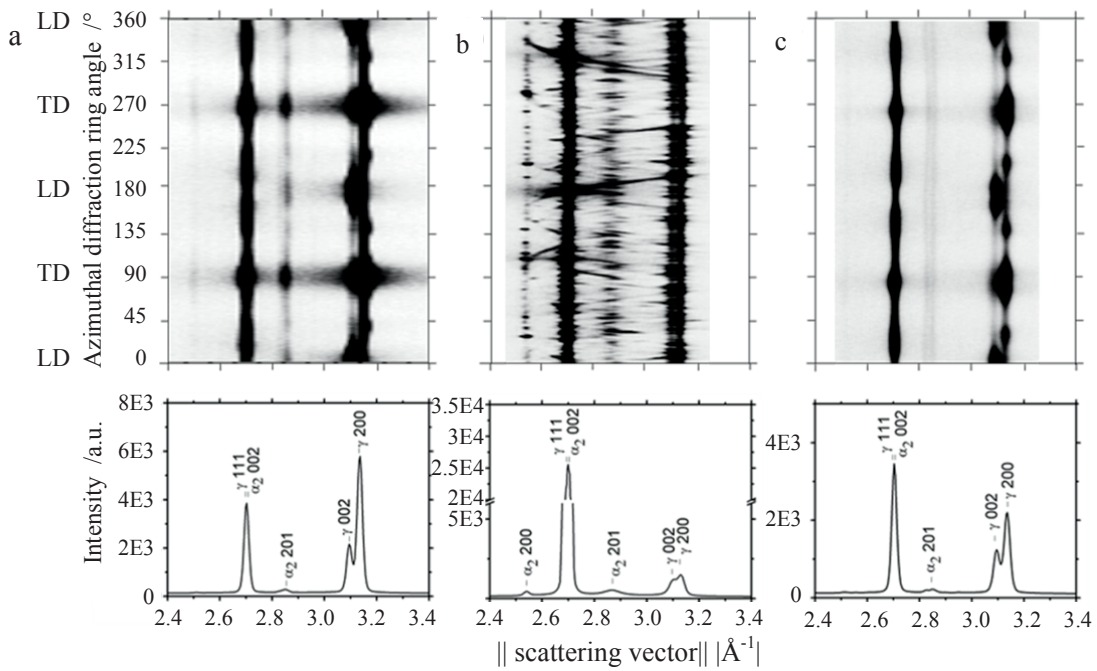
Figure 36: X-ray diffraction morphologies of the as-welded specimen after tensile testing at 750°C with an initial strain rate of 1.67×10^{-5} s^{-1}: (a) base material, (b) welding zone and (c) fracture tip (the specimen fractured at the base material). The diffraction morphologies were treated in the same manner as in Figure 35.
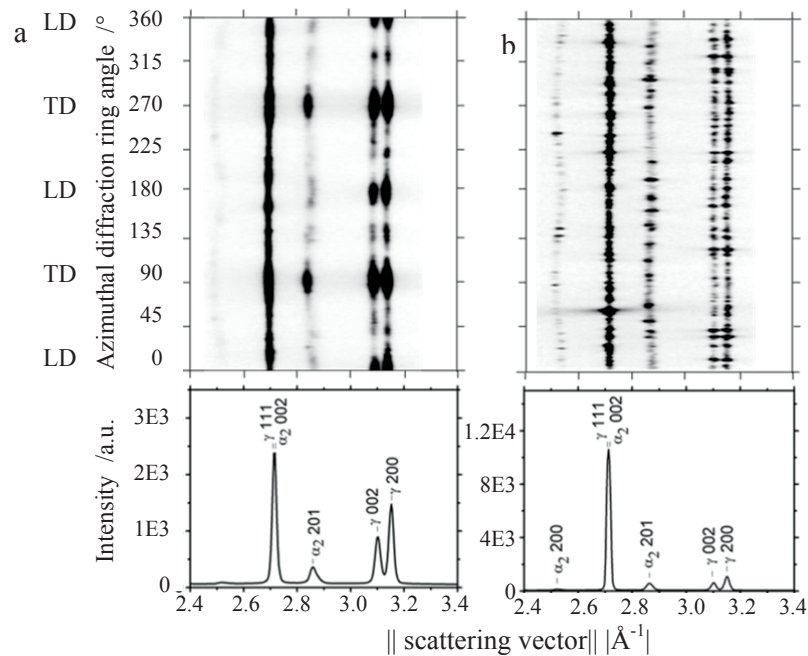
Figure 37: X-ray diffraction morphologies of the heat-treated specimen after tensile deformation at 750°C with an initial strain rate of 1.67×10^{-5} s^{-1}: (a) base material and (b) welding zone (the specimen fractured at the welding zone). The diffraction morphologies were treated in the same manner as in Figure 35.

47

Parallel diffraction lines of γ-002 and γ-200 are observed for the heat-treated specimen after tensile test in both the base material and the welding zone (Figure 37 (a)-(b)) because of the lamellar morphology in both regions. Again, the diffraction lines of α_2-201, γ-002 and γ-200 exhibit peak shifting along the azimuthal angle. The streak intensity was effectively reduced by the thick lamellar spacing. All this information obtained from the diffraction measurements corresponds well with the microstructural observations (Figure 27 (f)).

4.7 Conclusions

1. The crack-free joining of γ-TiAl-based alloys can be achieved through laser beam welding when the material is pre-heated in a furnace to 750°C. The welding zone is composed of coarse lamellar dendrites with small lamellar spacing. The residual stress presents a symmetrical three-peak morphology in the welding zone and heat affected zone because of the microstructural evolution and heat-induced softening. After heat treatment, the residual stress is largely relieved. The specimen exhibits a lamellar microstructure, which demonstrates a high ultimate tensile strength and acceptable elongation to fracture at 750°C.

2. Grain-boundary sliding accompanied by dynamic recrystallisation is considered to occur during the deformation of fine-grained γ-TiAl intermetallics at high temperatures. Strain misfit arises between the α_2 and γ phases and ultimately leads to the fracture of the tensile specimen.

3. In a material with a fully lamellar structure, fracturing is caused by translamellar and interlamellar separation. Cracking propagates through microcracks and delamination within α_2 lamellae. Titanium boride of small dimensions (<5 μm) is not found to cause premature fracturing of the tensile specimen.

4. The diffraction lines exhibit scattering-vector shifting along the azimuthal angle, which confirms the presence of high longitudinal tensile stress in the welding zone. Additionally, the application of a tensile load induces grain rotation, as indicated by diffraction shifting along the azimuthal angle. It is found that a phase transformation from α_2 to γ occurs in the welding zone during tensile testing at 750 °C because of the atomic diffusion facilitated by the high dislocation density in the non-equilibrium region. Both the grain size and the lamellar spacing in the welding zone are refined by tensile testing. After heat treatment, the welding zone exhibits a spiky diffraction morphology with a reduced streak intensity, which is consistent with the observation that the microstructure contains coarse grains with a wide lamellar spacing.

The disadvantage of heating by resistance furnace is that it is very time consuming. It takes 5 hours to carry out one welding experiment. The welding efficiency can be improved by heating using an induction furnace, which will be introduced in the next chapter.

5 Heating using an induction furnace

As seen in chapter 4, the crack-free welding of a TiAl alloy can be accomplished via furnace preheating at 750 °C. However, the heating using resistance furnace is quite time consuming. This chapter is dedicated to improve the heating efficiency via an induction furnace, which provides a fast and flexible heating. Moreover, these investigations were conducted using alloy 2 to assess the influence of *in situ* and conventional post-weld heat treatments on the microstructural and microtextural properties of the final weld. The content of this chapter is published in [21].

5.1 Experimental parameters

The alloy under investigation was alloy 2, the chemical composition of which is presented in Table 3. The actual composition was verified via EDS and was found to be within 1 at% of the nominal values. The welding was performed using the set-up depicted in Figure 16 in three steps: pre-heating, welding and post-weld heat treatment. All plates were pre-heated to 600 °C and maintained at that temperature for 1 minute to establish temperature homogeneity throughout the entire sample. The welding process was conducted using a laser beam power of 1200 W (identified as the power at the welding plate) at a rate of 1.5 m/min. *In situ* post-weld heat treatments at temperatures of 25 °C (sample #1), 400 °C (sample #2) and 800 °C (sample #3) and a duration of 1 minute were applied using an induction coil immediately after welding. After post-heating, the samples were air cooled. The welding time for a single specimen is about 15 minutes. A fourth specimen fabricated using the same procedure as sample #3 was conventionally heat treated at 1200 °C for 1 hour in a vacuum furnace and subjected to furnace cooling (sample #4).

The welds were visually inspected and investigated via radiography for the detection of cracks and porosity. The as-welded specimens were sectioned, ground and, finally, mechanically polished using a vibrating polisher. The microstructures were examined via SEM in BSE mode and EBSD. HEXRD experiments using synchrotron radiation were performed at DESY, Hamburg. Please refer to Chapter 4.1 for details of HEXRD experiment.

5.2 Radiography

Cracks transverse to the weld seam were observed in specimens #1 and #2 (Figure 38 (a)). When the specimens were subjected to *in situ* post-weld heat treatment at 800 °C, a sound square butt weld was produced. As shown in Figure 38 (b)-(d), the joint was free of pores and macrocracks, and both the top and bottom sides of the weld seam were bright silver in colour, indicating that the melt pool was not oxidised during the welding process. From the comparison of the results of various *in situ* post-weld heating temperatures (specimens #1 to #3), it is evident that *in situ* post-weld heating at sufficient high temperature followed by air

cooling plays an important role in mitigating solid-state cracking, which can be entirely eliminated when the specimen is post-heated at 800 °C. Although the high temperature gradient during cooling induces a significant amount of residual stress and suppresses the phase transformation resulting from laser beam welding, its impact can be reduced if the cooling is terminated at a temperature of approximately 800°C. When the welding zone is *in situ* post-heated above the brittle-to-ductile transition temperature, it undergoes phase transformation and plastic deformation, and its tendency towards cracking can be dramatically reduced [28]. However, when the *in situ* post-heating temperature is equal to or lower than 400 °C, cracking is observed in the material.

5.3 Microstructural characteristics

In alloy 2, with its β-stabilising alloying elements and low Al content, the β phase is the only phase that is present immediately after solidification is complete. This alloy is recognised as a β-solidifying alloy. Figure 39 (a) presents the microstructure of the base material stemming from the solidification path $L \rightarrow L + \beta \rightarrow \beta \rightarrow \beta + \alpha \rightarrow \beta + \alpha + \gamma \rightarrow B2 + \alpha_2 + \gamma$. The γ-TiAl appears as dark grey, the α_2-Ti_3Al appears as light grey, and B2 appears as the brightest phase. The B2 was found to be enriched in Cr, Si and Nb and depleted in Al; the composition determined via EDS was Ti-31.98Al-2.95Cr-1.2Nb-1.05Si. The B2 phase was predominantly located along colony boundaries and sometimes within the interiors of colonies. The B2 did not form a complete layer around the lamellar colonies but was
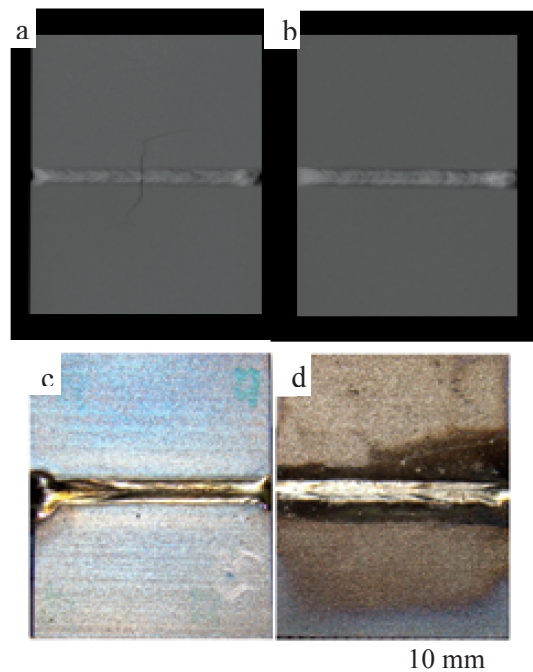

Figure 38: (a) Representative radiograph of specimen #1. (b) Radiograph of crack-free specimen #3. (c) Top and (d) bottom sides of specimen #3.

intersected by small γ grains. Most of the γ grains stemmed from γ lamellae in the colonies and grew into the β region. Cheng et al. [91] have observed that these coarsened γ grains have the same orientation as their thinner counterparts. Borides, indicated by arrows, in long straight ribbons and blocky morphologies, were observed to lie across colony boundaries. These borides have been reported to play an important role in grain refinement through the heterogeneous nucleation of α on borides [48, 51]. The volume fractions of the three phases in the base material were determined via EBSD to be 18.2%, 17.6% and 64.3% (in vol%) for B2, α_2 and γ, respectively. The equiaxed lamellar (γ + α_2) colonies had an average diameter of approximately 100 μm.

The welding zone (Figure 39 (b)) was composed of fine acicular α_2 plates distributed in various orientations, with average dimensions of approximately 8 μm in length and 2 μm in width. The fine acicular α_2 plates in the welding zone were observed to be separated by bright layers, which were enriched in Nb and Cr. The β dendrites transformed into α. The β stabiliser Nb was expelled into the α grain boundaries. Because of the high cooling rate from the melting point to 800 °C, chemical homogenisation could not be achieved, giving rise to these bright ridges [51]. Borides could not be easily identified under the microscope (Figure 39 (b)); only one, with a rod shape, was observed lying along the α_2 colony boundary (Figure 39 (c)). After welding, the volume fraction of the α_2 phase increased significantly to 92.1%, which was five times greater than that in the base material. Accordingly, the volume fractions of the B2 and γ phases decreased to 4.1% and 3.8%, respectively.

To reduce the amount of the brittle α_2 phase present in the welding zone, a conventional heat treatment with a duration of 1 hour at 1200°C was applied to specimen #4. The welding zone microstructure after this annealing (Figure 39 (d)) consisted of γ, B2 and lamellae. The amount of borides was observed to be greater than that in the as-welded welding zone, and they were observed to be present solely in γ grains or lamellae, or at the boundaries of γ and lamellae grains. The γ grains were observed to be intersected by B2, resulting from direct nucleation or discontinuous coarsening from B2 via B2 → γ [91]. The volume fractions of B2 and γ increased significantly after heating for 1 hour at 1200°C, and the phase composition changed to 10% B2, 53% α_2 and 37% γ.

5.4   Texture characteristics

The misorientation angles between α laths originating from the same β grain can only take values of 10.5°, 60°, 60.8° and 90°, as reported by Gey and Humbert [92]. Thus, the misorientation angle can be used to determine whether the α grains obey the Burgers relationship with respect to the parent β grains. According to the α_2-phase texture map of the base material (Figure 40 (a)), the material consisted of coarse equiaxed α_2 grains. The misorientation angles (Figure 40 (b)) indicate a slight preference for values in the range of 8-
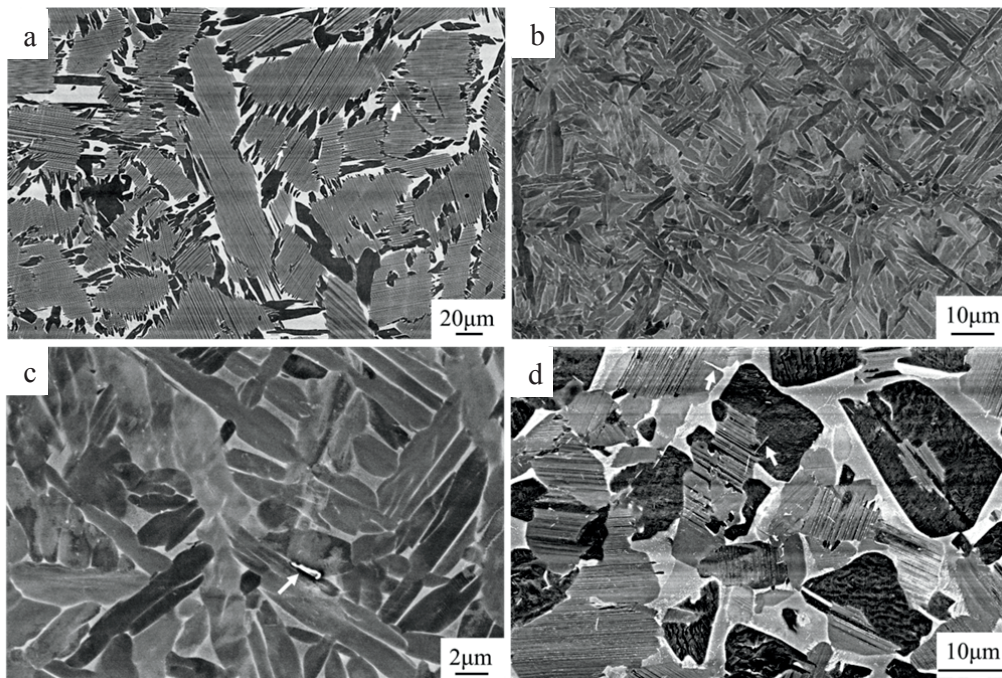
Figure 39: SEM images acquired in BSE mode of the microstructures of (a) the base material, the welding zone at (b) low and (c) high magnification and (d) the welding zone after annealing.
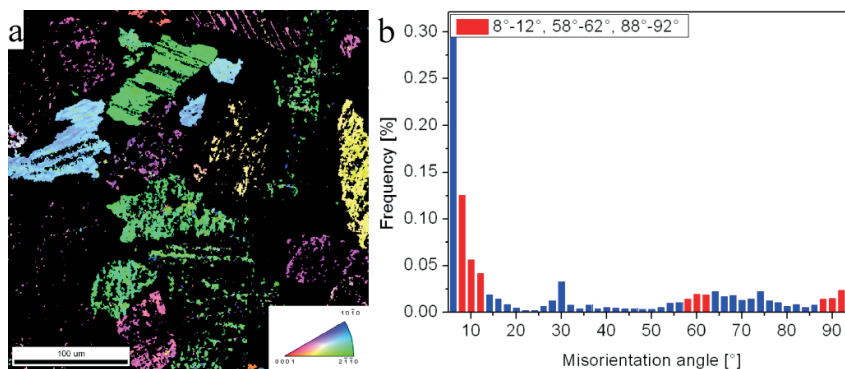
Figure 40: EBSD measurements of the Ti_3Al phase of the base material: (a) the texture map and (b) the misorientation angles between neighbouring Ti_3Al grains.

12°. This finding indicates that the presence of borides led to refinement in the base material during the solidification and that most of the α grains were non-Burgers.

The texture map of the $α_2$ phase in the welding zone (Figure 41 (a)) indicated that a large number of $α_2$ fine plates had the same orientation as neighbouring grains, as indicated by the large pink region near the top and middle part of the map. A similar result was also observed in Figure 6 (a) and (c) of ref. [48], although the author did not indicate that there were colonies of plates separated by bright ridges presenting the same orientation in the top, middle and bottom regions. As a result of this effect, the colony size in the welding zone
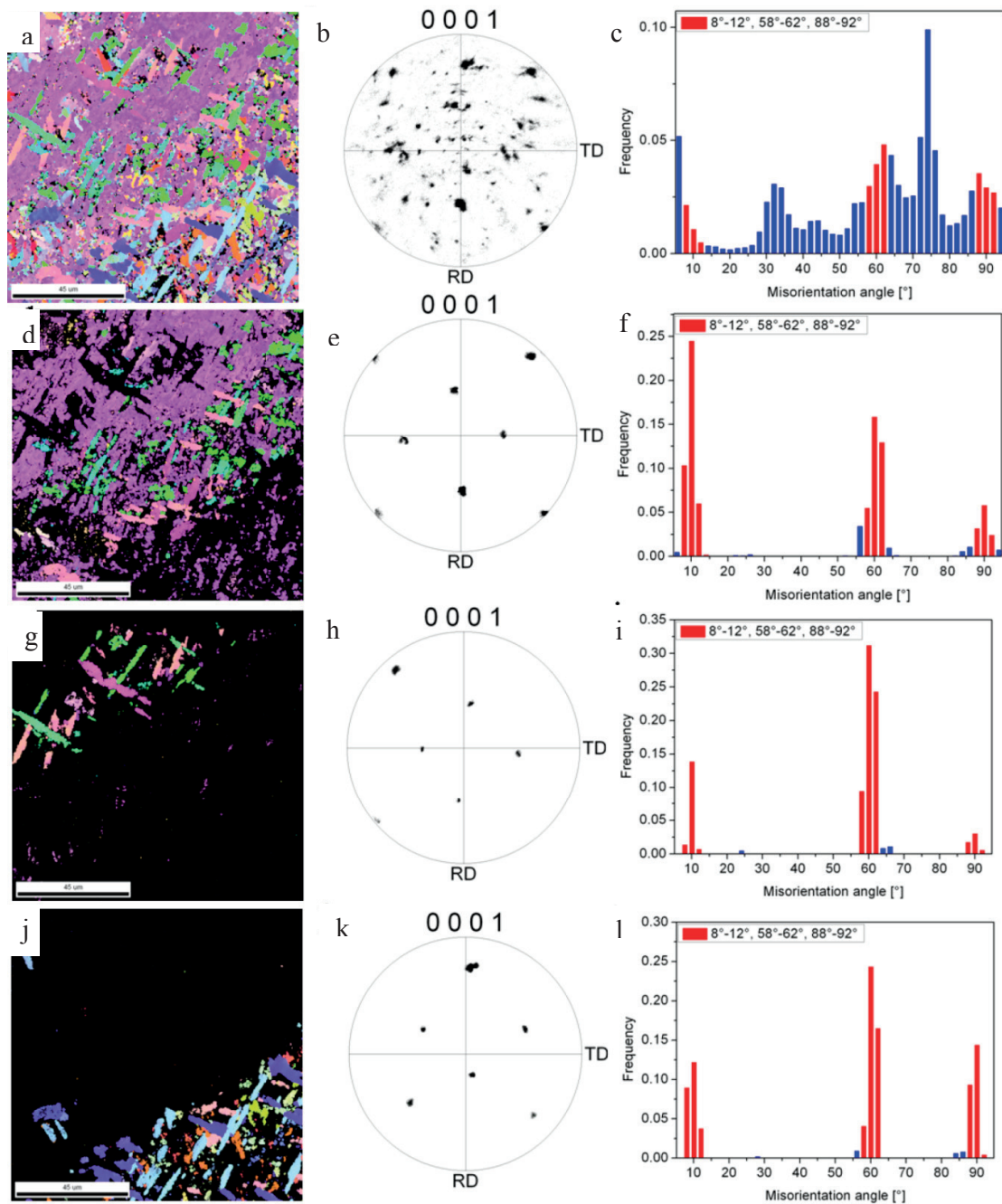
Figure 41: EBSD measurements of the Ti₃Al phase of the welding zone: (a) a texture map of all α_2 phase, (b) a pole figure of all α_2 phase (c) the misorientation angles between neighbouring grains; (d), (g) and (j) texture maps of three groups of α_2 grains; (e), (h) and (k) the corresponding pole figures of the three grain groups; and (f), (i) and (l) the misorientation angles between neighbouring α_2 grains of three grain groups.

cannot be simply identified by the dimensions of the α_2 plates; instead, it depends on the size of the "textured grain colonies". These coarsened "textured grain colonies" can suppress the refinement induced by the thin α_2 plates, as indicated by the microstructure. The pole figure

(Figure 41 (b)) indicates a rather random orientational distribution of the base plane of the α_2 phase, which resulted in a broad distribution of misorientation angles (Figure 41 (c)). Only a slight preference for angles of 8-12°, 58-62° and 88-92° can be observed. This broad distribution of misorientation angles can be attributed to the interaction of α_2 plates from the same parent β grain or α_2 grains adjacent to the β grain boundary. There are three possible nucleation mechanisms for the formation of this structure. Firstly, α grains nucleate heterogeneously on borides, through various orientation relationships: $(0001)_\alpha//(001)_{B27}$ and $<11\bar{2}0>_\alpha//[010]_{B27}$, as reported by Hu [51]; $[0\bar{1}1]_\alpha//[\bar{1}04]_{B27}$ and $[2\bar{1}\bar{1}0]_\alpha//[010]_{B27}$, as reported by Genç [53]; and $(1\bar{1}01)_\alpha//(001)_{B27}$, $(11\bar{2}0)_\alpha//(010)_{B27}$ and $(1\bar{1}0\bar{2})_\alpha//(100)_{B27}$, as reported by Banerjee [54]. As a result of the different orientations of different boride nucleation sites, a large number of α-grain orientations can be generated and spread into a broad distribution of misorientation angles. Secondly, α grains nucleate on β, and these grains follow the Burgers orientation relationship with their primary β grains. When α grains are generated from several overlapping β grains, the final misorientation angle depends primarily on the misorientation of the different parent β grains. Thirdly, borides nucleate on β through the relationship $\{011\}_\beta//(001)_{B27}$ and $<111>_\beta//[010]_{B27}$. At the same time, the α_2 phase heterogeneously nucleates on boride with an orientation relationship of $(0001)_\alpha//(001)_{B27}$ and $<11\bar{2}0>_\alpha//[010]_{B27}$, as observed by Hill et al. [52] and Hu et al. [25]. The nucleation of boride on the β phase and the nucleation of the α_2 phase on boride with the restrictions of the orientation relationships listed above can also lead to the formation of Burgers α_2. The interactions of several overlapping β dendrites can also give rise to a broad distribution of misorientation angles between α_2 grains. To verify the hypotheses detailed above, the original pole figure and texture map of the α_2 grains were divided into different components, as shown in Figure 41 (d) - (l). Interestingly, these individual pole figures, i.e. (e), (h) and (k), consist of points with misorientation angles of either 60° or 90°. In Figure 41 (e), the position of the {0001} poles of the grains in the mapped area actually correspond well to virtual {110} poles of a β grain aligned with the [100] crystal direction parallel to the TD. Figure 41 (h) and (k) exhibit the same coordination between $\{0001\}_\alpha$ and $\{110\}_\beta$, although the primary β is rotated somewhat. The misorientation angles of the α_2 grains in these three individual groups are presented in Figure 41 (f), (i) and (l). All these figures exhibit high intensities at angles of 8-12°, 58-62° and 88-92° for the three individual grain groups. This result proves that each individual group of α grains satisfies the Burgers orientation relationship in the welding zone.

The amount of α_2 phase was significantly reduced after the specimen was heat treated at 1200°C for 1 hour followed by furnace cooling (Figure 42). The α_2 laths reformed into an equiaxed morphology in the heat-treated welding zone. The misorientation-angle

distribution (Figure 42 (c)) exhibited peaks at angles of 8-12°, 58-62° and 88-92°, indicating that a small number of the equiaxed α_2 grains originated from the same primary β. Only two groups of Burgers α grains were identified in the texture map (Figure 42 (d)-(i)); approximately 35% of the α grains were textured. Unlike the coarsened "textured grain colonies" of the as-welded welding zone (Figure 41 (d)), the α_2 phase formed independent grains with individual orientations. The reduced amount and size of the textured grain colonies in the welding zone following heat treatment led to the conclusion that the size of the textured colonies had indeed been refined.

EBSD measurements provide textural information; however, this information is restricted by the limited surface region that can be measured to statistically represent the entire specimen. To examine the grain distribution over a large volume, HEXRD experiments were performed in transmission mode on the same material sample that was used for EBSD
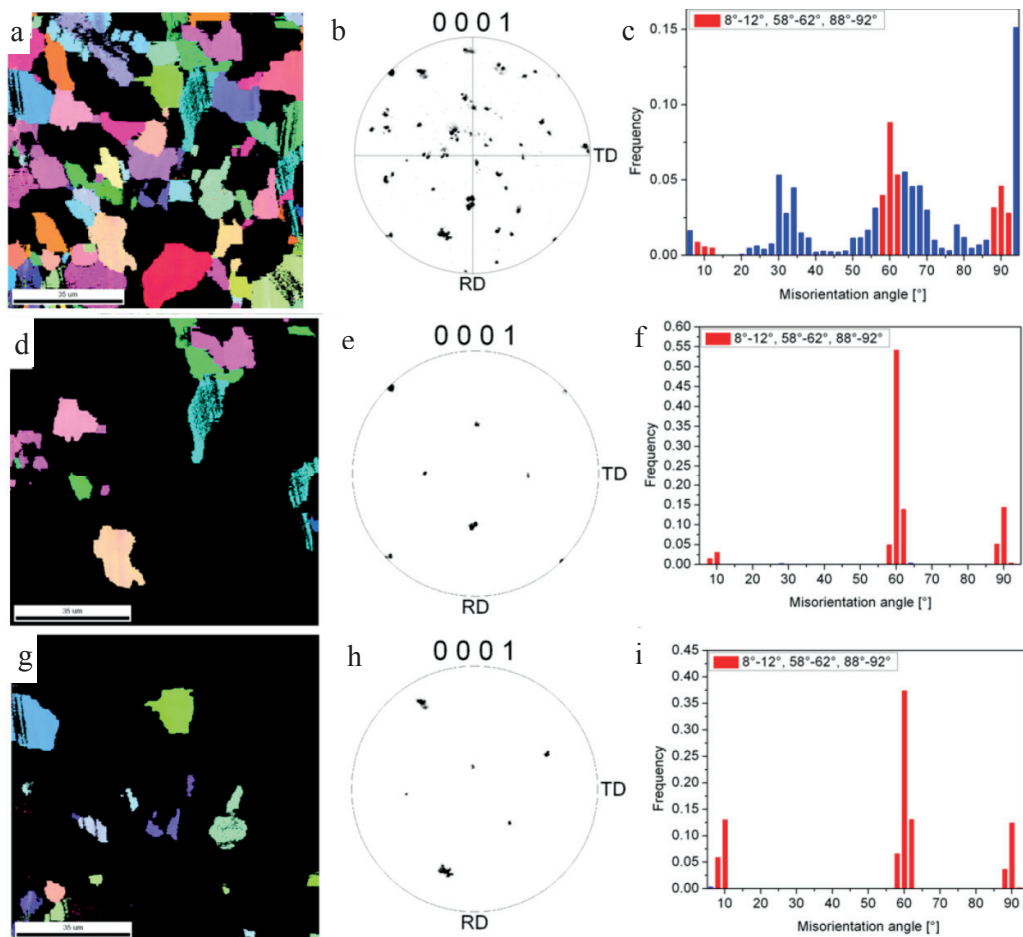
Figure 42: EBSD measurements of the α_2 phase of the annealed welding zone: (a) a texture map of all α_2 phases; (b) a pole figure of all α_2 phases; (c) the misorientation angles between neighbouring grains; (d) and (g) texture maps of two groups of α_2 grains; (e) and (h) the corresponding pole figures of the two grain groups; and (f) and (i) the misorientation angles between neighbouring α_2 grains of the two grain groups.
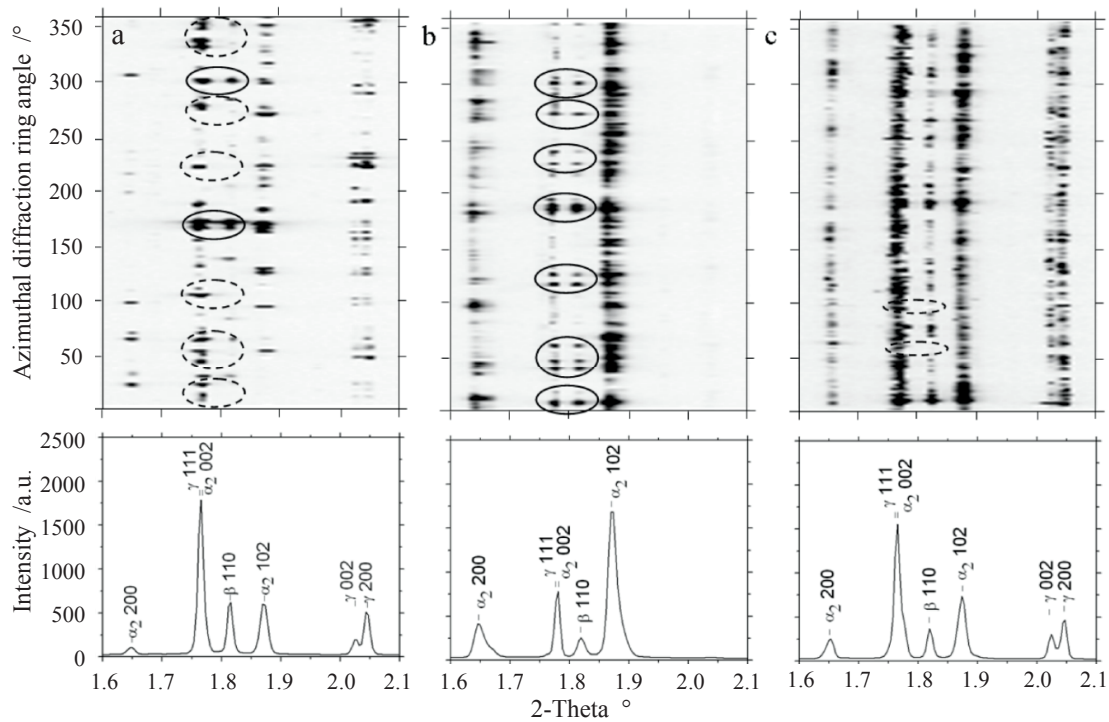
Figure 43: X-ray diffraction patterns of the (a) base material, (b) welding zone, and (c) annealed welding zone. The Debye-Scherrer diffraction rings have been unrolled into lines and azimuthally integrated. The solid and dashed ellipses indicate reflection pairs that correspond and do not correspond to the Burgers orientation relationship, respectively.

analysis. The beam was precisely oriented to measure the welding zone and the base material separately. The measurement volume of the incident beam was 1 mm × 1 mm × 2.7 mm. The Debye-Scherrer diffraction rings were recorded using a PerkinElmer detector. The diffraction rings were unrolled into lines, and powder diffractograms were calculated by azimuthally integrating the patterns over 360°. The wavelength of the incident beam was 0.14235 Å. As shown in Figure 43 (a) and (b), the $(110)_\beta$ and $(002)_{\alpha2}$ signals appeared as several single points rather than continuous lines, indicating that the base material and welding zone materials consisted of coarse grains or coarse grain colonies, which was consistent with the previous results. Comparatively speaking, the continuous diffraction lines of $(110)_\beta$ and $(002)_{\alpha2}$ in Figure 43 (c) demonstrate the refinement of the grain colonies in the annealed welding zone. The diffraction twins demarcated by the solid ellipses indicate that the (110) direction of β was parallel to the base plane of α_2. Nearly perfect parallel twins of β and α_2 are evident in Figure 43 (b). However, the $(110)_\beta$ and $(002)_{\alpha2}$ signals are not so well matched in the base material, indicating that the prevailing α nucleated heterogeneously through borides, whereas some α grains nucleated at the grain boundaries of the primary β grains.

Thus it can be understood that even though the grains were refined by α nucleation on boride in the cast specimens, this refinement could be hampered by the subsequent heat treatment.

The α_2 and β grains presented a Burgers orientation relationship after laser beam welding followed by air cooling (Figure 43 (b)). At the same time, the β grains tended to grow in more than one direction in the melt pool of the welding zone, which was not limited by the $<100>_\beta$//heat-flow direction. The textured grain colonies in the welding zone were refined after heating to 1200°C followed by furnace cooling. This heat treatment broke down the original microstructure, and the structure was rebuilt during cooling. It can be concluded that the heterogeneous nucleation of α on boride played an important role during furnace cooling, because the α_2 diffraction line displays a signal even where the diffraction line of β is blank (dashed ellipses in Figure 43 (c)) and fewer Burgers α grains are found in the annealed welding zone.

5.5 Conclusions

This study investigated the influence of post weld heat treatment applied using an induction furnace on the cracking behaviour and microstructure/microtexture of a TiAl-based alloy. The following conclusions can be drawn:

1. *In situ* post-weld heat treatment has a positive effect on reducing cracking in the welding zone of the TiAl-based alloy that is produced through laser beam welding. Cracking can be eliminated by applying *in situ* post-weld heating at 800 °C for 1 minute. *In situ* post-weld heating at lower temperatures is not sufficient to produce crack-free welds.

2. A large amount of the α_2 phase is formed because of the high cooling gradient that arises during laser beam welding. The welding zone consists of very coarse "textured α_2 colonies" with a sharp texture. EBSD and HEXRD analysis demonstrated that these "textured α_2 grain colonies" satisfy a Burgers orientation relationship with the parent β grains for laser beam welding followed by air cooling to 800 °C. The grain-refinement induced by boride is suppressed by these coarse textured colonies at a high cooling rate. The nucleation mechanism of the Burgers α_2 remains unknown.

3. Upon conventional post-weld annealing at 1200 °C for one hour, the original welding zone α_2 grains are broken down, and the structure is rebuilt during furnace cooling. The grains are thereby refined, and the heterogeneous nucleation of α on boride plays an important role in grain refinement at low cooling rates.

The welding efficiency is highly increased by heating via an induction furnace. The time for welding a specimen is reduced from 5 hours to 15 minutes. However, one shortcoming of the induction furnace is that the clamping jig needs to be made of ceramic restricting the complex design. One possible solution is to apply heating by a defocused laser as a heat source to heat the specimen locally, which will be discussed in the next chapter.

6   Dual-laser-beam heating and welding

As *in situ* post heating by an induction furnace can improve the weldability of γ-TiAl-based material and its mechanical properties, as introduced by chapter 5. However, the ceramic clamping jig is restricted by the complex design. This chapter describes a method of applying local temperature control and improving welding efficiency by applying heat treatments using a defocused laser beam to directly heat the area of interest. This approach reduces the conventional resistance furnace welding time of 5 hours to approximately 10 minutes. The work presented in this chapter is published in [9].

6.1   Experimental parameters

The material used in the investigation was TNB-V5. The experimental set-up was introduced in Figure 17. The welding approach that was used in this study consisted of three steps: pre-heating, welding, and *in situ* post-heating (process #2, Figure 44). For comparison, a simplified process without post-heating was also tested (process #1). The *in situ* post-weld heat treatment with a defocused laser beam was performed immediately following the welding process, while the welding zone temperature was still high. The pre-heating parameters were determined based on a pre-heating test. In this test, a thermocouple was inserted into the weld plate to measure the temperature generated by the defocused laser alone. At the end of the pre-heating process, the temperature of the weld seam could reach 800°C. Moreover, the diameter of the defocused laser was progressively reduced to reduce the temperature gradient across the welded piece. The total welding time was approximately 10 minutes.

Three samples were investigated. Samples 1 and 2 were prepared using processes #1 and #2, respectively. Sample 3 was heat treated in a furnace after the execution of process #2 at 1260 °C for 2 hours. This temperature is below the α transformation temperature of this material, which has been experimentally determined to be 1295 °C by Chladil et al. [93].

The microstructures of the laser-beam-welded TNB joints were investigated using SEM in BSE mode. The residual stresses in the butt-joint samples were measured. The welded pieces were cut via EDM into flat micro-tensile specimens for tensile testing. The tensile tests were conducted at 750°C with a tensile speed of 0.01 mm/min. At least three tests were performed for each sample condition, and the average values are reported. Before tensile testing, the specimens were ground with 2500# SiC paper to remove microcracks on the surface.
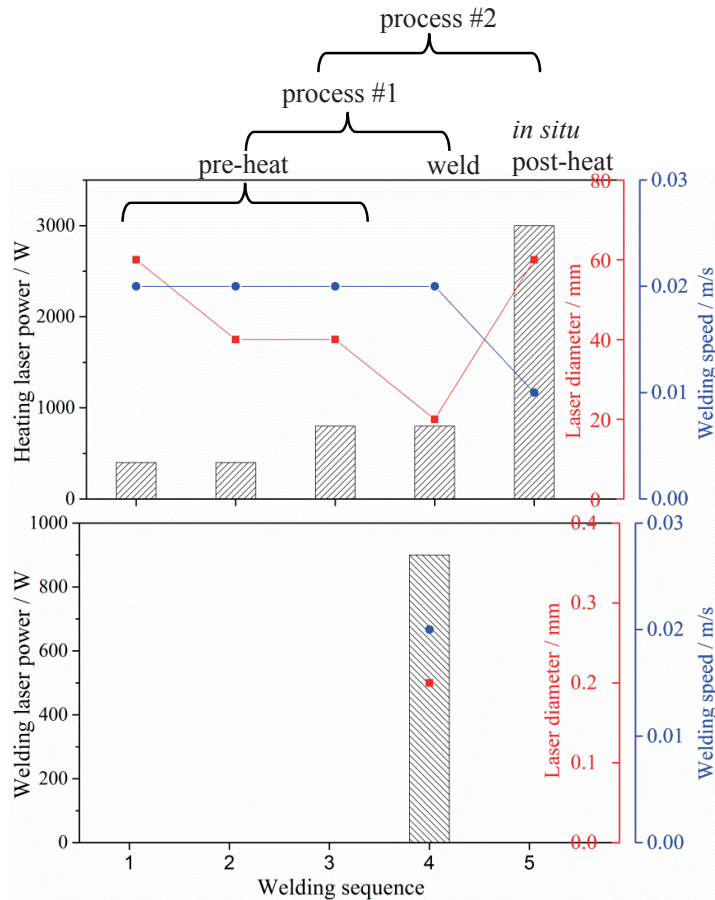
Figure 44: Dual-laser-beam welding parameters. Sequence 1-3: preheating with defocused laser. Sequence 4: welding and heating. The defocused laser is 2 mm behind the welding laser. Sequence 5: in situ post heating. The bars shows the energy input, the red dots indicating the laser diameter and the blue dots demonstrate the welding speed.

6.2 Microstructural characteristics

The base material was characterised by a duplex microstructure consisting of γ grains arranged in a strip-like fashion and lamellae (Figure 45 (a)). HEXRD experiment was made for base material, as shown in Figure 46, it consisted of γ-TiAl and α_2-Ti$_3$Al phases. A Cu paste was applied to the surface to calibrate the distance between the sample and the detector. The average grain size in the base material was 3.5 μm. Small amounts of carbides and borides below 1% may have been present but are not apparent in the diffraction pattern.

It is known that at high cooling rates, the high-temperature α phase cannot decompose; instead, it becomes ordered into the α_2 phase [32]. The α_2 phase in the welding zone (Figure 45 (b)) solidified into differently oriented plates. Only a small amount of the γ phase was observed in the welding zone, as γ formation is a diffusion-dependent process [32]. The bright layers, which were predominantly observed along colony boundaries, were identified
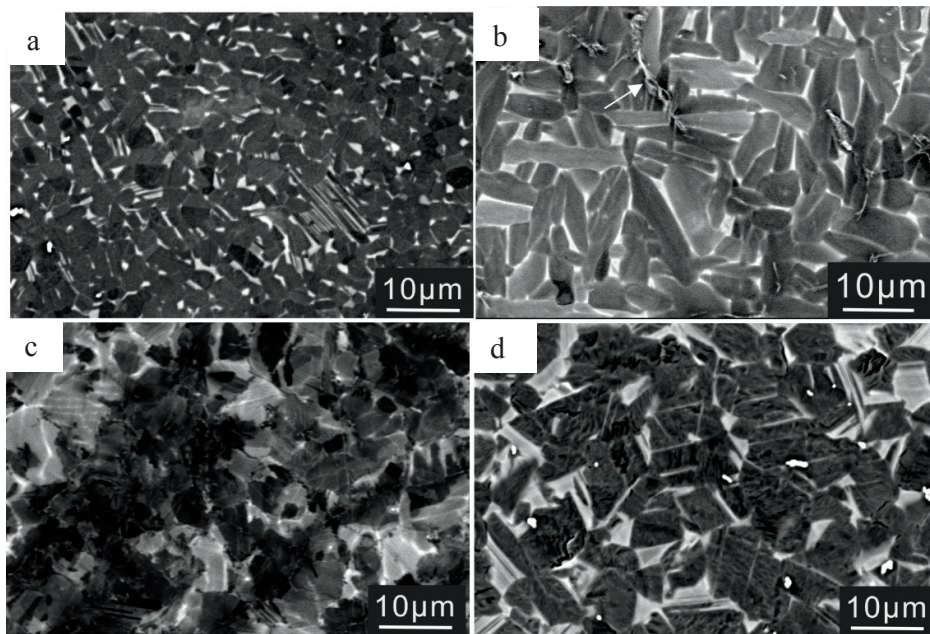
Figure 45: Back-scattering electron images of the microstructures of welded samples of TNB: The γ phase appears dark, and the $\alpha_2 + \gamma$ lamellae appear grey. (a) base material and the welding zones of (b) sample 1, (c) sample 2, and (d) sample 3.
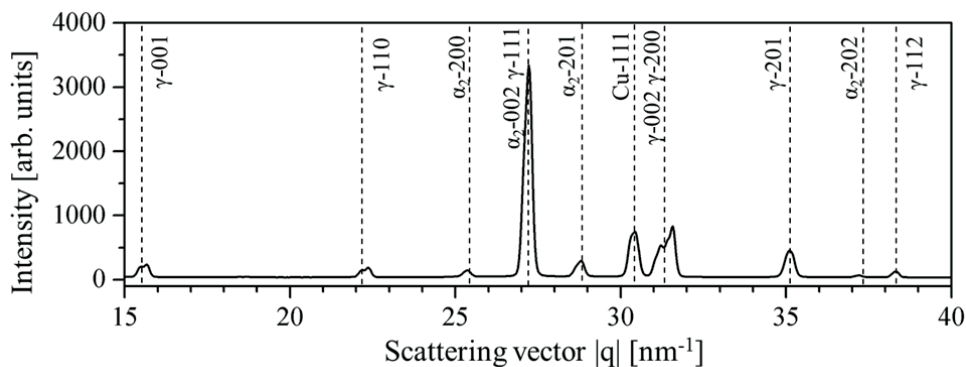
Figure 46: X-ray diffraction patterns (azimuthally averaged scattering intensity versus scattering vector |q|) of the base material.

through EDS analysis as layers enriched with Nb. The chemical composition of these layers was 53.1% Ti, 40% Al and 6.9% Nb. As we know from alloy 2, which is a β-solidifying alloy, these layers are formed via segregation during the $\beta \rightarrow \alpha$ transformation because of the low diffusibility of Nb. The arrow in Figure 45 (b) indicates an elongated boride particle of approximately 20 μm in length in the welding zone. This boride is very coarse, and such a particle may act as a critical defect in combination with other borides. This could have a detrimental effect on the mechanical properties of the material [76].

Upon *in situ* post-weld heating, the high-temperature α phase was decomposed, as shown in Figure 45 (c). The welding zone of sample 2 was composed of a massive γ phase, which was heavily faulted and developed from the high-temperature α phase when the welding zone

cooling rate was relatively high but not as high as that in sample 1 [32]. When sample 2 was conventionally heat treated within the (α+γ)-phase field, a microstructure that consisted of γ and α phases, with differently oriented α plates in a γ matrix, was generated. This microstructure is known as a convoluted microstructure (Figure 45 (d)) [28, 94]. Its formation is caused by the movement of Shockley partials and α precipitates on all four {111} planes of the massive γ phase.

6.3 Residual stress measurement

The stress patterns indicated high tensile stresses with a double peak in both samples, with maximum values at ±1.4 mm from the weld centre (Figure 47). The stress decreased rapidly with distance, eventually transforming into compressive stress. The maximum stress value of sample 1 was 1010 MPa, close to the yield limit. After *in situ* post-weld heat treatment, the maximum stress was reduced to 460 MPa (sample 2). After conventional heat treatment (sample 3), the stresses were completely relieved.

The observed double peak in the tensile stresses in the welding zone and heat affected zone resulted from softening, which also occurs in aluminium and titanium alloys. This shape of the stress curve can be explained in terms of the "mismatched bars" model developed by K. Masubuchi [18], which is introduced in chapter 2.3.1. Moreover, during welding, carbide precipitates such as Ti_3AlC and Ti_2AlC, which form arrays of strong pinning obstacles to dislocation, begin to dissolve, and the strengthening mechanism changes from carbon precipitation to carbon solution strengthening [95]. The carbon remains in solid solution in the welding zone and remains as precipitates in the heat affected zone and the base material,
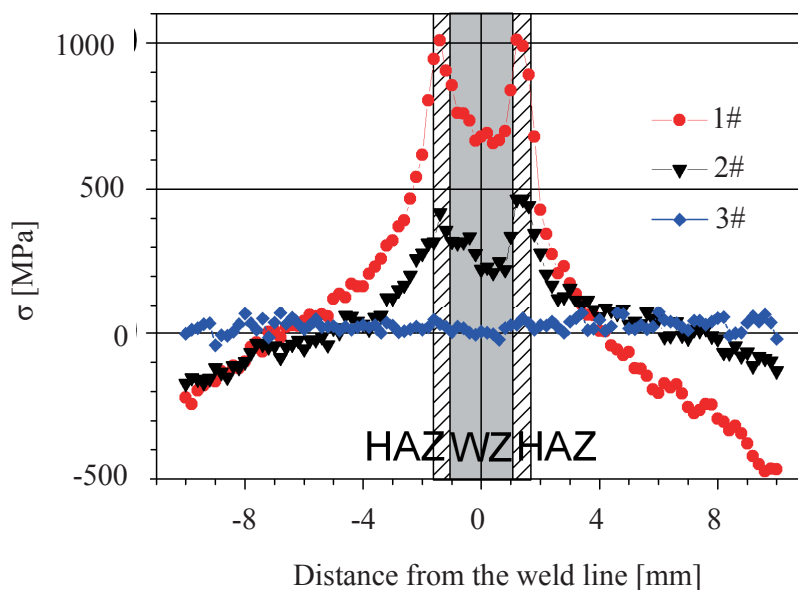

Figure 47: The longitudinal residual stresses of samples 1, 2, and 3, as determined via X-ray diffraction. The typical error is 30–50 MPa.

leading to the observed difference in the yield stress. Finally, in sample 1, the residual stress was 650 MPa in the welding zone and 1010 MPa in the heat affected zone.

The residual stresses experimentally determined in this work are in good agreement with the results of tensile tests conducted by Gerling et al. for the Ti-45Al-5Nb-0.5C alloy [96]. At room temperature, the yield stress was found to be 1080 MPa for Ti-45Al-5Nb-0.5C, which is similar to the residual stress in the heat affected zone of sample 1. However, it has also been proven that compared with carbon precipitates, carbon atoms in the solid-solution state act as weak glide obstacles that can be easily overcome with the aid of thermal activation. The flow stress has also been found to be nearly independent of the carbon concentration upon the addition of solid solute carbon [97]. This is why the residual stress of the welding zone was found to be approximately 370 MPa lower than that in the heat affected zone.

Sample 2 exhibited a peak residual stress of 460 MPa, 550 MPa lower than that of sample 1 (Figure 47). This finding indicates that residual-stress relaxation caused by dislocation motion was promoted by the *in situ* post-weld heat treatment. The residual stress observed for sample 3 indicates that the stress was completely relieved as a result of the conventional heat treatment.

6.4 Phase composition

As the phase composition is essential to the quality of the final welded piece, the phase distribution across the welding plate was determined (Figure 48). The contents of both phases were calculated using the Rietveld method. The figure shows that the phase composition of the base material was consistent in each sample, with 6–7% α_2 and 93–94% γ in the extruded state.

The phase composition of the welding zone varied strongly among the samples. In sample 1, an α_2 content of 90% formed a strong peak at the centre of the fusion zone, which was balanced by a 10% γ-phase content. In the region of the heat affected zone, the α_2 composition varied linearly until it reached that of the base material.
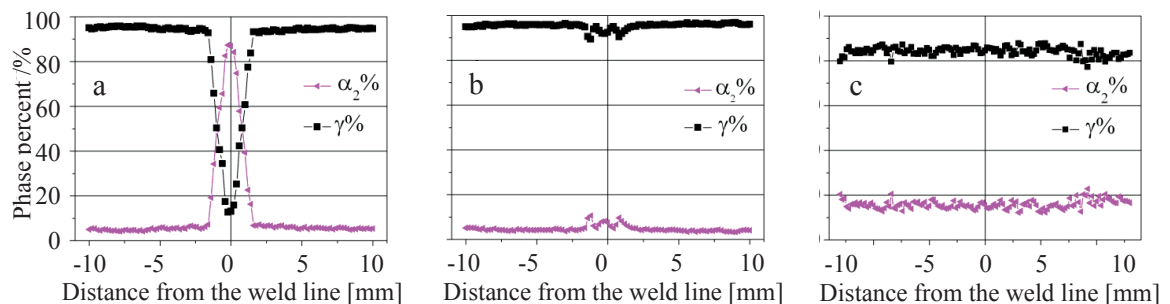

Figure 48: Phase percentages (volume percentages) of γ and α_2 across the welding zones of samples (a) 1, (b) 2, and (c) 3 as determined from the diffraction patterns.

In sample 2, the weld centre was composed of 93–94% massive γ phase, in agreement with the SEM observations. The γ-phase content decreased slightly at positions of ±1.2 mm from the weld centre (Figure 48 (b)). This decrease may be attributable to the higher cooling rate in the heat affected zone compared with that at the weld centre as a result of better heat conduction relative to the comparatively cold base material.

After the conventional post-weld heat treatment in the α + γ region, α precipitated within the γ, causing the amount of α_2 to increase once again. The phase composition and chemical composition of sample 3 were constant across the welding zone, indicating that the chosen temperature and duration for the conventional heat treatment were sufficient.

6.5   Mechanical properties

The influence of the microstructure on the weldability and mechanical properties of γ-TiAl-based materials has been reported [11, 28, 98]. The presence of the brittle α_2 phase is detrimental to the welded metal because this phase has a limited ability to accommodate plastic deformation. The results of tensile tests of the samples subjected to different heat treatments are presented in Table 4. These results demonstrate that the mechanical properties of the welds, represented by the UTS and elongation to fracture at 750°C, were significantly improved after either *in situ* or conventional heat treatment. Moreover, sample 3 exhibited a balance between a favourable UTS and favourable elongation because of its convoluted microstructure and reduced α_2 volume fraction. The tensile-test results are in agreement with those of Wu and Saage [28, 98], who have demonstrated tensile elongation of up to 1.3% and 1.1% in Ti-48Al-2Cr-2Nb and Ti-46Al-8Ta, respectively, both of which exhibit convoluted microstructures. In addition, it is worth noting the failure positions of the tensile specimens. The specimens taken from sample 3 fractured at the base material, whereas samples 1 and 2 failed at the welding zone and the heat affected zone, respectively; these results indicate that the convoluted microstructure formed as a result of *in situ* and conventional post-weld heat treatments improves the ductility and mechanical properties of TiAl-based alloys.

Table 4: Tensile-test results for the micro-tensile samples.

Sample number	UTS (MPa)	Elongation to fracture (%)
1	503	0.67
2	564	0.75
3	540	1.33

6.6 Conclusions

In conclusion, dual-laser-beam welding in combination with *in situ* and conventional heat treatments was performed in an effort to produce crack-free welding of a γ-TiAl-based alloy. The results can be summarised as follows:

1. Butt welding of TNB specimens of 2 mm in thickness and a size of 25×40 mm^2 was successfully performed using dual-laser-beam welding in a process consisting of pre-heating, welding and *in situ* or conventional post-weld heat treatment. No cracking was observed in the specimens. The entire welding time was approximately 5 minutes, which is considerably reduced compared with the time required for furnace heating.

2. *In situ* post-weld heat treatment is essential for the laser beam welding of γ-TiAl-based alloys for two reasons. First, this heat treatment, which is performed by heating the sample using a defocused laser immediately after welding, offers the advantages of decreasing the temperature gradient, relaxing the residual stress field and improving the dislocation motion. Second, a welding zone composed of massive γ exhibits a higher elongation to fracture than a welding zone that is predominantly composed of α_2. The improvement in ductility plays an important role in improving the fracture resistance of the as-welded piece such that cracking in the welding seams can be avoided.

3. By a subsequent conventional post-weld heating to the $(\alpha + \gamma)$-phase region for two hours the microstructure can be further improved. Such a treatment is sufficient to produce a convoluted microstructure, optimise the phase composition in the welding zone and ultimately increase the elongation by 77% at the expense of a 4% reduction in strength, thereby optimising the mechanical properties of the weld.

Last but not least, it is important to mention that the laser heating parameters depend strongly on the specimen geometry. If the specimen becomes bigger, it is necessary to increase the laser power or modify the laser path to heat the specimen homogeneously. This brings a question of how to precisely control the temperature regardless of the specimen size. This solution will be demonstrated in the next chapter.

7 *In situ* welding experiment FLEXILAS

As evidenced in chapter 4-6, the effective temperature control is critical of improving the reliability and efficiency of the TiAl welds. The dual-laser-beam is possible to heat locally; however, preliminary effort must be put to figure out the laser parameters which vary with the specimen geometry. In the FLEXILAS experiment, the temperature is controlled by a programed electrical system and a water cooling system, which are able to heat the specimen homogeneously and cool fast. With an assistance of a fibre laser, a reliable weld is made in 15 minutes.

The second advantage of the FLEXILAS facility is that it is possible to gain an understanding of the phase transformation during welding. Because the heating rate is extremely rapid, which requires only a few microseconds to melt the material, it is very difficult to measure this phase transformation using conventional methods. Based on the phase transformation knowledge of TNB-V5 alloy gained in chapter 6, this chapter concentrates on the influence of the laser parameters and the phase transformations during the laser melting and subsequent solidification of γ-TiAl alloys as observed via *in situ* HEXRD and a fast detector. Moreover, the knowledge gained from this investigation of the phase transformation is applied to the optimisation of the laser beam welding parameters. The content of this chapter is published in [99].

7.1 Experimental parameters

The TNB-V5 alloy was investigated and the experimental set-up was described in chapter 3.2.4. The specimen was heated at 150°C/s to 900°C by 4 programed resistance heating elements. Two local melts of constant energy input were performed after the specimen was heated, using a laser power of 600 W for 0.9 s and a laser power 300 W for 1.8 s. The second melt was performed after the specimen had cooled to 900 °C at a new position on the same specimen. Simultaneously, the detector was operated in a fast mode with a frame rate of 10 Hz to capture the phase transformation during melting and solidification.

After the *in situ* phase-transformation observation, nine welds were performed exactly with each parameter. For each weld one micro-tensile specimen was cut via EDM using the same geometry described in Figure 23 and the welding zone was in the middle of the gauge. The specimens were tensile tested at 25 °C, 650 °C and 750 °C with an initial strain rate of 1.67×10^{-5} s^{-1}. The samples were tested at each temperature. The average UTS and elongation to fracture of the specimens were analysed. Micro-hardness was also performed across the base material and welding zone. For each indent with the Vickers indenter load of 1 kp with a hold time of 20 s was used.

The knowledge of spot welding was transferred to line welding. Four bead-on-plate welds were performed at a constant linear energy. The welding parameters are summarised in

Table 5. Three micro-tensile samples were cut and tested as described above and the mechanical properties are evaluated.

Table 5: Welding parameters for the bead-on-plate welding.

Parameter name	1	2	3	4
Laser power (W)	300	600	1200	2400
Feed rate (mm/s)	2.5	5	10	20

7.2 Microstructural characteristics

Figure 49 (a) shows the initial microstructure of the extruded material. The material is the same as in chapter 6, it is duplex microstructure consisted of a strip-like arrangement of equiaxed γ, a few α_2 grains and elongated $\alpha_2+\gamma$ lamellar colonies, which were alternately aligned in the extrusion direction. The insert image shows the lamellar region, which was composed of fine α_2 and γ lamellae. Small amounts of borides are also observed parallel to the extrusion direction, as indicated by the arrows, exhibiting both blocky and flake morphologies [25, 100]. The columnar features in the welding zone (Figure 49 (b)) were initially α grains, which transformed into finely spaced $\alpha_2 + \gamma$ lamellae during cooling. For further details please refer to chapter 6.2 about the description of Figure 45. It is important to mention that the inset shows borides with a ribbon morphology concentrated in the dark lines, indicating that the borides formed before or simultaneously with the β grains and that they were expelled into the remaining liquid [48]. Thus, the boundaries of the β grains could be identified based on the borides and dark patches.
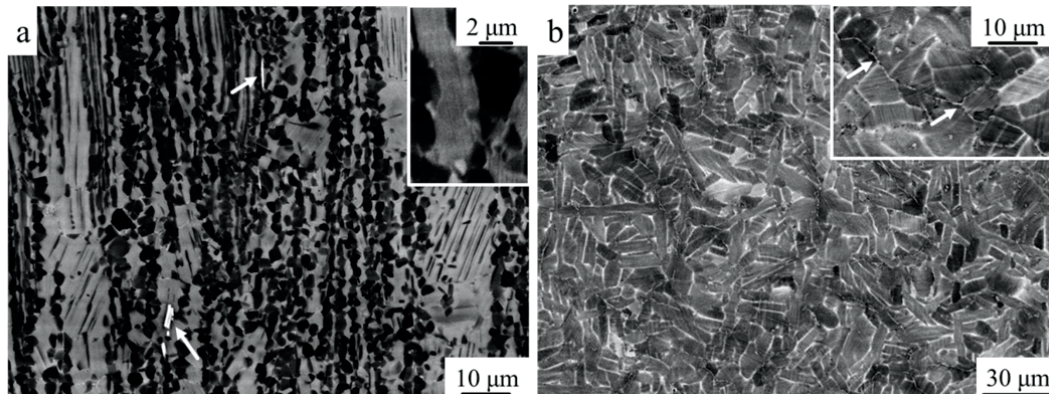

Figure 49: (a) Microstructure of the extruded rod (the extrusion direction is vertical). The arrows indicate borides parallel to the extrusion direction. The inset shows the details of the lamellae. (b) Microstructure of the melt zone after solidification, after laser melting of 300 W for 1.8 s. The arrows indicate the borides.

7.3 *In situ* phase transformation and grain refinement

During the local melting, the detector captured 10 images per second continuously during the experiment. The diffractions were analysed and arrayed into an image illustrating the

phase transformations over time (Figure 50). The scale of the figure represents the diffraction intensity, and purple and red colours correspond to low and high intensities, respectively. The transformation can be divided into 5 stages. The material began in a solid state (stage 1). Once the laser was switched on, the material melted into a liquid within an ultra-short time frame (stage 2). The diffractions from the solid phase vanished abruptly; meanwhile, a strong peak broadening was observed as a result of the formation of the liquid. In the 3rd stage, a completely stable liquid phase formed because of the continuous energy input from the laser. The diffraction from the liquid exhibited a strong intensity at a scattering vector of 27 nm^{-1}. Once the laser was switched off, the peak intensity of the melt gradually faded away. In the 4th stage, the transformation L $\rightarrow$ β occurred in the melt. From the diffraction of the high-temperature β phase, it was clear that the intensity of the $(110)_\beta$ peak (scattering vector 27.3 nm^{-1}) was much stronger than that of the $(200)_\beta$ peak (scattering vector 38.9 nm^{-1}). Afterwards, the solid underwent the following transformations as it cooled to 900°C (stage 5): β $\rightarrow$ β + α $\rightarrow$ α_2 + β $\rightarrow$ α_2 + γ + β.
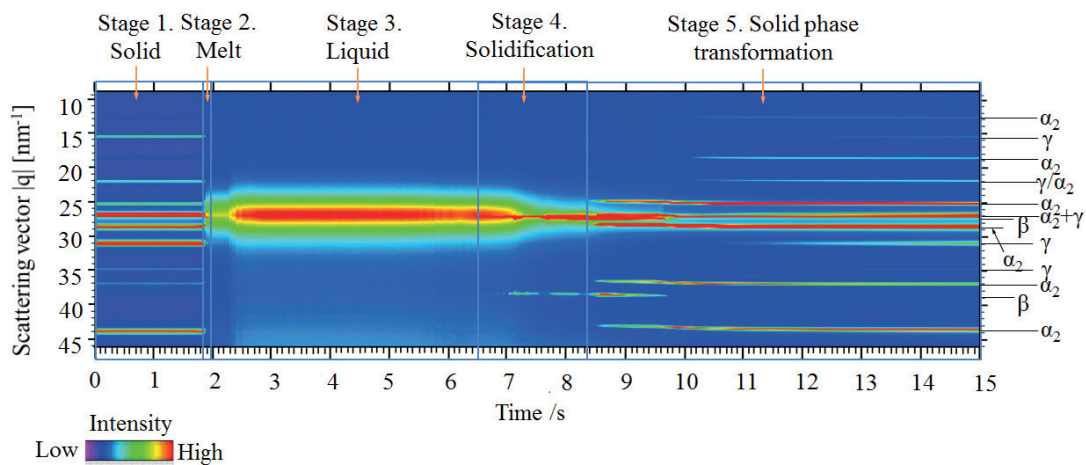

Figure 50: An example of time-resolved X-ray diffraction signals observed during the melting and solidification of TNB-V5 material.

7.3.1 Welding with 600 W laser power

As the melting stage (stage 2) was very short, Figure 51 separately presents X-ray diffraction patterns acquired only during laser melting at a laser power of 600 W for detailed analysis. The extruded starting material consisted of both α_2 and γ phases (Figure 51 (a)). The diffraction pattern indicates only small deviations from a powder texture. A calculation of the phase fractions using the Rietveld method yields a composition of 24 vol% α_2 phase and 76 vol% γ phase. After 0.1 s (Figure 51 (b)), the solid material began to melt and enter a liquid phase, typically observed as a halo beneath the diffraction reflections in the scattering range between 20 and 33 nm^{-1}. Another 0.1 s later (Figure 51 (c)), the α_2 and γ reflections decreased tremendously. Moreover, they shifted towards lower scattering vectors because of thermal lattice expansion, and the initially overlapping α_2-002 and γ-111 peaks split into two.

After 0.3 s had elapsed in the melting stage (Figure 51 (d)), the diffractions from α_2 vanished completely, leaving only three weak γ reflections. The intensity scales in Figure 51 (d)-(f) have been adjusted to show these small peaks. The amount of solid γ phase continued to decrease from 0.3 s to 0.9 s, as indicated by the three γ diffraction lines γ-001, γ-111 and γ-200. Finally, only a small amount of solid γ phase still remained after 0.9 s in the melting stage.

Under thermodynamic equilibrium conditions, the transformation from solid to liquid can be described as follows: $\alpha_2 + \gamma \rightarrow \alpha + \gamma \rightarrow \alpha \rightarrow \alpha + \beta \rightarrow \beta \rightarrow \beta + L \rightarrow L$. However, the diffraction patterns acquired during rapid laser melting show no evidence of the β phase prior to melting, and traces of the solid α_2 and γ phases can be definitively identified, as illustrated in Figure 51. This result indicates that the material melted rapidly when heated by the laser. A liquid film quickly formed on the surface, and the liquid-solid interface then rapidly propagated into the bulk material and ultimately formed a keyhole, where the majority of the laser energy was absorbed and where all the material melted to form a liquid. It is well known that the solid–solid phase transformation is a diffusional process, requiring both sufficient duration and temperature. However, the time from the initiation of melting to complete liquid formation was so short that solid–solid phase transformations were strongly inhibited. Thus, the solid retained its original composition of α_2 and γ phases and simply disintegrated into the liquid.

The diffraction patterns presented in Figure 51 also illustrate the melting sequence of phases in the bulk material. The figure indicates that the α_2 solids disappeared much earlier than the γ solids, leaving a few γ grains swimming in the melt pool until the material had completely melted. From a closer examination of the microstructure (Figure 49 (a)), it is apparent that the α_2 and γ phases exhibited different morphologies in the extruded material. The α_2 phase consisted predominantly of lamellae because of the decomposition of $\alpha \rightarrow \alpha_2 + \gamma$. The γ phase comprised either lamellae or globular grains alternately aligned with lamellae. It is well known that in multi-phase alloys, phase boundaries and interfaces are alternative sites for heterogeneous melt nucleation [101-103]. It is reasonable to deduce that the interfaces of the α_2 and γ lamellae were the initial venue for melt nucleation, consuming both α_2 and γ lamellae and forming liquid membranes at the lamellar interfaces. In the second stage, all lamellae melted, including all α_2 solids, leaving a few remaining superheated γ grains swimming in the melt pool. When such a system is heated extremely rapidly, it is theoretically predicted that it should be possible to increase the melting temperature by a factor of 1.3 to 2.0 [104, 105], leading to the coexistence of solid and melt above the melting temperature. Notably, the extruded material consisted of 24 vol% α_2 phase and 76 vol% γ phase. The higher volume fraction of γ may have been another reason for the apparently longer survival of solid γ particles in the melt compared to α_2.
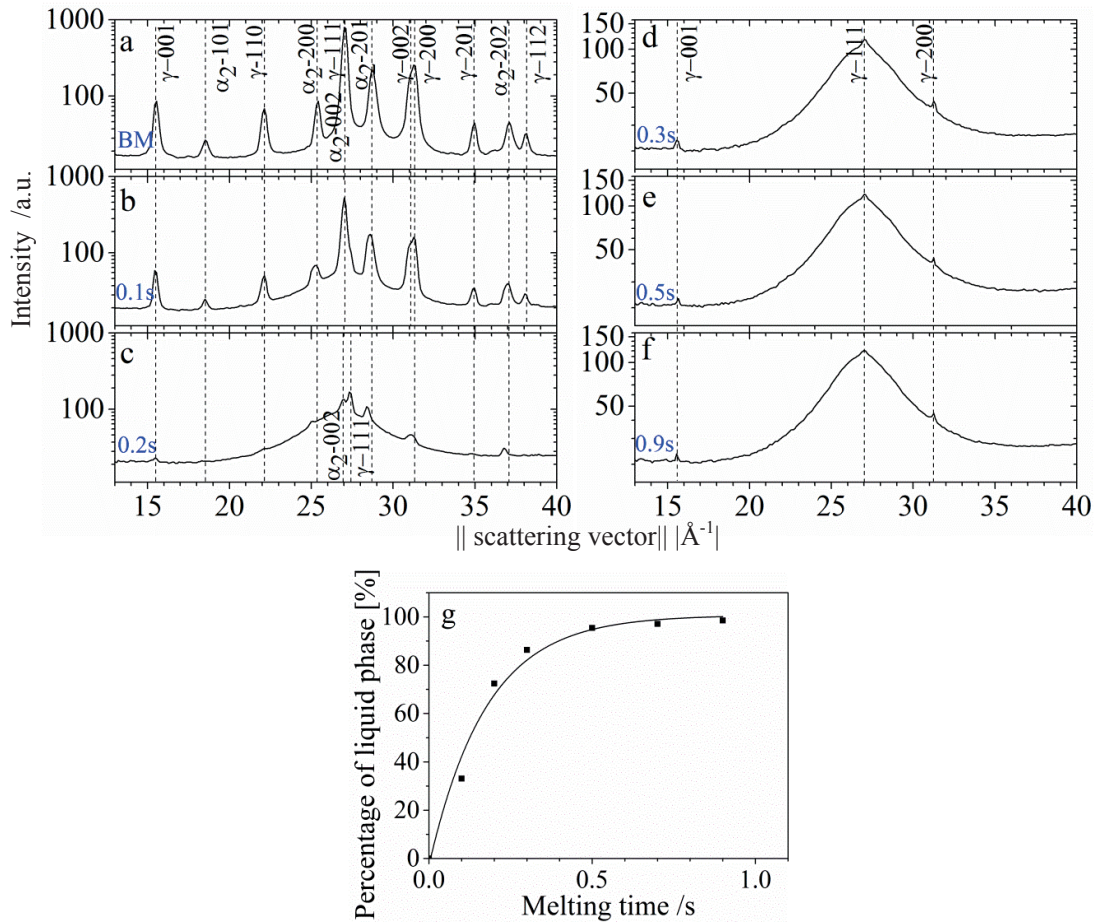
Figure 51: (a-f) X-ray diffraction patterns (azimuthally averaged scattering intensity versus scattering vector |q|) acquired during the laser melting of TNB-V5, revealing the phase compositions (a) of the base material and (b-f) at various times after the initiation of the laser melting process: (b) 0.1 s, (c) 0.2 s, (d) 0.3 s, (e) 0.5 s, and (f) 0.9 s. (g) Volume fraction of the liquid phase during laser melting. Laser power: 600 W.

To estimate the evolution of the amount of liquid over time, the background signals of Figure 51 (a-f) between the scattering vectors of 20 and 33 nm^{-1} were fitted with Gaussian functions. The areas under the Gaussian curves were integrated and compared to estimate the relative amounts of liquid phase present during the melting stage. Figure 51 (g) indicates a rapid melting of 86.3 vol% of the bulk material within only 0.3 s, followed by a much slower melting of the remaining 12.2 vol% of solid crystals over the next 0.6 s, leaving only 1.5 vol% of γ swimming in the melt. The presence of this superheated γ is consistent with the theoretical predictions reported in [104, 105].

7.3.2 Welding with 300 W laser power

After complete solidification, a lower laser power of 300 W was used to induce a second melt of the same sample at a new location. Compared with the previous melt, the second melt proceeded with a slower temperature increase. As illustrated by the diffraction patterns

(Figure 52), the solid-phase transformation underwent the following sequence: $\alpha_2 + \gamma \rightarrow (\alpha_2 + \alpha + \gamma + \beta) \rightarrow \alpha + \beta \rightarrow \beta \rightarrow \beta + L \rightarrow L$. The observation of α and β phases provides clear evidence that the diffusion-dependent solid–solid phase transformations $\alpha_2 + \gamma \rightarrow \alpha$ and $\alpha \rightarrow \beta$ took place in the heated area; these transformations did not occur in the previous welding experiment at a higher laser power. In addition, the diffraction peaks of the α_2, γ and α phases overlapped because of their lattice parameters. Figure 52 (c) appears to be composed of $\alpha_2 + \alpha + \gamma + \beta$ because of an overlapping of four phase fields, namely, $\alpha_2 + \gamma$, $\alpha + \gamma$, α and $\alpha + \beta$. The coexistence of both high-temperature and low-temperature phases can be attributed to the experimental set-up. After 0.4 s of melting, the heated area (demarcated by dotted lines in Figure 19 (b)) was relatively small, and the phase transformation occurred only within a small area. The X-rays swept over both the transformed and non-transformed areas, allowing both the low-temperature phase field $\alpha_2 + \gamma$ and the high-temperature phase field $\alpha + \beta$ to be observed. As the heating proceeded, the heated area expanded until it completely engulfed the area probed by the X-ray beam. Eventually, all grains had been transformed into α and β and no superheated grains are observed. Because of the appearance of α and β, it can be concluded that at a low laser power density, a slow heating rate, and long heating times, sufficient diffusion can take place for the expected solid–solid phase transformations to occur before the material melts. There was no superheated grains in the melt.
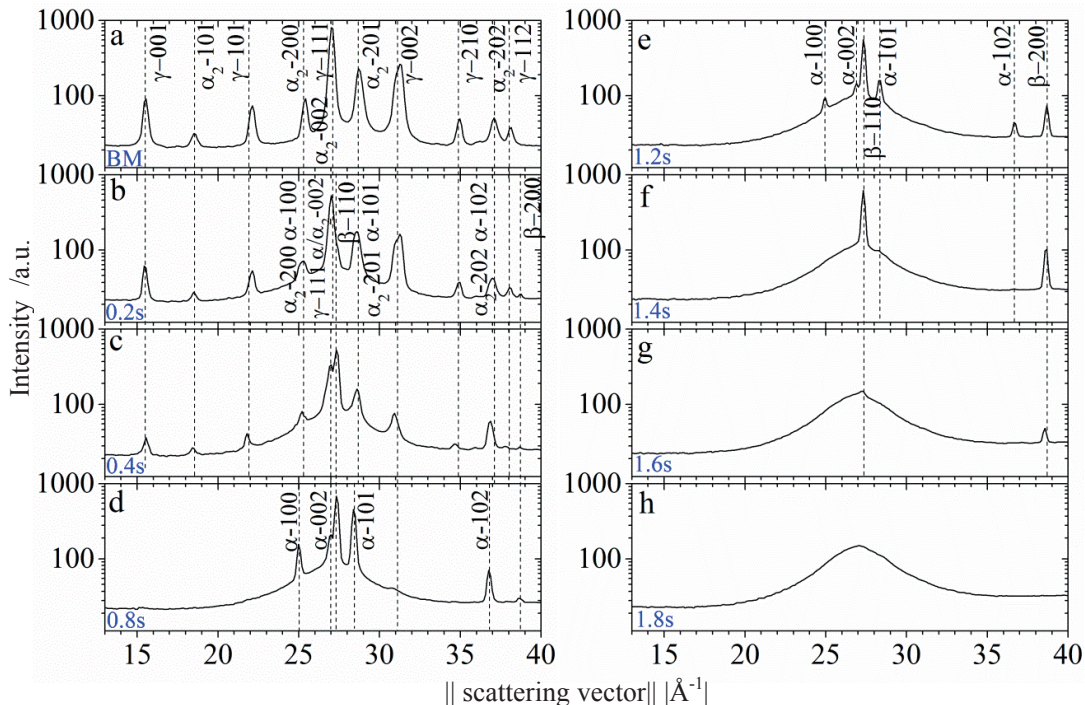

Figure 52: X-ray diffraction patterns observed during melting at a new position, revealing the phase compositions (a) of the base material and (b-h) at various times after the initiation of the laser melting process: (b) 0.2 s, (c) 0.4 s, (d) 0.8 s, (e) 1.2 s, (f) 1.4 s, (g) 1.6 s, and (h) 1.8 s. Laser power: 300 W.

7.3.3 **Solidification**

After the laser power was switched off, the melt solidified while the sample was maintained at 800 °C (Figure 53). From the series of diffraction patterns observed during the solidification stage (stage 4), it can be concluded that the phase-transformation sequence during solidification was $L \rightarrow L + \beta \rightarrow (L + \beta + \alpha) \rightarrow \beta + \alpha \rightarrow \alpha_2 + \beta \rightarrow \alpha_2 + \gamma + \beta$. The phase field indicated in parentheses $(L + \beta + \alpha)$ seems to indicate peritectic nucleation of α; however, this can be attributed to the overlapping of two phase fields $(L + \beta$ and $\beta + \alpha)$ when the X-rays passed through the material. A larger amount of the α_2 phase was retained compared with the thermodynamic equilibrium state. When the specimen was maintained at 900 °C from 14 s to 29 s, an increase in the heights of the γ-001 and γ-002 reflection peaks was observed, as shown in Figure 53 (i)-(j). At the same time, the heights of the α_2-101 and α_2-201 reflection peaks decreased, indicating an increase in the γ phase from 9.7 vol% to 28.4 vol% at the expense of the α_2 phase. It can be inferred that the constituent atoms
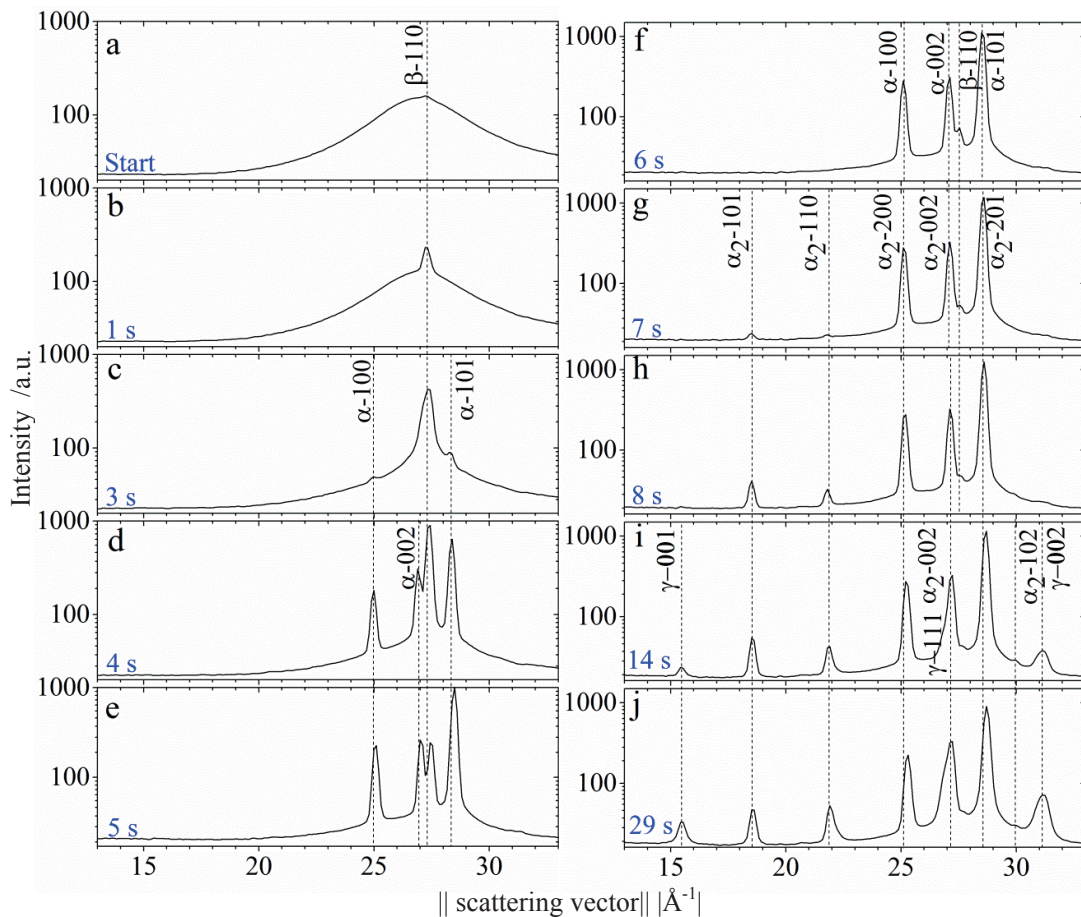

Figure 53: X-ray diffraction patterns observed during solidification, revealing the phase compositions (a) at the start of solidification and after (b) 1 s, (c) 3 s, (d) 4 s, (e) 5 s, (f) 6 s, (g) 7 s, (h) 8 s, (i) 14 s, and (j) 29 s. Heating temperature: 800 °C.

remained sufficiently mobile to undergo the phase transition $\alpha_2 \rightarrow \gamma$, consistent with [29, 106]. Because of the rapid cooling from the melt, the phases were out of chemical equilibrium. The α_2 inherited from α, which was enriched in Al, began to decompose into γ by expelling the Al and ultimately formed a lamellar structure. Meanwhile, the reflections of all phases shifted towards larger scattering vectors because of lattice shrinkage. These diffraction results agree well with the microstructural observation that the melt zone was predominantly composed of finely spaced $\alpha_2 + \gamma$ lamellar colonies.

7.3.4 Grain refinement

It is interesting to note that in both welds, either a laser power of 600 W for 0.9 s or a laser power of 300 W for 1.8 s, the total amount of incident energy was identical. However, when the material was heated at a higher laser power for a shorter time, a small amount of superheated solid γ remained in the melt, which was not present in the case of lower-power, longer-duration heating. The solidification process changed because of this small difference. Figure 54 (a-b) presents the diffraction patterns observed when the β phase began to precipitate in the melt, and (c-d) present the integrated Debye-Scherrer diffraction rings at the end of β solidification. The arrows in (c-d) indicate dots of α, proof of the end of β solidification and the beginning of $\beta \rightarrow \alpha$ transformation. When we compare the initial state during β solidification (Figure 54 (a)) and the final state (Figure 54 (c)), it is clear that in the faster-heating mode, small amounts of both β and γ phases could be simultaneously observed at the beginning of β precipitation. At the end of β precipitation, the solid β phase exhibited a continuous diffraction line, which indicated that the grains were small in size. It can be inferred that the β grains heterogeneously nucleated with the assistance of the superheated γ particles, leading to the formation of fine grains. The high heating rate played a role in producing superheated heterogeneous nucleation sites in the melt and refining the primary solidified β phase. However, in the slower-heating mode, only β was observed in the melt (Figure 54 (b)), and consequently, no continuous β diffraction is observed in Figure 54 (d). The few β dots in evidence indicate that a very limited number of individual β-grain reflections were recorded and that one β grain was significantly larger than the others. In this case, neither superheated particles nor refined grains were generated at the lower heating rate. Additionally, the refined β-grain size is consistent with the microstructural observations presented in Figure 55, where the β-grain boundaries are indicated by dotted outlines (The definition of β-grain boundary was introduced in chapter 7.2). The primary β grains had a diameter of 35 μm or 55 μm when welded at high or low laser powers, respectively, reflecting the refinement of the β grains induced by welding at a higher laser power. During cooling, the primary β grains transformed into lamellar colonies. Thus, at the higher heating rate, the size of the lamellar colonies was reduced. The γ phase formed at the β-grain boundaries because of the enrichment of Al.

Grains are refined with the assistance of the heterogeneous nucleation of α on borides during casting [48]. However, this mechanism does not apply in the case of a welding seam because the cooling rate is high and the refinement is suppressed [21, 27]. This investigation shed light on a newly conceived mechanism of grain refinement through the generation of superheated particles. The grains are refined by increasing the laser power, and the superheated γ serves as heterogeneous nucleation sites for β grains at a high heating rate.

7.4 Mechanical properties

7.4.1 Spot welding

The micro-hardness test was performed across the base material, heat affected zone and welding zone. The results are listed in Table 6. It demonstrates the welding zone made of high power shows higher hardness than that of low power welded specimen. The high hardness in the welding zone indicates that the refined colony size is stronger than the coarse one. The micro-hardness of the heat affected zone and base material are similar in both specimens.

Figure 56 presents the UTS and elongation-to-fracture values of the BM and welds tensile tested using different welding parameters at 25 °C, 650 °C and 750 °C. The welded
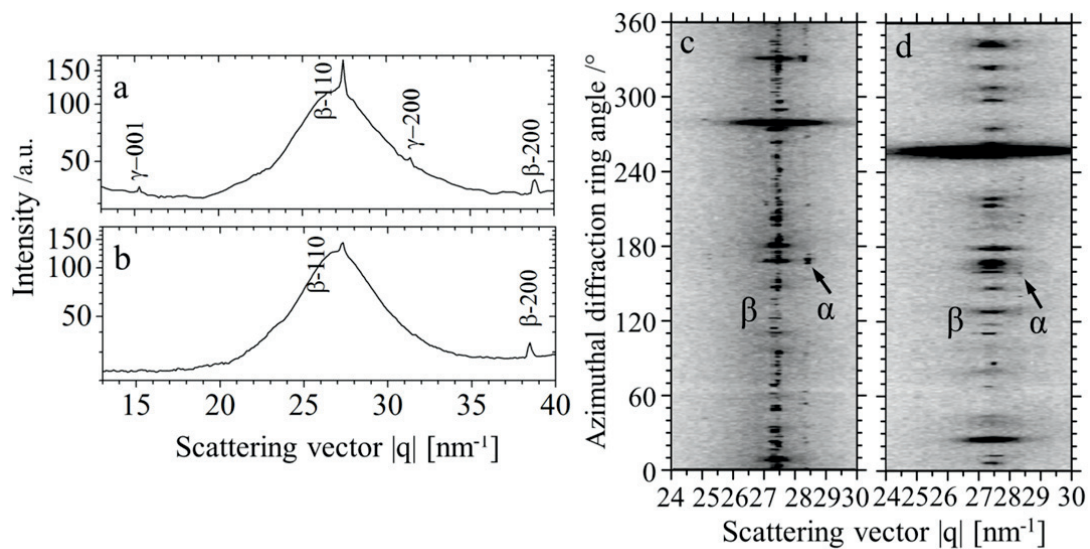

Figure 54: (a) and (b) X-ray diffraction patterns representing the beginning of β precipitation. (c) and (d) Debye-Scherrer diffraction rings, unrolled into lines and azimuthally integrated to show the X-ray diffraction patterns at the end of β solidification. The arrows indicate the precipitation of α. The diffraction patterns presented in (a) and (c) were captured for the following welding parameters: a laser power 600 W and a duration of 0.9 s. The diffraction patterns presented in (b) and (d) were captured for the following welding parameters: a laser power 300 W and a duration of 1.8 s.
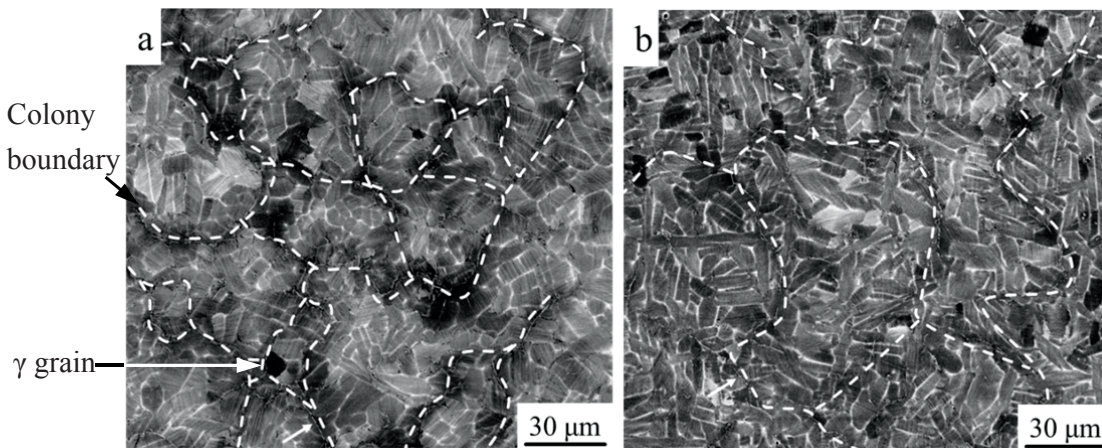
Figure 55: Microstructure of the melt zone after solidification. The dotted lines represent the boundaries of the primary β grains. The material was melted using a laser power of (a) 600 W and (b) 300 W. The arrow in (b) indicates borides.

specimens fractured in the WZ. The BM exhibited the highest UTS and elongation at all temperatures, and these experimental results are comparable with those of similar materials at both RT and high temperatures [65, 107-109]. The high ductility of the BM especially at high temperature is due to its duplex microstructure. The UTS of the weld seam formed at 600 W for 0.9 s is slightly better than that of the weld formed at 300 W for 1.8 s, and the elongation is improved by around a factor of two. The room temperature ductility of TiAl alloy could be improved by refined lamellar structures, which are less constrained [65, 110, 111]. The alloys with fine-grained, fully lamellar microstructure exhibit reasonable strength and high ductility. Moreover, the globular γ grains, which are located in the colony boundaries, are filled-up during plastic deformation with dislocations and deformation twins, which can compensate the lack of independent slip systems in the lamellae [109]. Thus, the refined lamellae colony size and the globular γ grains in the lamellar boundaries are favourable to increase ductility. The refined lamellar colony size are also reported to improve the tensile strength [111], similar to the grain size effect following the Hall-Patch relationship [112]. Besides, γ-grain boundaries serve as a barriers to dislocation motion caused by pile-up dislocations and act as an effective strengthening mechanism [113]. Thus, the refinement of the lamellar colonies combined with colony boundary γ-grains improves both the tensile strength and the ductility of the as-welded specimens. The results indicate that the refined colony size is beneficial for obtaining a high UTS and elongation to fracture.

Table 6: Vickers hardness of different zones of the laser-beam-welded plates (HV1). BM: base material, HAZ: heat-affected zone, WZ: welding zone.

	WZ	HAZ	BM
600 W, 0.9 s	434±28	375±9	384±10
300 W, 1.8 s	380±9	379±5	382±6

It is worth to mention that, when compared with the results in the last chapter, the tensile strength and ductility are largely improved in the as-welded specimens. The low UTS and elongation in specimen #1 in chapter 6 is due to large amount of α_2 phase with high residual stress. Fortunately, in this experiment, the brittle α_2 plates transform to lamellae colonies, which possess more slip systems through twinning in the γ lamellae. The residual stress could also be reduced attributed to higher pre-heating temperature and slower cooling gradient in the FLEXILAS, which is beneficial to delay crack initiation. The lamellar microstructure and low residual stress might be the reason of improved ductility in this experiment.
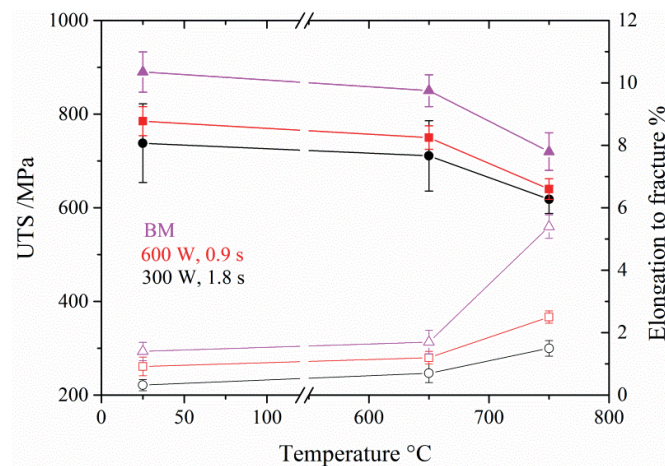

Figure 56: UTS (solid symbols) and elongation-to-fracture (hollow symbols) values for base material and spot welded specimens prepared using two sets of welding parameters at 25°C, 650°C and 750°C.

7.4.2 Bead-on-plate welding

When the knowledge of grain refinement during spot welding is transferred to bead-on-plate welding, the mechanical properties are shown in Figure 57. The weld seam formed at 1200 W and 10 mm/s exhibited mechanical properties inferior to those of the BM but superior to those of the welds formed at 600 W and 5 mm/s and at 300 W and 2.5 mm/s. The results indicate that the use of a high laser power is beneficial for obtaining a high UST and a high elongation to fracture. The strengthening and ductility mechanism is discussed in 7.4.1. It is important to note that, as the laser energy was further increased to 2400 W, the UTS decreased tremendously and the elongation approached 0. This behaviour was observed because such rapid welding generates defects in the weld seam, leading to the deterioration of the mechanical performance of the material. It indicates that only when the laser power and feed rate are within the optimal processing window may the refined grain size produced by a high laser power be beneficial to the mechanical properties of a sound final weld.
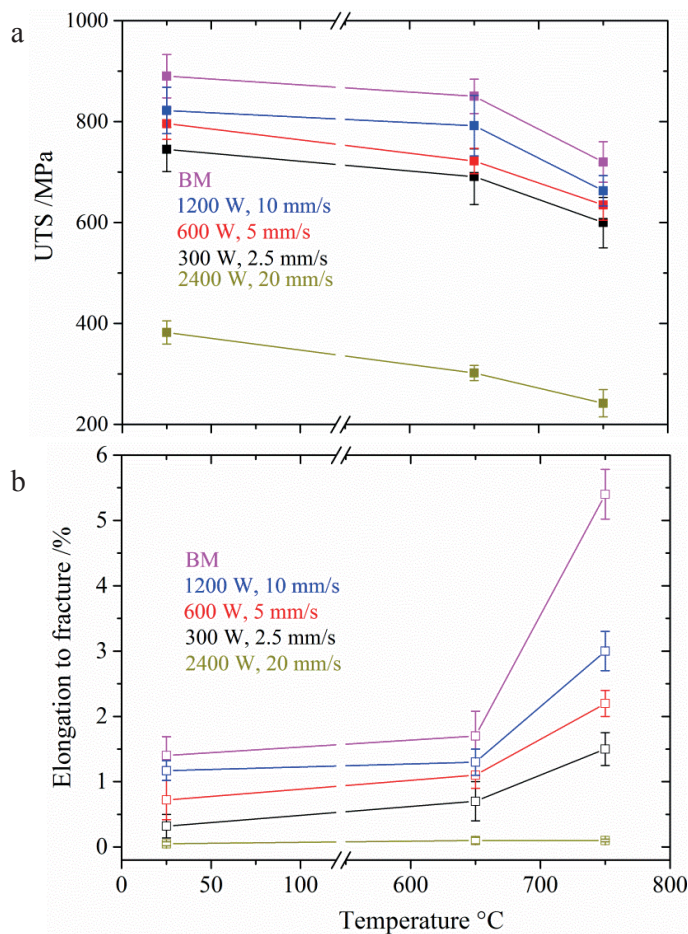
Figure 57: (a) UTS and (b) elongation-to-fracture values for bead-on-plate welded specimens prepared using four different sets of welding parameters at 25°C, 650°C and 750°C.

7.5 Conclusions

Through investigation of the results of the *in situ* experiments, the following conclusions can be drawn:

1. For a constant incident energy, a high heating rate is instrumental in producing grain refinement and improving the tensile properties of the final material. At a high heating rate, solid–solid transformations are strongly inhibited and the material disintegrates directly into the liquid phase, with the α_2 phase dissolving first through the following process: $\alpha_2 + \gamma \rightarrow \alpha_2 + \gamma + L \rightarrow \gamma + L$. The superheated γ produced at a high heating rate serves as heterogeneous nucleation sites and aids in refining the primary β grains.

2. Solid-solid phase transformations occur during the laser welding of bulk materials only when the heating rate is sufficiently low. Under such circumstances, thermal atomic diffusion occurs and leads to a solid–solid phase transformation that produces

α and β phases. In this case, no superheated particles are evident and grain refinement does not take place at such a low heating rate.

3. Because of heterogeneous nucleation on superheated γ, the primary β grains are refined, leading to the refinement of the lamellar colonies in the welding zone. The presence of lamellar colonies that are small in size combined with colony boundary γ-grains are beneficial to improve the UTS and ductility of the as-welded specimen at RT, 650°C and 750°C.

4. It is important to note that excessively rapid welding may induce defects in the WZ. Only when the laser power and feed rate are within the optimal processing window can high-laser-power welding and improve the mechanical properties of a sound final weld by the refined grain size.

Compared with resistance furnace heating, induction heating and dual-laser-beam heating, the process realized with the FLEXILAS welding facility controls the temperature precisely, heats the specimen homogeneously. The total consumption of time for welding one specimen is around 15 minutes, including the heating, welding and cooling. The time that laser welds the material is between 0.9 and 5 seconds, depending on the spot or bead-on-plate welding. It is reliable and has a high potential for industry application for producing sound TiAl welded specimens.

8 Conclusions

In this work, attention was paid on a number of scientific investigations. As stated in chapter 1, there were 3 objectives for laser beam welding of TiAl alloys as producing sound butt joints, optimising their microstructures and mechanical properties and, finally, understanding the phase transformations that occur during welding. Investigations were carried out with a sophisticated manner to achieve these objectives. The experiments started with the easy available γ-TAB alloy. After the first welding principle is proposed, the alloy 2 and TNB-V5 were also investigated. The 3 objectives were achieved one by one and these studies yielded the following conclusions:

1. It was experimentally demonstrated that despite the RT brittleness of TiAl alloys, these alloys can be welded in a crack-free manner with the proper application of heat treatments. The purpose of heat treatment is to heat the specimen above the brittle-to-ductile transition temperature prior to welding and to reduce the cooling rate during solidification. Pre-heating the specimen above 750°C using a furnace or a defocused laser was found to be of critical importance to the production of a sound weld. Heating the specimen to 800°C immediately after welding was also found to be effective in producing a crack-free weld.

2. These investigations were followed by an effort to optimise the microstructural and mechanical properties that can be achieved through the application of post weld heat treatment. (1) Post weld heat treatment is useful in refining textured α_2 colonies. Because of the high cooling rate during welding, the effect of the grain refinement induced by boride was suppressed, and a large number of textured α_2 colonies were observed in the welding zone. These colonies were broken down after post-weld annealing into refined grains as a result of the heterogeneous nucleation of α grains on borides. (2) Post weld heat treatment modifies the microstructure of the material and improves its tensile properties. By transforming the massive γ in the TNB-V5 alloy into a convoluted microstructure, the elongation to fracture could be increased by 77% at the expense of a 4% reduction in strength. In addition, the near-γ grains in the base material were modified into lamellae in the TAB alloy, and the material gained balanced mechanical properties. It is important to note that the optimal heating temperature and duration depend on the alloy composition and the desired microstructure. (3) Post weld heat treatment can relieve residual stresses. A large amount of residual stress is generated because of the shrinkage of the welding zone and the limited slip systems that form in the presence of a large amount of the α_2 phase. With the assistance of thermal atomic activation, these residual stresses can be considerably relieved.

3. To gain an understanding of the relationship between the welding parameters and grain refinement, *in situ* observations of laser beam welding via HEXRD were conducted. This was the first *in situ* laser-beam-welding experiment involving bulk materials for the observation of phase transformations as a function of the heating rate. This study concluded the following: (1) Phase transformations occur only when the laser energy is sufficiently low. At a high heating rate, solid–solid transformations are strongly inhibited and the material disintegrates directly into the liquid phase. (2) The superheated particles produced at a high heating rate refine the lamellar colonies. This is a newly discovered mechanism of grain refinement through the assistance of superheated particles, which is not suppressed by a high cooling rate. (3) The refined lamellar microstructure improves both UTS and elongation of the welding zone.

In addition, the productivity was increased through the improved welding methods. The heating methods varied from resistance heated furnace, induction furnace, dual-laser-beam welding to FELXILAS facility, aiming to reduce the welding time and generate a reliable and effective welding procedure. The disadvantages as long heating cycle of a resistance heated furnace, the difficult clamping design of an induction furnace and the laser parameter variation by specimen geometry during dual-laser heating were overcome by the FELXILAS facility. It heated the specimens fast and homogeneously and precisely controlled by an electrical device. The FELXILAS heating method is potential to be applied into industry application.

The presented studies demonstrate the potential of the laser beam welding of γ-TiAl alloys on the laboratory scale. With the new approach, it opens up a branch of opportunities for researches in future work. First, in addition to the newly gained understanding of the phase transformations during welding, it would be interesting to know how the residual stress develops during welding and which influencing factors are responsible for the high observed stresses. Using the FLEXILAS experimental set-up and synchrotron beam, the stress distribution as a function of time and position can be plotted.

Second, the reason why the grain refinement induced by borides can only proceed at low cooling rates is not clear. It may be because of the low cooling rate, the borides are transformed into an orientation that favours α precipitation. With the aid of EBSD and synchrotron radiation, investigations could be conducted to further extend the understanding of γ-TiAl alloys.

Third, it has been demonstrated that post weld heat treatment is necessary for the microstructural and mechanical optimisation of the final welds; however, it is quite time consuming when the specimen is heated only in a furnace. One possible solution is to apply the heat treatment using a combination of a defocused laser beam and a furnace with precise

control of the temperature field. Heat treatment can be much more efficient when the region of interest can be selectively heated while maintaining a homogeneous temperature throughout the rest of the specimen.

Bibliography

[1] Dimiduk DM. Gamma titanium aluminide alloys—an assessment within the competition of aerospace structural materials. Materials Science and Engineering: A 1999;263:281-8.

[2] Appel F, Paul J, Wagner R. Alloy based on titanium aluminides. EP1015650 B1 1998.

[3] Clemens H, Mayer S. Design, Processing, Microstructure, Properties, and Applications of Advanced Intermetallic TiAl Alloys. Adv Eng Mater 2013;15:191-215.

[4] Tetsui T. Application of TiAl in a Turbocharger for Passenger Vehicles. Adv Eng Mater 2001;3:307-10.

[5] Tetsui T. Development of a TiAl turbocharger for passenger vehicles. Materials Science and Engineering: A 2002;329–331:582-8.

[6] Clemens H, Smarsly W, in: M. Heilmaier (Ed.) Euro Superalloys 2010, Trans Tech Publications Ltd, Stafa, Zurich, 2011, pp. 551-6.

[7] Kelly T. Presentation at the Symposium on "Structural Aluminides for Elevated Temperature Applications", TMS 2008 Annual Meeting. New Orleans, LA, USA. 2008.

[8] Bewlay BP, Weimer M, Kelly T, Suzuki A, Subramanian PR. The Science, Technology, and Implementation of TiAl Alloys in Commercial Aircraft Engines. MRS Proceedings 2013;1516:49-58.

[9] Liu J, Ventzke V, Staron P, Schell N, Kashaev N, Huber N. Investigation of In Situ and Conventional Post-Weld Heat Treatments on Dual-Laser-Beam-Welded gamma-TiAl-Based Alloy. Adv Eng Mater 2012;14:923-7.

[10] Liu ZC, Lin JP, Li SJ, Chen GL. Effects of Nb and Al on the microstructures and mechanical properties of high Nb containing TiAl base alloys. Intermetallics 2002;10:653-9.

[11] Chaturvedi MC, Xu Q, Richards NL. Development of crack-free welds in a TiAl-based alloy. J Mater Process Tech 2001;118:74-8.

[12] Chen GQ, Zhang BG, Liu W, Feng JC. Crack formation and control upon the electron beam welding of TiAl-based alloys. Intermetallics 2011;19:1857-63.

[13] Glatz W, Clemens H. Diffusion bonding of intermetallic Ti-47Al-2Cr-0.2Si sheet material and mechanical properties of joints at room temperature and elevated temperatures. Intermetallics 1997;5:415-23.

[14] Ventzke V, Bohm KH, Kocak M, Riekehr S, Horstmann M, Merhof P, Watzlaw M. Microstructure and mechanical properties of friction welded gamma-TiAl based alloy Ti-47Al-3.5(Mn+Cr+Nb)-0.8(B+Si) in investment cast condition. Materialwissenschaft und Werkstofftechnik 2006;37:649-60.

[15] Miyashita T, Hino H. Friction Welding Characteristics of TiAl Intermetallic Compound. J Jpn I Met 1994;58:215-20.

[16] Ventzke V, Riekehr S, Horstmann M, Kashaev N, Brokmeier HG, Huber N. The Development of the Rotational Friction Welding Process for the Welding of γ-TiAl-Casting Alloy Ti-47Al-3.5(Mn+Cr+Nb)-0.8(B+Si) to Ti6Al4V. Practical Metallography 2014;51:321-52.

[17] Radaj D. Heat Effects of Welding: Temperature Field, Residual Stress, Distortion. Berlin Heidelberg New York: Springer; 1992.

[18] Masubuchi K. Analysis of Welded Structures: Residual Stress, Distortion and their Consequences. UK: Pergamon; 1980.

[19] Liu J, Ventzke V, Staron P, Brokmeier H-G, Oehring M, Kashaev N, Huber N. Effect Of Dual-Laser Beam Welding On Microstructure Properties Of Thin-Walled γ-Tial Based Alloy Ti-45Ai-5Nb-0.2C-0.2B (TNB). In: Supplemental Proceedings: Vol. 1: Materials Processing and Interfaces. Warrendale TMS 2012:887-94.

[20] Arenas MF, Acoff VL. The effect of postweld heat treatment on gas tungsten are welded gamma titanium aluminide. Scripta Mater 2002;46:241-6.

[21] Liu J, Dahmen M, Ventzke V, Kashaev N, Poprawe R. The effect of heat treatment on crack control and grain refinement in laser beam welded beta-solidifying TiAl-based alloy. Intermetallics 2013;40:65-70.

[22] Clemens H, Kestler H. Processing and applications of intermetallic gamma-TiAl-based alloys. Adv Eng Mater 2000;2:551-70.

[23] Schwaighofer E, Clemens H, Mayer S, Lindemann J, Klose J, Smarsly W, Guther V. Microstructural design and mechanical properties of a cast and heat-treated intermetallic multi-phase gamma-TiAl based alloy. Intermetallics 2014;44:128-40.

[24] Clemens H, Bartels A, Bystrzanowski S, Chladil H, Leitner H, Dehm G, Gerling R, Schimansky FP. Grain refinement in gamma-TiAl-based alloys by solid state phase transformations. Intermetallics 2006;14:1380-5.

[25] Hu D, Yang C, Huang A, Dixon M, Hecht U. Grain refinement in beta-solidifying Ti44Al8Nb1B. Intermetallics 2012;23:49-56.

[26] Jin YG, Wang JN, Yang J, Wang Y. Microstructure refinement of cast TiAl alloys by beta solidification. Scripta Mater 2004;51:113-7.

[27] Oehring M, Stark A, Paul JDH, Lippmann T, Pyczak F. Microstructural refinement of boron-containing beta-solidifying gamma-titanium aluminide alloys through heat treatments in the beta phase field. Intermetallics 2013;32:12-20.

[28] Wu XH, Hu D. Microstructural refinement in cast TiAl alloys by solid state transformations. Scripta Mater 2005;52:731-4.

[29] Liu J, Ventzke V, Staron P, Schell N, Kashaev N, Huber N. Effect of Post-weld Heat Treatment on Microstructure and Mechanical Properties of Laser Beam Welded TiAl-based Alloy. Metall Mater Trans A 2014;45:16-28.

[30] Staron P, Kocak M, Williams S. Residual stresses in friction stir welded Al sheets. Applied Physics A 2002;74:S1161-S2.

[31] Staron P, Kocak M, Williams S, Wescott A. Residual stress in friction stir-welded Al sheets. Physica B 2004;350:E491-E3.

[32] Jones SA, Kaufman MJ. Phase equilibria and transformations in intermediate titanium-aluminum alloys. Acta Metall Mater 1993;41:387-98.

[33] Clemens H, Chladil HF, Wallgram W, Zickler GA, Gerling R, Liss KD, Kremmer S, Guther V, Smarslyg W. In and ex situ investigations of the beta-phase in a Nb and Mo containing gamma-TiAl based alloy. Intermetallics 2008;16:827-33.

[34] Witusiewicz VT, Bondar AA, Hecht U, Rex S, Velikanova TY. The Al-B-Nb-Ti system III. Thermodynamic re-evaluation of the constituent binary system Al-Ti. J Alloy Compd 2008;465:64-77.

[35] Schuster J, Palm M. Reassessment of the binary Aluminum-Titanium phase diagram. JPED 2006;27:255-77.

[36] Küstner V, Oehring M, Chatterjee A, Clemens H, Appel F. Solidification and Crystallization. Weinheim: Wiley-VCH Verlag GmbH; 2004.

[37] Johnson DR, Inui H, Yamaguchi M. Crystal growth of TiAl alloys. Intermetallics 1998;6:647-52.

[38] Naka S, Thomas M, Sanchez C, Khan T. Development of third generation castable gamma titanium aluminides: role of solidification paths. Structural Intermetallics, Warrendale TMS 1997.

[39] Küstner V, Oehring M, Chatterjee A, Güther V, Brokmeier H-G, Clemens H, Appel F. Gamma Titanium Aluminides 2003 (eds Y. - W. Kim , H. Clemens , and A.H. Rosenberger) Warrendale, TMS 2003:89.

[40] Dey SR, Hazotte A, Bouzy E. Crystallography and phase transformation mechanisms in TiAl-based alloys - A synthesis. Intermetallics 2009;17:1052-64.

[41] Dey SR, Bouzy E, Hazotte A. Features of feathery gamma structure in a near-gamma TiAl alloy. Acta Mater 2008;56:2051-62.

[42] Dey SR, Bouzy E, Hazotte A. EBSD characterisation of massive gamma nucleation and growth in a TiAl-based alloy. Intermetallics 2006;14:444-9.

[43] Dey SR, Hazotte A, Bouzy E, Naka S. Development of Widmanstatten laths in a near-gamma TiAl alloy. Acta Mater 2005;53:3783-94.

[44] Schnitzer R, Chladil HF, Scheu C, Clemens H, Bystrzanowski S, Bartels A, Kremmer S. Herstellung lamellarer Gefügetypen in intermetallischen TiAl- Legierungen und deren Charakterisierung. Practical Metallography 2007;44:430-42.

[45] Wu XH. Review of alloy and process development of TiAl alloys. Intermetallics 2006;14:1114-22.

[46] De Graef M, Löfvander JPA, McCullough C, Levi CG. The evolution of metastable B_f borides in a Ti-Al-B alloy. Acta Metall Mater 1992;40:3395-406.

[47] Imayev RM, Imayev VM, Oehring M, Appel F. Alloy design concepts for refined gamma titanium aluminide based alloys. Intermetallics 2007;15:451-60.

[48] Hecht U, Witusiewicz V, Drevermann A, Zollinger J. Grain refinement by low boron additions in niobium-rich TiAl-based alloys. Intermetallics 2008;16:969-78.

[49] Cheng TT. The mechanism of grain refinement in TiAl alloys by boron addition — an alternative hypothesis. Intermetallics 2000;8:29-37.

[50] Christodoulou L. International workshop on gamma alloys. The University of Birmingham; 1996.

[51] Hu D, Yang C, Huang A, Dixon M, Hecht U. Solidification and grain refinement in Ti45Al2Mn2Nb1B. Intermetallics 2012;22:68-76.

[52] Hill D, Banerjee R, Huber D, Tiley J, Fraser HL. Formation of equiaxed alpha in TiB reinforced Ti alloy composites. Scripta Mater 2005;52:387-92.

[53] Genc A, Banerjee R, Hill D, Fraser HL. Structure of TiB precipitates in laser deposited in situ, Ti-6Al-4V-TiB composites. Mater Lett 2006;60:859-63.

[54] Banerjee R, Genc A, Hill D, Collins PC, Fraser HL. Nanoscale TiB precipitates in laser deposited Ti-matrix composites. Scripta Mater 2005;53:1433-7.

[55] Staron P, Fischer T, Lippmann T, Stark A, Daneshpour S, Schnubel D, Uhlmann E, Gerstenberger R, Camin B, Reimers W, Eidenberger E, Clemens H, Huber N, Schreyer A. In Situ Experiments with Synchrotron High-Energy X-Rays and Neutrons. Adv Eng Mater 2011;13:658-63.

[56] Shuleshova O, Holland-Moritz D, Loser W, Voss A, Hartmann H, Hecht U, Witusiewicz VT, Herlach DM, Buchner B. In situ observations of solidification processes in gamma-TiAl alloys by synchrotron radiation. Acta Mater 2010;58:2408-18.

[57] Babu SS, Elmer JW, Vitek JM, David SA. Time-resolved X-ray diffraction investigation of primary weld solidification in Fe-C-Al-Mn steel welds. Acta Mater 2002;50:4763-81.

[58] Xu Q, Chaturvedi MC, Richards NL. The role of phase transformation in electron-beam welding of TiAl-based alloys. Metall Mater Trans A 1999;30:1717-26.

[59] Arenas MF, Acoff VL. Analysis of gamma titanium aluminide welds produced by gas tungsten arc welding. Weld J 2003;82:110s-5s.

[60] Arenas MF, Acoff VL. An investigation of the cracking susceptibility of gamma titanium aluminide welds produced by gas tungsten arc welding. High Temp Mat Pr-Isr 2004;23:25-34.

[61] Reisgen U, Olschok S, Backhaus A. Electron beam welding of titanium aluminides - Influence of the welding parameters on the weld seam and microstructure. Materialwiss Werkst 2010;41:897-907.

[62] Kestler H, Clemens H. Titanium and Titanium Alloys (Eds: Leyens, C. and Peters, M.). Weinheim: WILEY-VCH; 2003.

[63] Kim Y-W. Ordered intermetallic alloys, part III: Gamma titanium aluminides. JOM 1994;46:30-9.

[64] Liu CT, Maziasz PJ, Clemens DR, Schneibel JH, Sikka VK, Nieh TG, Wright JL, Walke LR. Gamma Titanium Aluminides, Y.-W. Kim, R. Wagner, and M. Yamaguchi, eds., Warrendale TMS 1995:679.

[65] Liu CT, Schneibel JH, Maziasz PJ, Wright JL, Easton DS. Tensile properties and fracture toughness of TiAl alloys with controlled microstructures. Intermetallics 1996;4:429-40.

[66] Nieh TG, Wadsworth J. Fine structure superplastic intermetallics. Int Mater Rev 1999;44:59-75.

[67] Nieh TG, Hsiung LM, Wadsworth J. Superplastic behavior of a powder metallurgy TiAl alloy with a metastable microstructure. Intermetallics 1999;7:163-70.

[68] Goods SH, Nieh TG. Mechanisms of Intergranular Cavity Nucleation and Growth during Creep. Scripta Metall Mater 1983;17:23-30.

[69] Zhang CP, Zhang KF. Superplasticity of a gamma-TiAl alloy and its microstructure and cavity evolution in deformation. J Alloy Compd 2010;492:236-40.

[70] Shiota H, Tokaji K, Ohta Y. Influence of lamellar orientation on fatigue crack propagation behavior in titanium aluminide TiAl. Materials Science and Engineering: A 1998;243:169-75.

[71] Heatherly L, George EP, Liu CT, Yamaguchi M. An Auger investigation of the fracture behavior of PST TiAl alloys. Intermetallics 1997;5:281-8.

[72] Kim SW, Kumar KS, Oh MH, Wee DM. Crack propagation behavior in TiAl-Nb single and Bi-PST crystals. Intermetallics 2007;15:976-84.

[73] Yokoshima S, Yamaguchi M. Fracture behavior and toughness of PST crystals of TiAl. Acta Mater 1996;44:873-83.

[74] Chan KS, Onstott J, Kumar KS. The fracture resistance of a binary TiAl alloy. Metall Mater Trans A 2000;31:71-80.

[75] Chen YY, Niu HZ, Kong FT, Xiao SL. Microstructure and fracture toughness of a beta phase containing TiAl alloy. Intermetallics 2011;19:1405-10.

[76] Hu D. Effect of boron addition on tensile ductility in lamellar TiAl alloys. Intermetallics 2002;10:851-8.

[77] Hu D, Jiang H, Wu X. Microstructure and tensile properties of cast Ti-44Al-4Nb-4Hf-0.1Si-0.1B alloy with refined lamellar microstructures. Intermetallics 2009;17:744-8.

[78] Hauk V. Structural and Residual Stress Analysis by Nondestructive Methods. Amsterdam: Elsevier; 1997.

[79] Kostov V, Gibmeier J, Wilde F, Staron P, Rossler R, Wanner A. Fast in situ phase and stress analysis during laser surface treatment: A synchrotron x-ray diffraction approach. Rev Sci Instrum 2012;83.

[80] Schnubel D, Horstmann M, Ventzke V, Riekehr S, Staron P, Fischer T, Huber N. Retardation of fatigue crack growth in aircraft aluminium alloys via laser heating - Experimental proof of concept. Materials Science and Engineering: A 2012;546:8-14.

[81] Schnubel D, Huber N. Retardation of fatigue crack growth in aircraft aluminium alloys via laser heating - Numerical prediction of fatigue crack growth. Comp Mater Sci 2012;65:461-9.

[82] Paradowska A, Finlayson TR, Price JWH, Ibrahim R, Steuwer A, Ripley M. Investigation of reference samples for residual strain measurements in a welded specimen by neutron and synchrotron X-ray diffraction. Physica B 2006;385–386, Part 2:904-7.

[83] Liss K-D, Bartels A, Schreyer A, Clemens H. High-energy X-rays: a tool for advanced bulk investigations in materials science and physics. Textures and Microstructures 2003;35:219-52.

[84] Hu D, Mei JF, Wickins M, Harding RA. Microstructure and tensile properties of investment cast Ti-46Al-8Nb-1B alloy. Scripta Mater 2002;47:273-8.

[85] Simpkins Ii RJ, Rourke MP, Bieler TR, McQuay PA. The effects of HIP pore closure and age hardening on primary creep and tensile property variations in a TiAl XD™ alloy with 0.1 wt.% carbon. Materials Science and Engineering: A 2007;463:208-15.

[86] Liss KD, Stark A, Bartels A, Clemens H, Buslaps T, Phelan D, Yeoh LA. Directional atomic rearrangements during transformations between the alpha- and gamma-phases in titanium aluminides. Adv Eng Mater 2008;10:389-92.

[87] Karadge M, Kim YW, Gouma PI. Precipitation strengthening in K5-series gamma-TiAl alloyed with silicon and carbon. Metall Mater Trans A 2003;34A:2129-38.

[88] Gouma PI, Subramanian K, Kim YW, Mills MJ. Annealing studies of gamma-titanium aluminides alloyed with light elements for creep strengthening. Intermetallics 1998;6:689-93.

[89] Niu HZ, Kong FT, Chen YY, Zhang CJ. Low-temperature superplasticity of forged Ti-43Al-4Nb-2Mo-0.5B alloy. J Alloy Compd 2012;543:19-25.

[90] Liss KD, Bartels A, Clemens H, Bystrzanowski S, Stark A, Buslaps T, Schimansky FP, Gerling R, Scheu C, Schreyer A. Recrystallization and phase transitions in a gamma-TiAl-based alloy as observed by ex situ and in situ high-energy X-ray diffraction. Acta Mater 2006;54:3721-35.

[91] Cheng TT, Loretto MH. The decomposition of the beta phase in Ti–44Al–8Nb and Ti–44Al–4Nb–4Zr–0.2Si alloys. Acta Mater 1998;46:4801-19.

[92] Gey N, Humbert M. Characterization of the variant selection occurring during the alpha - beta - alpha phase transformations of a cold rolled titanium sheet. Acta Mater 2002;50:277-87.

[93] Chladil HF, Clemens H, Leitner H, Bartels A, Gerling R, Schimansky FP, Kremmer S. Phase transformations in high niobium and carbon containing gamma-TiAl based alloys. Intermetallics 2006;14:1194-8.

[94] Hu D, Botten RR. Phase transformations in some TiAl-based alloys. Intermetallics 2002;10:701-15.

[95] Appel F, Paul JDH, Oehring M. Gamma Titanium Aluminide Alloys Science and Technology. Weinheim: WILEY-VCH; 2011.

[96] Gerling R, Schimansky FP, Stark A, Bartels A, Kestler H, Cha L, Scheu C, Clemens H. Microstructure and mechanical properties of Ti45Al5Nb+(0-0.5C) sheets. Intermetallics 2008;16:689-97.

[97] Christoph U, Appel F, Wagner R. Dislocation dynamics in carbon-doped titanium aluminide alloys. Materials Science and Engineering: A 1997;239–240:39-45.

[98] Saage H, Huang AJ, Hu D, Loretto MH, Wu X. Microstructures and tensile properties of massively transformed and aged Ti46Al8Nb and Ti46Al8Ta alloys. Intermetallics 2009;17:32-8.

[99] Liu J, Staron P, Riekehr S, Stark A, Schell N, Huber N, Schreyer A, Müller M, Kashaev N. In situ study of phase transformations during laser-beam welding of a TiAl alloy for grain refinement and mechanical property optimization. Intermetallics 2015;62:27-35.

[100] Yang C, Jiang H, Hu D, Huang A, Dixon M. Effect of boron concentration on phase transformation texture in as-solidified Ti44Al8NbxB. Scripta Mater 2012;67:85-8.

[101] Mei QS, Lu K. Melting and superheating of crystalline solids: From bulk to nanocrystals. Progress in Materials Science 2007;52:1175-262.

[102] Alsayed AM, Islam MF, Zhang J, Collings PJ, Yodh AG. Premelting at defects within bulk colloidal crystals. Science 2005;309:1207-10.

[103] Dahmen U, Hagege S, Faudot F, Radetic T, Johnson E. Observations of interface premelting at grain-boundary precipitates of Pb in Al. Philos Mag 2004;84:2651-62.

[104] Fecht HJ, Johnson WL. Entropy and enthalpy catastrophe as a stability limit for crystalline material. Nature 1988;334:50-1.

[105] Lele S, Rao PR, Dubey KS. Entropy catastrophe and superheating of crystals. Nature 1988;336:567-8.

[106] Yeoh LA, Liss KD, Bartels A, Chladil H, Avdeev M, Clemens H, Gerling R, Buslaps T. In situ high-energy X-ray diffraction study and quantitative phase analysis in the alpha plus gamma phase field of titanium aluminides. Scripta Mater 2007;57:1145-8.

[107] Appel F, Oehring M, Wagner R. Novel design concepts for gamma-base titanium aluminide alloys. Intermetallics 2000;8:1283-312.

[108] Draper SL, Isheim D. Environmental embrittlement of a third generation gamma TiAl alloy. Intermetallics 2012;22:77-83.

[109] Voisin T, Monchoux J-P, Hantcherli M, Mayer S, Clemens H, Couret A. Microstructures and mechanical properties of a multi-phase β-solidifying TiAl alloy densified by spark plasma sintering. Acta Mater 2014;73:107-15.

[110] Hoppe R, Appel F. Deformation-induced internal stresses in multiphase titanium aluminide alloys. Acta Mater 2014;64:169-78.

[111] Kim Y-W. Microstructural evolution and mechanical properties of a forged gamma titanium aluminide alloy. Acta Metall Mater 1992;40:1121-34.

[112] Umakoshi Y, Nakano T. The role of ordered domains and slip mode of α_2 phase in the plastic behaviour of TiAl crystals containing oriented lamellae. Acta Metall Mater 1993;41:1155-61.

[113] Nakano T, Yokoyama A, Umakoshi Y. Effect of Nb addition on the plastic behavior of TiAl crystals containing oriented lamellae. Scr Metal. Mater 1992;27:1253-8.

List of publications

[1]. Liu J, Ventzke V, Staron P, Schell N, Kashaev N, Huber N. Investigation of In Situ and Conventional Post-Weld Heat Treatments on Dual-Laser-Beam-Welded gamma-TiAl-Based Alloy. Adv Eng Mater 2012;14:923-7.

[2]. Liu J, Ventzke V, Staron P, Brokmeier H-G, Oehring M, Kashaev N, Huber N. Effect Of Dual-Laser Beam Welding On Microstructure Properties Of Thin-Walled γ-Tial Based Alloy Ti-45Ai-5Nb-0.2C-0.2B (TNB). In: Supplemental Proceedings: Vol. 1: Materials Processing and Interfaces. Warrendale TMS 2012:887-94.

[3]. Liu J, Dahmen M, Ventzke V, Kashaev N, Poprawe R. The effect of heat treatment on crack control and grain refinement in laser beam welded beta-solidifying TiAl-based alloy. Intermetallics 2013;40:65-70.

[4]. Liu J, Ventzke V, Staron P, Schell N, Kashaev N, Huber N. Effect of Post-weld Heat Treatment on Microstructure and Mechanical Properties of Laser Beam Welded TiAl-based Alloy. Metall Mater Trans A 2014;45:16-28.

[5]. Liu J, Staron P, Schnubel D, Schell N, Huber N, Kashaev N, in: 29th Congress of the International Council of the Aeronautical Sciences, ICAS 2014, International Council of the Aeronautical Sciences, 2014.

[6]. Liu J, Staron P, Riekehr S, Stark A, Schell N, Huber N, Schreyer A, Müller M, Kashaev N. In situ study of phase transformations during laser-beam welding of a TiAl alloy for grain refinement and mechanical property optimization. Intermetallics 2015;62:27-35.

Acknowledgements

Geesthacht 18.6.2015   Jie Liu